

R&D studies of Muon Polarimeter
for J-PARC E06
T-Violation Experiment

Master's Thesis

35-096116

Keisuke Yoshihara

Department of Physics,
Graduate School of Science, The University of Tokyo

20th January 2011

Abstract

The J-PARC E06 experiment, called TREK, aims to measure the transverse muon polarization in $K^+ \rightarrow \pi^0 \mu^+ \nu_\mu$ decay as an indicator of the direct T-violation in weak interaction. From the KEK PS E246 experiment, the result of $P_T = -0.0017 \pm 0.0023(stat) \pm 0.0011(syst)$ was obtained, which is consistent with T-invariance. Now the TREK Collaboration intends to continue the P_T experiment at J-PARC, where a higher accelerator beam intensity will be available and a higher experimental sensitivity can be expected, in order to search for new physics beyond SM. We aim for a sensitivity of $\delta P_T \sim 10^{-4}$, which might reveal some new physics beyond the SM in this sensitive region. In order to achieve this sensitivity, we have to improve some detectors to decrease the systematic errors. The largest systematic error is the effect of multiple scattering of muons through the Cu degrader in front of the polarimeter. The TREK experiment, however, will be free from this error as we will employ an active polarimeter. In order to evaluate the performance of the active polarimeter, we have performed beam test at TRIUMF in Vancouver, Canada. In this thesis, the results of this beam test and other studies including an alternative design of polarimeter are presented. Finally the result of the commissioning of K1.1BR beamline at Hadron Experimental Hall in J-PARC is presented.

Acknowledgements

First of all, I would like to express my sincere gratitude to my supervisor, Prof. T. Kawamoto, who allowed me to join the TREK experiment and encouraged my research and my private life. Numerous discussions with him greatly attracted me to particle physics. I want to express my thanks Prof. S. Asai, who allowed me to join this experiment. I am deeply indebted to Dr. T. Namba for his valuable suggestions and support. I also owe him for carefully reading this thesis repeatedly. I greatly want to express my gratitude to Prof. J. Imazato, who attracted me to this exciting experiment and gave me so many chances to learn a lot about physics and detectors. He also gave me a lot of helpful advice, also showing me the attitude necessary for a scientist through his daily work. I am much indebted to Prof. M. Hasinoff for carefully reading this work repeatedly in spite of my poor English, and also for helping me to do the beam test at TRIUMF. I am grateful to Dr. Y. Igarashi, who always worked with me in KEK and in J-PARC and taught me about not only the Data Acquisition system, but also other hardware and software technique. I owe him for his kindness and his support with regard to my research and the enjoyable working atmosphere. I would like to express my gratitude to Dr. H. Yamazaki for his advice. A lot of discussion with him greatly promoted my understanding for particle physics. I would like to express my gratitude to Dr. S. Shimizu for his advice. I could see his passion for physics experiments and he also gave me many suggestion for my studies. I would like to express my gratitude to Dr. A. Toyoda for his support. Without his support, the beam tuning in J-PARC could not have been performed. I would like to express my gratitude to Dr. K. Horie for her support with regard to my simulation work. I would like to express my gratitude to Dr. M. Uchida for his support with regard to my simulation work. I would like to express my gratitude to Dr. F. Habermehl for his help for the preparation of K1.1BR commissioning. I owe him for his kindness. I would also like to thank the other members of the TREK collaboration. I want to express my gratitude to all the secretaries of our group, R. Anbiru, M. Shiota, N. Kataoka, C. Morita, M. Suzuki. I would like to thank all the students of our group, R. Inoue, S. Kazama, K.K. Siang, Y. Sasaki, A. Miyazaki, Y. Fuji, T. Kamiya, Y. Ninomiya, K. Bendtz, Y. Yamaguchi, Y. Iiyama, elderly students, and younger students. Finally, I would like to express my gratitude to my parents, my girlfriend, and all relatives for their continuous support and encouragement.

Contents

Introduction	1
1 J-PARC TREK Experiment	5
1.1 Phenomenology of $K_{\mu 3}$ Decay	5
1.2 Transverse Polarization P_T	7
1.3 Theoretical Predictions	9
1.3.1 Standard Model	9
1.3.2 Final state interactions	9
1.3.3 Multi-Higgs doublet model	10
1.3.4 SUSY models	12
1.4 J-PARC TREK experiment	15
1.5 Experimental Setup	16
1.5.1 Overview of TREK detector setup	16
1.5.2 Fitch-type Cherenkov counter	16
1.5.3 Beamline	17
1.5.4 K^+ stopping target	18
1.5.5 Photon Counter	19
1.5.6 Superconducting spectrometer magnet	22
1.5.7 Tracking Chamber	22
1.5.8 Muon polarimeter	25
1.5.9 Muon polarimeter magnet	25
1.5.10 Electronics and data acquisition	27
2 Muon Polarimeter for TREK Experiment	28
2.1 Muon polarimeter	28
2.2 Passive polarimeter for the E246	29
2.3 Requirements for an active polarimeter	34
2.4 Concepts of the polarimeter design	34
2.5 Requirement for stopper material	35
2.6 Expected performance of the polarimeter	37
2.7 Development of the charge division method	39
2.7.1 Test experiment	39
2.7.2 Analysis scheme	40
2.7.3 Result and an additional analysis	40
2.7.4 Summary	42

2.8	Production	42
2.9	Read-out system for the polarimeter	44
2.9.1	16 ch Amp. Shaper Buffer card (ASB card)	44
2.9.2	VME discriminator board MODEL RPV-240	45
2.9.3	De-coupler card	46
2.9.4	CAEN ADC V792 / CAEN TDC V1190	47
3	Beam test at TRIUMF	48
3.1	M11 beamline	48
3.2	Preparation	51
3.2.1	Beam tuning	51
3.2.2	Experimental setup	54
3.2.3	Degrader tuning	58
3.3	Measurement	60
3.3.1	Null Asymmetry test	60
3.3.2	Analyzing power measurement	61
4	Analysis of the beam test data	63
4.1	Verification of data quality	63
4.2	Wire efficiency	67
4.3	Event selection	69
4.4	Development of the track reconstruction	70
4.5	Spurious asymmetry	73
4.5.1	Data analysis	73
4.5.2	Simulation	80
4.5.3	Summary of the asymmetry analysis	83
4.5.4	Future plan	84
5	Design of the Muon Tube Polarimeter	85
5.1	Estimates of Muon Tube parameters	86
5.2	Current status of MTP	87
6	K1.1BR beamline for the TREK experiment	91
6.1	Expected performance of K1.1BR	92
6.1.1	Design of beamline and optics	92
6.1.2	Pion contamination	95
6.1.3	Expected Kaon yield	96
6.2	Detectors for the beamline commissioning	97
6.2.1	beam detector elements	97
6.2.2	Fitch-type differential Cherenkov counter	99
6.3	Commissioning of the beamline	101
6.3.1	Result of the beam tuning	101
	Conclusion	106
	A Charge division	107

B An estimate of X-T relation 110

 B.1 Determination of the X-T relation 111

 B.2 Iteration method 112

C Beam polarization 118

List of Figures

1.1	The intensity distribution (a), and the three components of the muon polarization in the $K_{\mu 3}$ decay of (b)longitudinal component P_L , (c)normal component P_N , and (d)transverse component $P_T/\text{Im}\xi$ as defined by Eq(1.9).	6
1.2	Definition of P_T, P_N, P_L	7
1.3	Radiative corrections in the $K_{\mu 3}$ decay	9
1.4	(a) One of the diagrams of the final state interactions contributing to P_T^{em} ; from one photon exchange calculated in Ref [28] and (b) one of the diagrams from two photon exchanges calculated in Ref [29].	10
1.5	T-violating diagram in the three Higgs doublet model in $K_{\mu 3}$ decay. Interference between (a) W^+ exchange and (b) charged Higgs exchange is the main contribution.	12
1.6	T-violating diagram of Minimal Supersymmetric Standard Model in $K_{\mu 3}$ decay. 13	
1.7	T-violating diagram of R-parity breaking Supersymmetric Standard Model in $K_{\mu 3}$ decay, (a) and (b) are possible diagrams , (a) is a slepton exchange and (b) is a down-type squark exchange. Note that the diagram (c) does not exist.	14
1.8	Side view (top) and end view (bottom) of TREK detector	17
1.9	T-violating azimuthal polarization P_T for the case of the π^0 going in the forward (fwd) and backward (bwd) directions.	18
1.10	Scintillating fiber target for TREK experiment. The active zone has a length of 20 cm and a diameter of 7.5 cm. Each of the 489 fibers has $3.0\text{mm} \times 3.0\text{mm}$ square cross section. The fiber bundle is surrounded by 12 fiducial counters.	18
1.11	Example picture of scintillating fiber with two thin wave length shifter (WLS) fibers although an actual number of WLS is equal to 1.	18
1.12	CsI(Tl) barrel with 768 crystal modules. There are 12 muon holes.	19
1.13	Performance of the CsI(Tl) detector for $K_{\mu 3}$ and $K_{\pi 2}$ in E246. a) Invariant mass spectrum of two photons of $K_{\mu 3}$, b) cluster timing distribution also of $K_{\mu 3}$ showing the time resolution, c) opening angle distribution of $K_{\pi 2}$ showing the angular resolution, and d) two-photon and one-photon energy spectra of $K_{\mu 3}$ events.	20
1.14	Readout scheme of the CsI(Tl) calorimeter using APD	21
1.15	One sector of the superconducting toroidal magnet.	23
1.16	Schematics of the tracking system in the E246 setup (left) and the TREK setup (right)	25
1.17	Muon field magnet one sector test setup.	26

2.1	Schematic structure of the muon polarimeter.	29
2.2	Magnetic field distribution on the muon stopper	30
2.3	Incident muon y distribution in the stopper measured by the C4 chamber (top), and the intrinsic geometrical asymmetry for those muons (bottom). The real stopping distribution has a smearing due to beam divergence and multiple scattering. The geometrical asymmetry was measured as the null asymmetry A_0 by accepting all π^0 directions.	31
2.4	Muon stopper made of parallel plates which serve also as drift chamber cell structure.	36
2.5	Picture of 1/5 prototype polarimeter	39
2.6	Picture of 1/5 prototype polarimeter	39
2.7	(a) and (c) are RQ distributions and (b) and (d) are x distributions, respectively. (a) and (b) are ± 5 cm samples and (c) and (d) are ± 15 cm samples. The RQ distributions are obtained by adjusting the α . The x distributions are also obtained by adjusting the f parameter.	41
2.8	The residual distribution before correction (left) and the residual distribution after applying the additional correction (right) as discussed in the text. . .	41
2.9	Process of the wire stringing.	43
2.10	Picture of the FSM polarimeter.	43
2.11	Main flow of the data acquisition system.	44
2.12	Top view of ASB cards.	46
2.13	Overview of the modules for DAQ. The silver card on the bottom is one of the De-coupler cards. The four red modules are the interrupt register (left), the two ADC modules (center) and the TDC module (right), respectively. All the blue modules are VME-discriminator modules.	47
3.1	Overview of Meson Hall in TRIUMF.	48
3.2	M11 beam rate	49
3.3	Layout of M11 beam channel	50
3.4	Experimental setup for beam tuning.	51
3.5	Pictures of oscilloscope. The top one shows the S0 and the S1 counter signal which correspond to the yellow line and the blue line, respectively. The S1 counter signals appear 10 ns later than the S0 signals. On the other hand, the bottom one shows the $S0 \otimes S1$ and $S0 \otimes S1 \otimes RF$ corresponding to the yellow line and the blue line, respectively. $S1 \otimes RF$ coincidence signal has 3 components due to the three kinds of positive charged particles.	52
3.6	Pictures of TOF spectrum at 170 MeV/c by using the MCA. The top one shows the raw TOF spectrum showing three peaks for π , μ , and e . The bottom one shows the TOF spectrum after the RF cut. In the bottom one, pion peak including a little contamination of muons has been selected. . . .	53
3.7	Timing chart. The ADC gate was made from the coincidence of both the delayed trigger and the chamber signals. In addition, the TDC stop has the same timing as the end of the trigger gate.	54
3.8	Configuration of the DAQ system.	55
3.9	Typical chamber raw signal. It had an overshoot and some ringing.	55

3.10	Main flow diagram of the logic circuit.	56
3.11	Configuration of the gas system.	57
3.12	Configuration for degrader tunings.	58
3.13	Results of the degrader tuning. Upstream (top), Middle (middle), and Downstream (bottom).	59
3.14	Conceptual diagram for the null asymmetry test. In this measurement, the π^+ beam was used.	60
3.15	Conceptual diagram for analyzing power measurement. In this measurement, μ^+ beam was adopted.	61
4.1	Picture of the S1 counter time spectrum. This was used to be the time reference. A 170 ps in σ time resolution was achieved. This is sufficiently high in our measurement.	63
4.2	Picture of the muon decay curve. The parameter $(1/\tau)$ corresponds to $\sim 2\mu\text{s}$. 64	
4.3	Picture of the TDC data corresponding to a single wire. The TDC spectrum composed of the decay positron hit with a small fraction of the incident particle. 64	
4.4	Picture of the ADC data after a pedestal suppression. The figure corresponds to a single wire hit. The ADC spectrum is completely composed of the decay positron due to the delayed trigger as mentioned in Chapter 3.	65
4.5	Sample track. In this picture, the pion enters into polarimeter and the decay positron is finally emitted.	65
4.6	π^+ stopping distribution. It seems that incident pion stops ASB region with concentric circles. Its central position tends to concentrate upstream of the full ASB region.	66
4.7	Configuration of the Al plates (left) and the ASB cards (right).	67
4.8	The first results of the wire efficiency measurement. These efficiencies relied on the position of a sense wire due to multiple scattering effect.	68
4.9	Schematic view of the Al plates and the new definition of the wire efficiency. 68	
4.10	Final result of the detection efficiencies in a cell unit. This included the correction of the multiple scattering effect.	69
4.11	Schematic view of the track reconstruction.	70
4.12	Sample picture of the decay positron fitting 1.	72
4.13	Sample picture of the decay positron fitting 2.	72
4.14	Sample picture of the decay positron fitting 3.	72
4.15	Sample picture of the decay positron fitting 4.	73
4.16	Schematic view of the null asymmetry measurement and the definition of axis. 73	
4.17	Result of null asymmetry measurement. A large spurious asymmetry appears. It depend on the wire position.	74
4.18	Schematic view of the decay positron emission. The tendency shows that the positron tended to be emitted upward (downward) in case of a vertex cell located upward (downward).	75
4.19	Schematic view of pion decay in rest frame (left) and laboratory frame (right). 76	
4.20	Summary of properties of decay muons. Momentum distribution.	77
4.21	Summary of properties of decay muons. Decay-cone aperture angle for muons produced by pion decay in flight.	77

4.22	Three types of muon source (surface μ^+ , cloud μ^+ , and decay μ^+) produced by energetic protons from accelerators.	78
4.23	Schematic view of the M11 beamline. BWD muons could be produced after the B2 magnet.	79
4.24	TOF spectrum. BWD (FWD) muon could be contained in the pion peak toward the left (right) direction.	79
4.25	A polarimeter constructed in Geant4 simulation. In addition, main axes were also defined. Here, the incident beam was incoming toward the $-Z$ direction.	80
4.26	Incident π^+ beam profiles in Geant4 simulation	81
4.27	Features of the decay positron in Geant4 simulation	82
4.28	Result of the spurious asymmetry measurement in Geant4 simulation.	82
4.29	Schematic view of the cause of a spurious asymmetry.	83
5.1	Schematic view of the constraint against the Muon Tube. The tubes are aligned densely in the left one, while the tubes in the right one are aligned with a lower packing density.	87
5.2	$OD : ID = 10 : 9$	88
5.3	$OD : ID = 10 : 8$	88
5.4	$OD : ID = 10 : 7$	88
5.5	$OD : ID = 10 : 8.5$	88
5.6	Side view of Muon tube.	88
5.7	End view of Muon tube.	88
5.8	Full volume.	89
5.9	Buffer space.	89
5.10	Inner template.	90
5.11	Tube to template connector.	90
5.12	End plate.	90
5.13	Feedthrough.	90
5.14	The Al tubes assembling.	90
5.15	End plate connection.	90
5.16	Feedthroughs connection.	90
5.17	Process of the wire stringing.	90
6.1	Overview of the Hadron Hall at J-PARC	91
6.2	The layout of K1.1BR	92
6.3	Beam envelop of the current K1.1BR beamline. The top half and the bottom half corresponds to vertical and horizontal envelop, respectively.	94
6.4	Picture of the intermediate focusing slits ($IFX + IFY$) and the mass slit (MS) before installation. Both slits are located at the vertical focusing point. The IFY , in particular, has a crucial role for the removal of pions in spite of the use of a single stage separator. In addition, IFX is useful to control the overall beam acceptance.	94

6.5	Picture of the horizontal focusing slit (<i>HFOC</i>) before installation. The <i>HFOC</i> is placed before the final doublet $Q7 - Q8$ and is also useful for the removal of the pion contamination in the beam.	95
6.6	Picture of the electrostatic separator (<i>ESS</i>) before installation. The <i>ESS</i> is one of the essential elements for the beamline to extract a clean K^+ beam.	95
6.7	Detector components for the beam tuning.	97
6.8	Detector elements for the beamline commissioning.	98
6.9	Picture of the beam Hodoscope. The Hodoscope is composed of 24 scintillators with a thickness of 12 mm in a stainless steel frame.	98
6.10	Top view of the beam Cherenkov counter.	99
6.11	Side view and end view of the beam Cherenkov counter. The beam with 740-800 MeV/c momentum emits Cherenkov light with an angle of 38° for K^+ and 47° for π^+ . The critical angle of the radiator for total reflection is 42.2°	100
6.12	Distribution of PMT-hit K ring multiplicity @ 770 MeV/c in Monte Carlo simulation.	100
6.13	Distribution of PMT-hit π ring multiplicity @ 770 MeV/c in Monte Carlo simulation.	100
6.14	TOF spectrum. A large number of kaons were observed in the separated beam. We also see pions and protons in the spectrum. In this figure, the conditions that the π ring and K ring PMT hit multiplicity are equal to zero hit and more than 1 hit, were required, respectively.	102
6.15	The performance of the K ring. In this spectrum, the condition of the pion timing confirmed by the TOF spectrum above is required. Thus, the figure shows the pion fraction in the K ring.	102
6.16	The performance of the K ring. In this spectrum, the condition of the kaon timing confirmed by the TOF spectrum above is required. Thus, the figure shows the real kaon events.	103
6.17	The performance of the π ring. In this spectrum, the condition of the pion timing confirmed by the TOF spectrum above is required. Thus, the figure shows the real pion events.	103
6.18	Mass separation curve obtained with a <i>ESS</i> voltage of ± 300 kV at the beam momentum of 0.8 GeV/c.	104
6.19	Kaon beam spot at the FF for the best tuning setting of $Q7$ and $Q8$, and at the end of $Q8$ using a beam Hodoscope.	105
A.1	The schematic view of charge division system. The distance from avalanche to wire ends are Z_1 and Z_2 , and the corresponding resistances of the wire are R_1 and R_2 , respectively. The input impedance of amplifiers are r_1 and r_2	107
A.2	Equivalent electric circuit of the charge division system. The collected charge on capacitor is discharged through resistances. The experimentally time-integrated I_1 and I_2 are observed as the charges Q_1 and Q_2	108
B.1	Drift time distribution. The sweep of the drift time distribution corresponded to a cell size.	110

B.2	Schematic view of the definition of wires for analyzing the X-T relation. The same configuration of wires was adopted in my analysis.	111
B.3	2-Dimensional plot of the X-T relation based on 50 $\mu\text{m}/\text{ns}$ drift velocity. The resulting plot shows that drift velocity was not constant.	112
B.4	Sample of projected histogram. These products were fitted by Gauss function.	113
B.5	Result of fitting with an assumed parameter. At the same time, the value of χ^2 was recorded every time.	114
B.6	The variation of χ^2 . The value of χ^2 converged after several iterations. . .	115
B.7	Final result of parameters corresponding to actual drift velocity.	115
B.8	A final set of the projected histograms and the 2-Dimensional X-T plot. The mean value of the histogram is shifted toward the right direction and the value of sigma is becoming smaller.	116
B.9	The variation of σ . The resulting parameters were adopted as the fluctuation of the equi-drift-time line.	117
C.1	Conceptual diagram of the longitudinal polarization measurement.	118
C.2	Asymmetry of the longitudinal polarization measurement.	119

List of Tables

1.1	Main parameters of the CsI(Tl) calorimeter.	20
1.2	Readout scheme using APDs compared with the E246 PIN readout.	22
1.3	Main parameters of the charged particle tracking	24
1.4	Main parameters of the muon field magnet	26
2.1	Summary of major systematic errors	33
2.2	Parameters of plate and wire	35
2.3	List of μ SR target	38
2.4	The main functions of ASB	45
2.5	Gain control set	45
2.6	The specs of VME discriminator board	46
3.1	Summary of degrader thickness	60
5.1	Parameter comparisons of the plate type.	86
6.1	Main parameters of the beam Cherenkov counter. The K^+ momentum is expected to be 740-800 MeV/c. The K^+ efficiency is obtained to be higher than 99 % by setting the threshold multiplicity of $N > 6$	99
6.2	Results of the K^+ beam tuning at 0.8 GeV/c at K1.1BR.	104

Introduction

In the field of elementary particle physics, it is essential to search for what kinds of materials (or particles) is our universe composed of and how they build up our universe. For proceeding with our understandings, a lot of elementary particle physics experiments were performed around the world.

As the results of these investigations, the electroweak model was accomplished as well as quantum chromodynamics (QCD). Finally, the elementary particle Standard Model (SM) [1, 2] based on the Cabibbo-Kobayashi-Masukawa mixing matrix (CKM matrix) was proposed. The SM consists of the quarks and the leptons with three generations in addition to the gauge bosons based on the gauge principle such as W, Z, and γ bosons for the interactions as the elementary particles. It is generally said that the SM has also another elementary particle, named Higgs boson for the vacuum description although it has not yet been discovered. However, it is expected to be probably discovered in the mass region of $110 < M_H < 200$ GeV in the near future. The SM successfully explains the various phenomena in our universe, especially regarding the particles and their interactions precisely, and was consistent with a lot of particle and nuclear physics experiments.

At the same time, it is a well-known fact that the SM can not be the ultimate theory, namely it may just explain a comparatively low energy scale ($\sim TeV$). Thus, particle and nuclear physicists hope that new physics beyond the SM lies at the energy region of a few TeV, in the light of the following problems given as examples.

- Neutrino mass problem
Neutrinos have actually a small mass (meV-eV) although neutrinos are dealt with massless particles in the SM. Although the problem was accounted for as the neutrino oscillation [3], the oscillation parameters have not been determined precisely yet.
- Hierarchy problem [4]
This is the question that asks why the Higgs boson is so much lighter than the Planck scale (or the grand unification energy scale).
- Baryogenesis problem [5]
This is the question that asks why our universe mainly consists of not antibaryons but baryons.
- Dark matter and dark energy problem [6]
Although it is said that our universe mainly consists of the dark matter and the dark

energy, they have not yet been discovered.

For explaining these unknown phenomena, theoretical physicists have made up a lot of new theories. As the most important possibility, some of them believe that the existence of the super symmetry theory (SUSY) [7] which predicts the partner particles for all of the SM particles. The SUSY will be possible to solve all problems above. The existence of the SUSY particles assumed, for example, the Yukawa coupling of the top quark can generate electroweak scale naturally.

As well as the theoretical physicists, we, namely experimental physicists, have planned a lot of new experiments with the aim to search for new physics beyond the SM. One of the most noteworthy experiments is the Large Hadron Collider (LHC) experiment [8]. In the LHC, where energy frontier physics can be performed, it is possible to search for the new particles such as the Higgs boson and the SUSY particles beyond the SM, directly up to TeV scale. It is said (and I hope) that the LHC will discover the Higgs boson because the LHC will be cover the mass region of $110 < M_H < 200$ GeV in the near future. In addition, neutrino oscillation experiments and next-generation B factory experiments are also undertaken.

In Japan, we give high priority to the T2K experiment [9] and the BELLE experiment [10] as the large experimental projects. The T2K project in J-PARC [11] aims to measure one of the neutrino oscillation parameters and the experiment has already started. And the BELLE experiment in KEK, where the highest luminosity beam is available, has already measured the CP violation, which was discovered in the neutral kaon system in 1964 [12], corresponding to the CKM matrix phase in the asymmetric decay timing of the B^0 system in 2001.

As well as these experiments, it is clear that we should also perform the kind of precise measurement at J-PARC using kaons such as the KOTO experiment [13], which aims to measure the rare decay of neutral kaons $K_L \rightarrow \pi^0 \nu \bar{\nu}$, the TREK experiment [14], which aims to measure the transverse polarization (P_T) corresponding to the T-violation, and the P36 experiment, which aims to measure the lepton universality using $\Gamma(K_+ \rightarrow e^+ \nu) / \Gamma(K^+ \rightarrow \mu^+ \nu)$, are also of great importance not only in the search for new physics but also to proceed with our understandings of new physics.

Since baryogenesis as a generic term produced an asymmetry between baryons and antibaryons in the very early universe, the universe today is composed of the substantial amounts of residual matter. In order to generate its term, a set of three conditions, the so-called A. Sakharov conditions, are required.

- 1) Baryon number violation
- 2) C-symmetry and CP-symmetry violation
- 3) Interactions out of thermal equilibrium

Currently, there is no experimental evidence of the particle interactions, where the

conservation of baryon number is broken. In addition, although the CP violation completely corresponds to the CKM matrix complex phase in the quark sector, larger CP violations are required in order to explain baryogenesis. Therefore it is essential to examine new CP violation sources.

The CPT theorem [15] asserts that a Lorentz-invariant field theory is unchanged under the combined CPT operation, thus conserving CPT. According to the CPT invariance, however, the observation of the CP violation in the K^0 and B^0 systems requires the existence of T violation. Thus, T violation has a great impact on our understanding of nature. Before the first observation of T-violation by the CPLEAR experiment in 1988 [16], the T-violation was regarded as the kind of statistical fluctuation due to an increase of entropy in our universe. The observation means that the T-violation can be explained as the result of particle interactions. I was surprised at this fact, and at the same time I was so shocked because we have no way to go back to the past of our universe although we can often go back to the past in some kind of Science Fiction (SF) movie.

A large number of experiments to search for T-violating effects have been performed such as the particle and the nuclear electro dipole moment (EDM) experiments [17]. On the other hand, we aim to measure the effect in $K^+ \rightarrow \pi^0 \mu^+ \nu_\mu (K_{\mu 3})$. More than 50 years ago it was suggested by J. Sakurai [18] that the nonzero transverse polarization (P_T) of the muon in $K_{\mu 3}$ decay would be a definite signature of the T violation. Therefore, we want to test if the polarization of the muons perpendicular to the kaon decay plane is nonzero. The system has several advantages such as the smallness of the final-state interactions which can mimic T violation by inducing a T-odd effect.

The search of P_T has been performed at the KEK-PS North Hall in KEK as the E246 experiment [19]. As the result of the E246 experiment, $P_T = -0.0017 \pm 0.0023(stat) \pm 0.0017(syst)$ [20] was obtained as the world record, and the result was consistent with no T-violation.

Now we are preparing to perform the TREK experiment. The TREK experiment aims to search for the T-violation with a sensitivity of $P_T \sim 10^{-4}$. In this sensitivity, we will be able to discover the new physics beyond the SM. In chapter 1, I will describe the new physics which will be covered by the TREK experiment, and I will also describe some detector components for TREK.

For the TREK experiment, the muon polarimeter, which will measure the muon transverse polarization directly, is one of the most essential detectors. The polarimeter has been studied in my responsibility such as manufacturing of the prototypes, preparation of the beam test, as well as analysis of the data including some simulations. Here, I will summarize the status of the muon polarimeter in the chapters as described below.

In Chapter 2, some requirements of the polarimeter will be described.

In Chapter 3, the outline of the beam test in TRIUMF [21] will be described.

In Chapter 4, some analyses based on the beam test data will be described.

In Chapter 5, a new design of the polarimeter based on the beam test analysis will be described.

In fact, I have participated in the other test experiments for the TREK experiment. For evaluating the kind of APD readout as one of the new candidate for the CsI(Tl) calorimeter, we have also done a beam test at ELPH in Tohoku University.

Furthermore, I have also taken part in the commissioning of the K1.1BR beamline at the Hadron Experimental Hall in J-PARC. Last autumn, the K1.1BR beamline started its operation for the first time. There, I have prepared and tuned all the detectors, for example MWPCs, Gas Cherenkov detector, Hodoscope counter, Fitch Cherenkov detector, and TOF counters, for measuring the K/pi ratio and the kaon yield. In addition, I have tuned all the K1.1BR magnets downstream from the proton target along with our collaborators.

Thus, in Chapter 6, I will describe the status and the result of K1.1BR beam commissioning.

It was actually impossible to write everything on which I have worked for the TREK experiment due to time constraints. Thus, I will describe the development of the polarimeter mainly.

Chapter 1

J-PARC TREK Experiment

1.1 Phenomenology of $K_{\mu 3}$ Decay

The matrix element for $K_{\mu 3}$ decay in the standard form of the V-A theory can be written as [22, 23]

$$M \propto \frac{G_F}{2} \sin \theta_c [f_+(q^2)(p_K^\lambda + p_\pi^\lambda) + f_-(q^2)(p_K^\lambda - p_\pi^\lambda)] \times [\bar{u}_\mu \gamma_\lambda (1 - \gamma_5) u_\nu], \quad (1.1)$$

with two form factors $f_+(q^2)$ and $f_-(q^2)$ of the momentum transfer squared to the lepton pair, $q^2 = (p_K - p_\pi)^2$. Here, G_F is the Fermi constant, θ_c is the Cabibbo angle, p_K , p_π , p_μ , and p_ν are the four-momenta of the kaon, pion, muon, and antineutrino, respectively. Using $p_K = p_\pi + p_\mu + p_\nu$, Eq(1.1) can be rewritten as

$$M \propto \frac{G_F}{2} \sin \theta_c [f_+(q^2)(p_K^\lambda + p_\pi^\lambda) \bar{u}_\mu \gamma_\lambda (1 - \gamma_5) u_\nu + f_-(q^2) m_\mu \bar{u}_\mu (1 - \gamma_5) u_\nu] \quad (1.2)$$

$$= \frac{G_F}{2} \sin \theta_c f_+(q^2) [2p_K^\lambda \cdot \bar{u}_\mu \gamma_\lambda (1 - \gamma_5) u_\nu + (\xi(q^2) - 1) m_\mu \bar{u}_\mu (1 - \gamma_5) u_\nu]. \quad (1.3)$$

The parameter $\xi(q^2)$ is defined as

$$\xi(q^2) = f_-(q^2)/f_+(q^2). \quad (1.4)$$

The first term of Eq(1.2) corresponds to the vector and axial vector amplitude, and the second term corresponds to the scalar and pseudo-scalar amplitude. Both f_+ and f_- can, in general, be complex, but if T invariance holds, then the parameter ξ should be a real number. Hence, any nonzero value of $\text{Im}\xi$ would imply T violation. The form factors f_- and f_+ depend on q^2 as

$$f_\pm(q^2) = f_\pm(0)[1 + \lambda_\pm(q/m_\pi)^2], \quad (1.5)$$

where the currently adopted values [23] of λ_+ and $\xi(0)$ are

$$\begin{aligned} \lambda_+ &= 0.0284 \pm 0.0027 \\ \xi(0) &= -0.14 \pm 0.05 \end{aligned} \quad (1.6)$$

and $\lambda_- = 0$, namely, a constant f_- .

The Dalitz distribution for $K_{\mu 3}$ decay is given by [23]

$$\rho(E_\pi, E_\mu) \propto f_+^2 [A + B\xi(q^2) + C\xi^2(q^2)], \quad (1.7)$$

with

$$\begin{aligned} A &= m_K(2E_\mu E_\nu - m_K E'_\pi) + m_\mu^2 \left(\frac{1}{4} E'_\pi - E_\nu\right) \\ B &= m_\mu^2 \left(E_\nu - \frac{1}{2} E'_\pi\right) \\ C &= \frac{1}{4} m_\mu^2 E'_\pi \\ E'_\pi &= (m_K^2 + m_\pi^2 - m_\mu^2)/(2m_K) - E_\pi \end{aligned} \quad (1.8)$$

Here, E_π , E_μ , and E_ν are the pion, muon, and neutrino energies in the kaon center-of-mass frame, respectively, and m_K , m_π , and m_μ are the kaon, pion, muon masses, respectively. The Dalitz distributions are shown in Fig(1.1)(a).

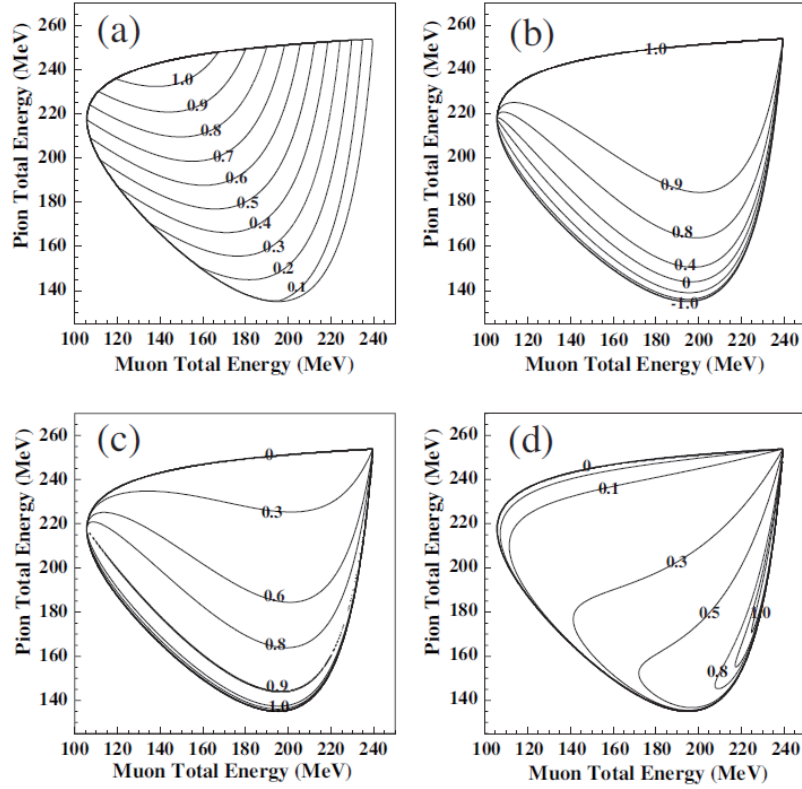


Figure 1.1: The intensity distribution (a), and the three components of the muon polarization in the $K_{\mu 3}$ decay of (b)longitudinal component P_L , (c)normal component P_N , and (d)transverse component $P_T/\text{Im}\xi$ as defined by Eq(1.9).

1.2 Transverse Polarization P_T

In general, one can define three orthogonal components of the muon polarization vector: the longitudinal(P_L), normal(P_N), and transverse(P_T) as the component parallel to the muon momentum \vec{P}_μ , the component transverse to P_L in the decay plane, and the component normal to the decay plane, respectively. The directions of P_L , P_N and P_T are schematically shown in Fig(1.2).

They are expressed as

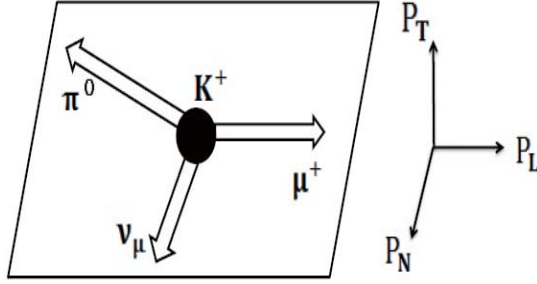


Figure 1.2: Definition of P_T , P_N , P_L

$$\begin{aligned}
 P_L &= \frac{\vec{\sigma}_\mu \cdot \vec{p}_\mu}{|\vec{p}_\mu|} \\
 P_N &= \frac{\vec{\sigma}_\mu \cdot (\vec{p}_\mu \times (\vec{p}_\pi \times \vec{p}_\mu))}{|\vec{p}_\mu \times (\vec{p}_\pi \times \vec{p}_\mu)|} \\
 P_T &= \frac{\vec{\sigma}_\mu \cdot (\vec{p}_\pi \times \vec{p}_\mu)}{|\vec{p}_\pi \times \vec{p}_\mu|}
 \end{aligned} \tag{1.9}$$

with the polarization vector $\vec{\sigma}_\mu$. Using the decay probability Eq(1.7), the muon polarization in the kaon rest frame can be written as [22, 23]

$$\vec{\sigma}_\mu = \vec{A}/|\vec{A}|, \tag{1.10}$$

where \vec{A} is determined as follows:

$$\begin{aligned}
 \vec{A} &= (a_1(\xi) - a_2(\xi))[(m_K - E_\pi) \\
 &\quad + (E_\mu - m_\mu)(\vec{p}_\pi \cdot \vec{p}_\mu)/|\vec{p}_\mu|^2] \vec{p}_\mu - a_2(\xi)m_\mu \vec{p}_\mu \\
 &\quad + m_K m_\mu \text{Im}(\xi)(\vec{p}_\pi \times \vec{p}_\mu).
 \end{aligned} \tag{1.11}$$

Here,

$$\begin{aligned}
 a_1(\xi) &= 2m_K^2 [E_\nu + \text{Re}(b(q^2))(E_\pi^* - E_\pi)] \\
 a_2(\xi) &= m_K^2 + 2\text{Re}(b(q^2))m_K E_\mu + |b(q^2)|^2 m_\mu^2 \\
 b(q^2) &= \frac{1}{2}[\xi(q^2) - 1] \\
 E_\pi^* &= (m_K^2 + m_\pi^2 - m_\mu^2)/(2m_K).
 \end{aligned} \tag{1.12}$$

These three polarization components are shown in Fig(1.1)(b)-Fig(1.1)(d). One has to look for P_T in the presence of the predominant in-plane component of the polarizations, P_L and P_N . P_T can be further written as an explicit product of $\text{Im}\xi$ and a kinematical factor as

$$P_T = \text{Im}\xi \cdot \frac{m_\mu}{m_K} \frac{|\vec{p}_\mu|}{[E_\mu + |\vec{p}_\mu| \vec{n}_\mu \cdot \vec{n}_\nu - m_\mu^2/m_K]}. \quad (1.13)$$

The quantity $\text{Im}\xi$, which is sensitive to T-violation, can be determined from a P_T measurement. The advantage of $K_{\mu 3}$ over $K_{e 3}(k^+ \rightarrow \pi^0 e^+ \nu_\mu)$ is apparent as P_T is proportional to the lepton mass.

$$\langle P_T \rangle \sim 0.3 \text{Im}\xi. \quad (1.14)$$

It is of interest to establish the connection between the $\text{Im}\xi$ and effective parameters of new physics appearing in the coefficients of generic exotic interactions. To this end, an effective four fermion Lagrangian can be used:

$$\begin{aligned} L = & -\frac{G_F}{\sqrt{2}} \sin \theta_C \bar{s} \gamma_\alpha (1 - \gamma_5) u \bar{\nu} \gamma^\alpha (1 - \gamma_5) \mu \\ & + G_S \bar{s} u \bar{\nu} (1 + \gamma_5) \mu + G_P \bar{s} \gamma_5 u \bar{\nu} (1 + \gamma_5) \mu \\ & + G_V \bar{s} \gamma_\alpha \bar{u} \nu \gamma^\alpha (1 - \gamma_5) \mu + G_A \bar{s} \gamma_\alpha \gamma_5 u \bar{\nu} \gamma^\alpha (1 - \gamma_5) \mu + h.c.. \end{aligned} \quad (1.15)$$

here, G_S and G_P are the scalar and pseudo-scalar coupling constants and G_V and G_A are the exotic vector and axial-vector coupling constants, respectively. Tensor interactions are neglected. $\text{Im}\xi$ is found to be caused only by the interference between the SM term and the scalar term, namely by the complex phase of G_S [24, 25], which can be written as

$$\text{Im}\xi = \frac{(m_K^2 - m_\pi^2) \text{Im} G_S^*}{\sqrt{2} (m_s - m_u) m_u G_F \sin \theta_C}, \quad (1.16)$$

where m_s and m_u are the masses of the s-quark and u-quark, respectively. Thus, measurements of the P_T can constrain the exotic scalar interactions.

1.3 Theoretical Predictions

The amplitude of the T-violating transverse muon polarization has been estimated in various theoretical models. In this section, I will briefly describe several models which might lead to a sizable P_T value. I will also give a more general discussion based on the effective field theory to clarify the difference of P_T physics from other T and CP violating observables.

1.3.1 Standard Model

A T-violating amplitude arises from the relative phases between diagrams or complex coupling constants in a diagram. Since only a single element of the Cabibbo-Kobayashi-Masukawa matrix V_{us} is involved in the W-exchanging semi-leptonic $K_{\mu 3}$ decay in the SM, no CP violation appears in first order. [26] The lowest order contribution comes from radiative corrections to the $\bar{u}\gamma_\mu(1 - \gamma_5)sW^\mu$ vertex as shown in Fig(1.3) is presented in the textbook of Bigi and Sanda [27]. This has been estimated to be less than 10^{-7} .

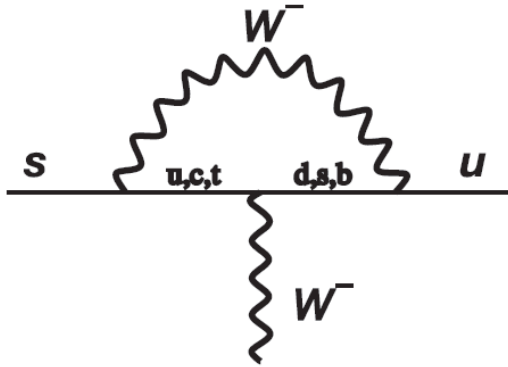


Figure 1.3: Radiative corrections in the $K_{\mu 3}$ decay

1.3.2 Final state interactions

Strictly speaking, a measured non-zero value of a T-odd observable does not automatically mean T-violation. Spurious P_T^{em} can be induced by electromagnetic final-state interactions(FSI). This has been a concern in P_T experiments for quite some time. In the case of $K_{\mu 3}$ decays, the FSI are mainly due to electromagnetic interactions. Since the FSI contributions to P_T in the present case are much smaller than those in $K^0_{\mu 3}$ decay, where the two charged particles can interact in the final state and $P_T^{em} \sim 10^{-3}$, this effect may limit the sensitivity for T violation and it has been extensively investigated. The single-photon contribution to P_T^{em} that arises in this decay due to the imaginary part of the two-loop diagram was estimated more than 20 years ago as $P_T^{em} \leq 10^{-6}$ [28]. An example is shown in Fig(1.4)(a). More recently, two-photon exchange contributions to P_T^{em} have also been studied in Ref [29], where the transverse polarization is proportional to the imaginary part of the diagrams shown in Fig(1.4)(b). The average value of P_T^{em} over the Dalitz plot was concluded to be less than 10^{-5} . Thus, a nonzero P_T in the range of $\sim 10^{-3} - 10^{-4}$ would

unambiguously imply the existence of a new physics contribution.

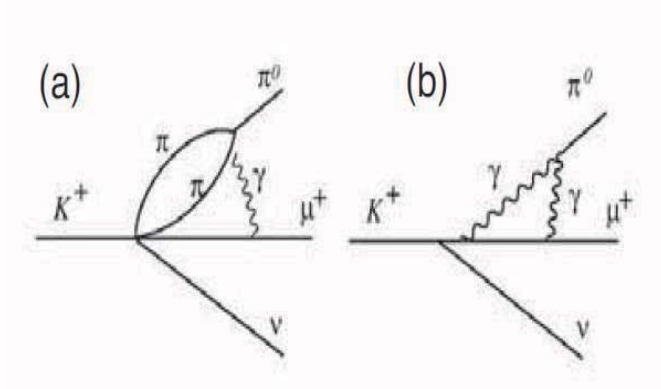


Figure 1.4: (a) One of the diagrams of the final state interactions contributing to P_T^{em} ; from one photon exchange calculated in Ref [28] and (b) one of the diagrams from two photon exchanges calculated in Ref [29].

1.3.3 Multi-Higgs doublet model

As the minimum and natural extension of the SM with one Higgs doublet, multi-Higgs doublet models have been considered [30, 31, 32, 33, 34, 35, 36, 37, 38] as one of the promising candidate theories for non-zero P_T . This model was originally proposed by S.Weinberg [39]. One doublet is for up-type quarks, one for down-type quarks, and one for leptons. This Higgs generation number does not allow for flavor changing neutral current (FCNC). To avoid the FCNC, Weinberg proposed natural flavor conservation (NFC), which requires that all fermions couple to only one kind of Higgs doublet. With the NFC, it is well-known that at least three Higgs doublets are needed to generate CP violation. In the class of models without tree-level FCNC, new CP violating phases are introduced,

- 1) in the complex phase of CKM,
- 2) in the complex charged Higgs mixing matrix,
- 3) in the neutral-Higgs mixing matrix.

Here, 1) and 2) are associated with the CP violation in the $K_{\mu 3}$ decay. The coupling of quarks and leptons to the charged Higgs boson is expressed in terms of the Lagrangian [30, 31]

$$L = (2\sqrt{2}G_F)^{\frac{1}{2}} \sum_{i=1}^2 [\alpha_i \bar{u}_L V M_D d_R H_i^+ + \beta_i \bar{u}_R M_U V d_L H_i^+ + \gamma_i \bar{\nu}_L M_E e_R H_i^+] + h.c., \quad (1.17)$$

where M_D , M_U , M_E are diagonal mass matrices, V is the CKM matrix, and α_i , β_i and γ_i are the new complex coupling constants associated with the charged Higgs interactions.

For three doublet case the NFC can be arranged. In this model CP symmetry can also be broken spontaneously due to the complex phases of the vacuum expectation values

of the Higgs fields. The coefficients, α_i , β_i and γ_i can have complex phases, and P_T is calculated as

$$\text{Im}\xi = \frac{m_K^2}{m_H^2} \text{Im}(\gamma_1 \alpha_1^*), \quad (1.18)$$

where α_1 and γ_1 are the quark and lepton couplings to the lightest charged Higgs boson. The E246 result [40] yielded $|\text{Im}\xi(\gamma_1 \alpha_1^*)|/m_H^2 < 0.066(\text{GeV})^{-2}$ (90 % C.L.) as the most stringent limit for this parameter. It is also constrained by the semi-leptonic decay of the B meson [41], $B \rightarrow \tau \nu X$, but the result is less stringent than the P_T constraint. The recent result of $B \rightarrow \tau \nu$ published by the BELLE collaboration in Oct 2010 [42] is also less constrained due to a large uncertainty of the theoretical calculation for the SM branching ratio. Suppose that the TREK will achieve 20 times higher sensitivity of P_T than the E246 result, the TREK will give 10 times stronger constraint directly against this parameter.

Other constraints to this model come from the neutron EDM (d_n), $b \rightarrow s\gamma$ [41] and $b \rightarrow s\bar{l}l$ [43] complementing the P_T result in a different manner, since these channels limit $\text{Im}(\alpha_1 \beta_1^*)$.

These two parameters are related as $\text{Im}(\alpha_1 \beta_1^*) = -(v_3/v_2)^2 \text{Im}(\gamma_1 \alpha_1^*)$ through the ratio of the vacuum expectation values v_2 and v_3 . An interesting scenario assumed in Ref [30] is $v_3/v_2 \sim m_\tau/m_t \sim 1/80$ thus making P_T the most sensitive test of the three Higgs doublet model over d_n and $b \rightarrow s\gamma$.

The important feature of this model is the prediction of P_T in the radiative decay $K^+ \rightarrow \mu^+ \nu \gamma (K_{\mu\nu\gamma})$. The following expression was obtained [24],

$$P_T(K_{\mu\nu\gamma}) \cong -0.1 \frac{m_K^2}{m_H^2} \text{Im}\xi(\gamma_1 \alpha_1^*), \quad (1.19)$$

with the same parameter as $P_T(K_{\mu 3})$ but with different size and sign. The E246 provided a result [44] but with less statistics. Although the final state interaction is large and on the order of 10^{-3} we may pursue this mode also at J-PARC in the future.

Furthermore, it is essential to compare the P_T with the collider experiments, in particular the LHC. If the LHC finds the charged Higgs boson, the P_T measurement will be important to look for associated CP violating couplings. Provided that a MSSM Higgs boson is discovered with 5σ significance after an integrated luminosity of 30 fb^{-1} , the discovery of this would yield a value of $\tan\beta/m_{H^+} \geq 0.06(\text{GeV})^{-1}$. If this limit is applied to the lightest charged Higgs boson with regard to the multi-Higgs model, the P_T corresponds to $|P_T| < 3 \times 10^{-4}$. This roughly corresponds to the sensitivity of the TREK experiment.

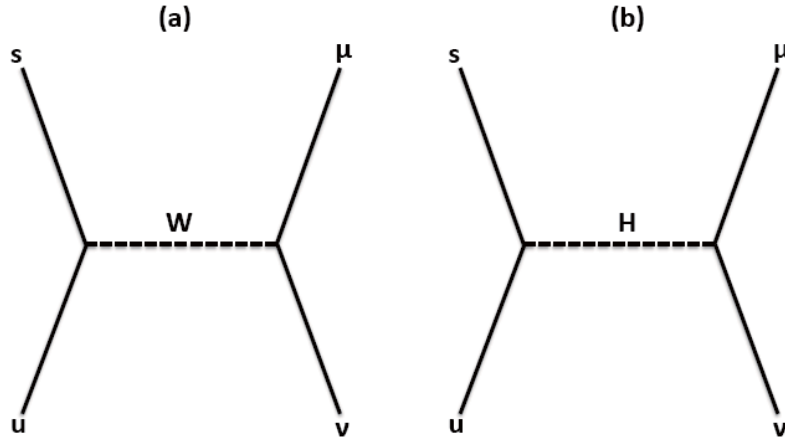


Figure 1.5: T-violating diagram in the three Higgs doublet model in $K_{\mu 3}$ decay. Interference between (a) W^+ exchange and (b) charged Higgs exchange is the main contribution.

1.3.4 SUSY models

A number of other models also allow P_T at observable level without conflicting with other experimental constraints. Supersymmetric models have attracted many physicist, since it offers the natural unification of strong and electroweak interactions, and a natural solution to the mass hierarchy problem. However, the current experimental information of these models is not sufficient. Thus, intensive experimental researches have been devoted to study the model. Some MSSM models allow sizable values of P_T .

In the MSSM, we require R-parity conservation.

$$R \equiv (-1)^{3B+L+2S} \quad (1.20)$$

where B, L and S are baryon number, lepton number and intrinsic spin of the particle, respectively. $R = +1$ for the ordinary particles and $R = -1$ for their superpartners are assigned. Thus, if R-parity is conserved, superparticles are produced in pairs. In addition, it ensures the stability of the proton and the stability of the lightest superparticle (LSP), which is one of the candidates for dark matter in our universe.

One interesting case is the MSSM discussed by G.-H. Wu and J.N. Ng [45]. In this model the complex coupling constant between the charged Higgs boson and s-quarks and u-quarks is induced through squark and gluino loops. The P_T value, when the muon and neutrino momenta are at right angles, is given as

$$P_T^{H^+} \approx 3.5 \times 10^{-3} I_{H^+} \frac{p_\mu (\mu + A_t \cot \beta)}{E_\mu m_g} \frac{(100\text{GeV})^2 \text{Im}[V_{33}^{H^+} V_{32}^{D_L^*} V_{31}^{U_R^*}]}{M_H^2 \sin \theta_C} \quad (1.21)$$

for $\tan \beta \approx 50$. If we allow large flavor mixing coupling in the squark-quark vertices, there is an allowed parameter region for large P_T . The E246 P_T upper bound corresponds

to $M_H > 140\text{GeV}$. In the view of several assumptions made, this boundary should be considered as a qualitative estimate. It is noteworthy that $P_T(K_{\mu 3})$ and $P_T(K_{\mu\nu\gamma})$ have opposite signs in this model.

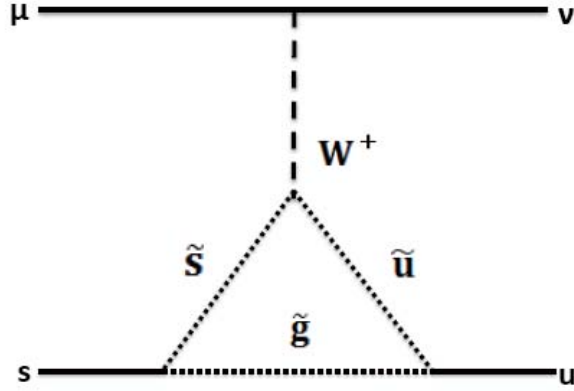


Figure 1.6: T-violating diagram of Minimal Supersymmetric Standard Model in $K_{\mu 3}$ decay.

SUSY with R-parity violation

On the other hand, if R-parity is not conserved, the situation is completely changed. Under such conditions, single production of superparticles becomes possible. According to one of the R-parity violating models [46], the superpotential which breaks R-parity can be written as

$$W = \lambda_{ijk} L_i L_j E_k^c + \lambda'_{ijk} L_i Q_j D_k^c + \lambda''_{ijk} U_i^c D_j^c D_k^c, \quad (1.22)$$

where λ_{ijk} , λ'_{ijk} , λ''_{ijk} are coupling constants with i, j, k being family indices. L_i , E_i , Q_i , (U_i^c, D_i^c) denote superfields of the left-handed lepton doublets, lepton singlets, left-handed quark doublets and singlets, respectively. Here, $\lambda_{ijk} = -\lambda_{jik}$ and $\lambda''_{ijk} = -\lambda''_{jik}$. The first and second terms represent lepton-number violation, the third term is baryon-number violation. It has been well known that there is a very tight constraint on λ''_{ijk} from non-observation of proton decay. For this reason, R-parity was originally introduced to the MSSM. It would be easier to understand the R-parity breaking interaction, if the corresponding Lagrangian is given from Eq(1.22). First, let us assume $\lambda''_{ijk} = 0$, because of non-observation of proton decays. For the non-zero λ_{ijk} and λ'_{ijk} , the corresponding Lagrangian is given by

$$\begin{aligned} L = & \frac{1}{2} \lambda_{ijk} [\bar{\nu}_{Li}^c e_{Lj} \tilde{e}_{Rk}^* + \bar{e}_{Rk} \nu_{Li} \tilde{e}_{Li} - (i \leftrightarrow j)] \\ & + \lambda'_{ijk} [\bar{\nu}_{Li}^c d_{Lj} \tilde{d}_{Rk}^* + \bar{d}_{Rk} \nu_{Li} \tilde{d}_{Rj} + \bar{d}_{Rk} d_{Lj} \tilde{\nu}_{Li} \\ & - \bar{e}_{Ri}^c u_{Lj} \tilde{d}_{Rk}^* - \bar{d}_{Rk} e_{Li} \tilde{u}_{Lj} - \bar{d}_{Rk} u_{Lj} \tilde{e}_{Li}] + h.c., \end{aligned} \quad (1.23)$$

where the tilde denotes the scalar fermion superpartners. The subscripts of R and L are right-handed and left-handed, respectively. This Lagrangian describes possible R-parity breaking couplings. Eq(1.23) shows that tree level contributions are allowed in the diagrams of P_T in $K_{\mu 3}$ decay. Typical diagrams are shown in Fig(1.7). Thus, it could give large contributions to P_T . Theoretical calculations predict P_T of the order of 10^{-3} .

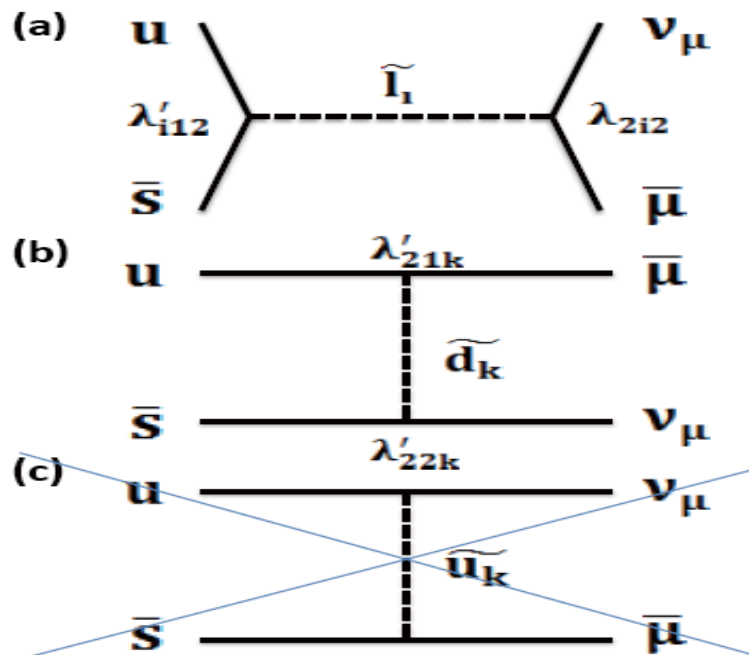


Figure 1.7: T-violating diagram of R-parity breaking Supersymmetric Standard Model in $K_{\mu 3}$ decay, (a) and (b) are possible diagrams , (a) is a slepton exchange and (b) is a down-type squark exchange. Note that the diagram (c) does not exist.

1.4 J-PARC TREK experiment

Considering the current experimental situation of direct CP violation (or direct T-violation) studies and searches for new physics, we believe that it is essential to perform a P_T measurement in $K_{\mu 3}^+$ at J-PARC, which offers much superior experimental environment. The transverse muon polarization (P_T) in $K_{\mu 3}$ decay is one of the best indicators for the direct T-violation. In addition, it can be a better probe to search for new physics, in particular new CP violation source, beyond the SM with less background than any other probe of P_T .

In terms of the fact that currently there is no P_T experiment beyond the E246 limit around the world, we think that this P_T experiment ranks high among the particle physics experiments in the low energy region. Hence, we should be responsible for the P_T experiment as a leading group and we will perform the TREK experiment in J-PARC.

The crucial merits of the TREK experiment compared with the E246 experiment are as follows.

1) In a case that the TREK experiment runs for nearly 1 year with ~ 270 kW proton intensity, a large number of K^+ events, which corresponds to more than ≥ 100 times as high as the E246 experiment, will be available though the E246 experiment was limited by the statistical error. In addition, as we employ an active polarimeter, the analyzing power is more than 2 times higher than the E246 experiment. This means that eventually we will be able to improve the sensitivity of the P_T up to more than ≥ 20 times as high as the E246 experiment even considering the fact that the statistical sensitivity of asymmetry measurements scales as $1/\sqrt{N}$.

2) Along with an uncertainty of statistics, we must reduce systematic errors in the E246, which is summarized in Table(2.1), at least by one order of magnitude in order to achieve the sensitivity of $\sim 10^{-4}$. For accomplishing the sensitivity above, we have to upgrade the E246 detectors.

- New polarimeter system (an active polarimeter + muon polarimeter magnet) is adopted to reduce the μ^+ multiple scattering and an uncertainty of the magnetic field in the polarimeter.
- New electronics and read-out, in particular CsI(Tl) read-out, systems will be adopted to handle the higher event rates.
- Additional tracking GEM chambers for charged particle is adopted for improving an uncertainty of the determination of decay planes.
- A slimmer target with finer segmentation is adopted in order to improve an uncertainty of the K^+ stop position.

We plan to perform the TREK experiment using the K1.1BR beamline at Hadron Experimental Hall in J-PARC in 2015 - 2016. At present we are waiting for the realization

of accelerator high power operation (currently ~ 5 kW intensity beam for slow extraction is available.), and after finishing another experiment (P36) at K1.1BR which can be performed with lower accelerator power, we will start to perform the TREK experiment. The preparation of all the detectors is in progress. In the next section, these detectors are described in detail.

1.5 Experimental Setup

In order to overcome the limitations of the E246 experiment, several improvements to the detector system must be undertaken. In this section, I will present an overview of the TREK detector system and several important detectors as follows.

1.5.1 Overview of TREK detector setup

The TREK experiment will be performed using a toroidal spectrometer setup in conjunction with a stopped K^+ beam at the low momentum separated kaon beamline K1.1BR in the Hadron Experimental Hall of the J-PARC 50 GeV synchrotron. The spectrometer consists of an iron-core superconducting toroidal magnet with 12 gaps. The setup is shown in Fig(1.8). The K^+ beam will be stopped in an active target located at the center of the magnet. $K_{\mu 3}$ decays are identified by detecting a π^0 with a CsI(Tl) barrel surrounding the active target, a muon with a charged particle tracking system consisting of GEM chambers (C0, C1), MWPCs(C2, C3 and C4) and the target with particle identification by means of time-of-flight(TOF). This arrangement will enable a measurement of the decay pions ranging over all directions covering all regions of the decay phase space for a given μ^+ momentum. As described next, this scheme allows for a “double ratio” measurement and, thus, a number of systematic errors can be suppressed. The CsI(Tl) barrel has 12 holes to admit charged particles into the magnet gaps. Since the barrel does not cover the full 4π solid angle, not in all events will the two photons from π^0 decay be detected. However, one photon with relatively large energy can also be used to determine the π^0 momentum. Muons are bent by about 90 deg, momentum-analyzed, and then they enter the muon polarimeter system. After passing through a spectrometer and Cu degrader, the muons are finally stopped in the active polarimeter. The muon polarization is measured by means of the decay positron asymmetry. When π^0 s are detected in the forward (FWD) or the backward (BWD) directions relative to the beam axis, transverse component P_T lies in the azimuthal directions in each polarimeter clockwise (*cw*) or counterclockwise (*ccw*), respectively, as shown in Fig(1.9). Thus, the magnitude of the transverse polarization $P_T \sim \vec{\sigma}_\mu \cdot \vec{p}_{\pi^0} \times \vec{p}_{\mu^+}$ can be measured as the azimuthal asymmetry of positron emission, namely, a *cw* and *ccw* emission rate difference.

1.5.2 Fitch-type Cherenkov counter

The Fitch-type Cherenkov counter will also be described in detail in Chapter 6.

1.5.3 Beamline

The K1.1BR beamline for the TREK experiment will be described in detail in Chapter 6.

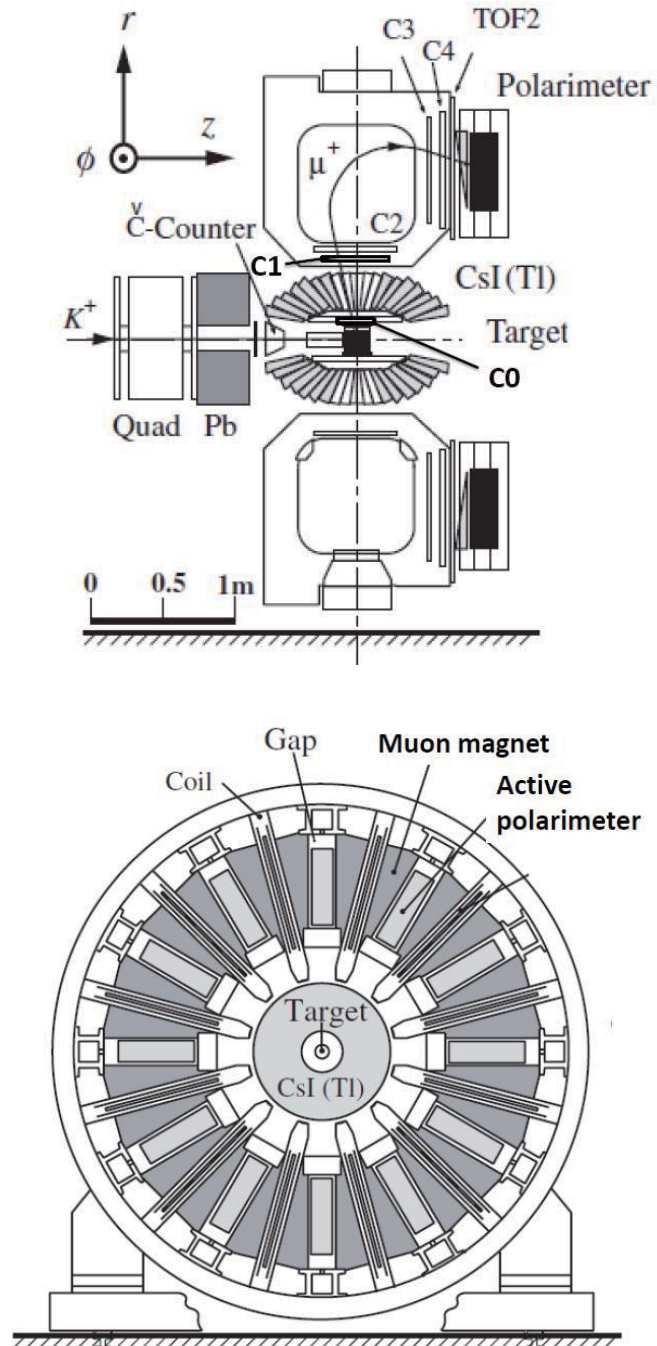


Figure 1.8: Side view (top) and end view (bottom) of TREK detector

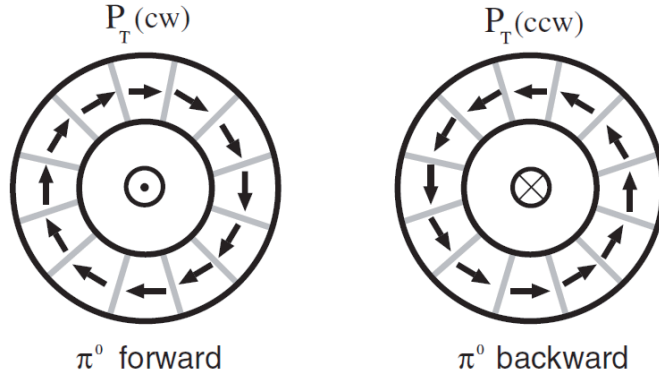


Figure 1.9: T-violating azimuthal polarization P_T for the case of the π^0 going in the forward (fwd) and backward (bwd) directions.

1.5.4 K^+ stopping target

In order to localize the K^+ stopping point (decay vertex) and also to help the tracking of the decay particles, the K^+ stopping target is an active bundle of scintillating fibers. The bundle is made of 489 pieces of 3.0 mm rectangular scintillating fibers with a length of 20 cm forming a 7.5 cm diameter cylinder. In each fiber a thin wavelength shifter (WLS) fiber is embedded in a groove and the light through the nearly 1.5 m long WLS fiber is read by a multi pixel proportional counter(MPPC). The fine segmentation is also necessary to suppress backgrounds in reconstructed trajectories. The manufacturing of the target has been started at TRIUMF in Canada.

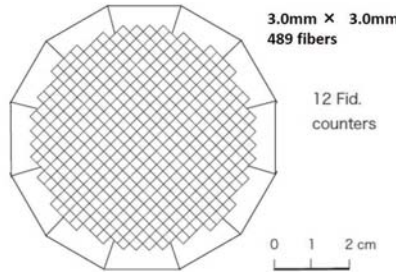


Figure 1.10: Scintillating fiber target for TREK experiment. The active zone has a length of 20 cm and a diameter of 7.5 cm. Each of the 489 fibers has 3.0mm \times 3.0mm square cross section. The fiber bundle is surrounded by 12 fiducial counters.

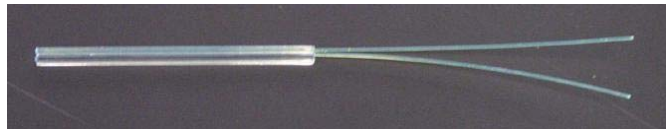


Figure 1.11: Example picture of scintillating fiber with two thin wave length shifter (WLS) fibers although an actual number of WLS is equal to 1.

1.5.5 Photon Counter

The photon counter is one of the most important detectors for the TREK experiment. The muon transverse polarization axis is determined directly whether the π^0 is emitted forward or backward. To reconstruct the π^0 mass and momentum, 768 CsI(Tl) crystals, which have already been used in the E246 experiment, with APD readout, will be adopted. These photon calorimeters make up a barrel surrounding the target region as shown in Fig(1.12). There are twelve muon holes to allow the charged particles to enter the spectrometer. The solid angle coverage is therefore less than 4π ($\sim 3\pi$ if we include the losses due to the K^+ beam entrance and exit holes). The size of the muon hole was optimized to maximize the $K_{\mu 3}$ acceptance. As shown in Fig(1.12), the barrel structure is symmetric for the upstream (forward) and the downstream (backward) side, which is essential in the TREK experiment. The barrel was assembled very carefully ensuring a local as well as a global precision of better than 1 mm. The main parameters of the barrel are summarized in Table(1.1). The calorimeter worked very well in the E246 experiment.

Some valuable features of the photon calorimeter are as follows. First of all, the high light yield of each crystal is confirmed with a low photon energy threshold (≤ 5 MeV). The timing information can be also extracted and this will be available in the analysis. The energy response function has a significant tail on the low energy side mainly due to shower lateral leakage into the muon holes, but the intrinsic energy resolution of the spectrum is reasonably good. In addition, the angular response of a photon was confirmed to be equal to 2.40° using $K_{\pi 2}$ events in the E246 experiment. These angular characteristics become more important in the TREK experiment. The typical responses measured in the E246 data are shown in Fig(1.13). The performance related to energy might be different after modifying the readout scheme, but the angular characteristics will remain almost the same.

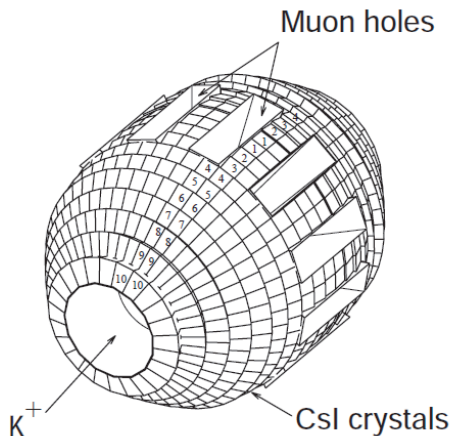


Figure 1.12: CsI(Tl) barrel with 768 crystal modules. There are 12 muon holes.

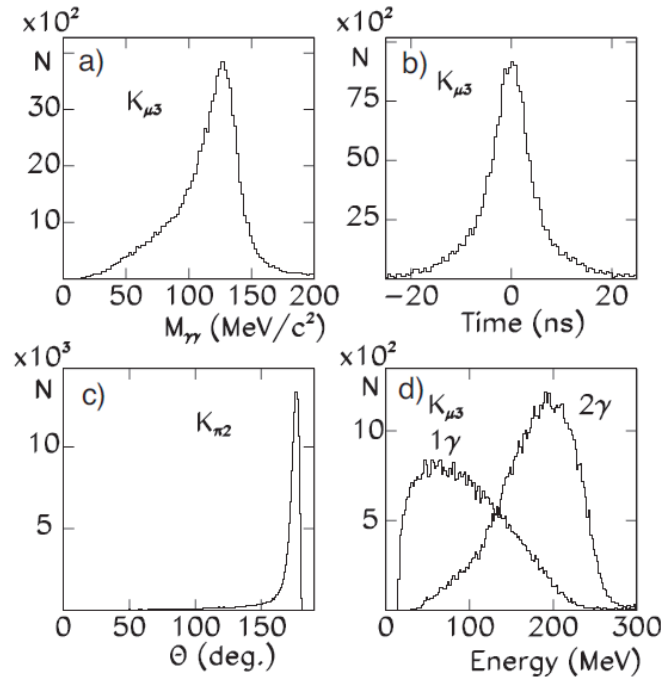


Figure 1.13: Performance of the CsI(Tl) detector for $K_{\mu 3}$ and $K_{\pi 2}$ in E246. a) Invariant mass spectrum of two photons of $K_{\mu 3}$, b) cluster timing distribution also of $K_{\mu 3}$ showing the time resolution, c) opening angle distribution of $K_{\pi 2}$ showing the angular resolution, and d) two-photon and one-photon energy spectra of $K_{\mu 3}$ events.

Table 1.1: Main parameters of the CsI(Tl) calorimeter.

Parameter	Value
Number of CsI(Tl) crystals	768
Segmentation	$\Delta\theta = \Delta\phi = 7.5^\circ$.
Inner / outer diameter	41 / 90 cm diameter
Detector length	141 cm
Solid angle coverage	$\sim 75\%$
Crystal length	25 cm ($13.5 X_0$)
Typical size of crystals	$3 \times 3 - 6 \times 6 \text{ cm}^2$
Wave length at peak	560 nm
Light decay time	$\sim 900 \text{ ns}$

Avalanche photo-diode readout (APD)

In the E246 experiment, the PIN diode readout was used, but it is impossible to take data under the higher counting rate condition expected at J-PARC. Considering the higher intensity of the K1.1BR K^+ beam, it is necessary to use a preamplifier which can be operated under high rate conditions. Thus, we are planning to use avalanche photo-diodes (APD) of reverse type. Such APDs with multiplication factors of about one hundred with reasonably large sensitive areas are commercially available. The conceptual scheme of the APD readout is shown in Fig(1.14), and the relevant parameters are compared with the PIN readout in Table(1.2).

The output from the amplifier system will be read by FADCs (65MHz sampling with 12 bits) recently developed by the KEK electronics shop. The FADCs are very powerful to resolve pulse pileup. If the photon statistics are large enough, one may in principle analyze pileup events up to the rise time of the FADC input pulse, namely the rise time of a photon signal as determined by the light emission mechanism, the shower development in the crystal, and the light propagation/collection in the crystal. If we apply a simple current amplifier, the noise is more serious. This point which might lead to pulse height uncertainty will be solved by the integration (hardware or off-line) of the signal over the time window of 900 ns at the cost of pileup resolving capability. In this case, we may expect the pulse separation of a pileup with a time difference larger than half of the decay time (400 ns) is not spoiled. In a conservative estimation, the calorimeter system can tolerate an average counting rate of 0.1 MHz in each crystal with a loss of 4 %. Since a photon cluster involves $3 \times 3 = 9$ crystals, the maximum rate of 0.1 MHz in each crystal corresponds to a total decay particle rate, of nearly 20 MHz, into the total solid angle of 4π , which is large enough for the beam intensity in the TREK experiment.

To evaluate the performance of the APD read-out and 65 MHz FADCs, we have already performed a beam test at the Research Center for Electron Photon Science, Tohoku University in June 2010.

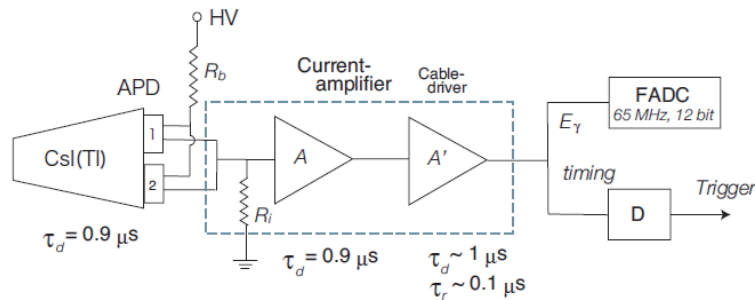


Figure 1.14: Readout scheme of the CsI(Tl) calorimeter using APD

Table 1.2: Readout scheme using APDs compared with the E246 PIN readout.

Parameter	E246-PIN	APD readout
Diode	1 × S3204-03	1 × S8148
Total area	18 × 18 mm ²	5 × 5 mm ²
Quantum efficiency	~ 0.70	> 0.80
Photoelectron / GeV	1.1 × 10 ⁷	4.0 × 10 ⁶
Diode gain	1	50
Electron yield at 100 MeV	1.1 × 10 ⁶	2.0 × 10 ⁷
Preamplifier	Charge sensitive	Current amplifier

1.5.6 Superconducting spectrometer magnet

The superconducting spectrometer magnets will be reused for the TREK experiment. Basically, the performance of the spectrometer expected for the TREK experiment is the same as the E246 experiment. Hence I will describe the status of E246 spectrometer as follows.

The heart of the muon spectrometer is a superconducting toroidal magnet with 12 iron sectors separated by 12 gaps. Each iron sector is magnetized by a superconducting coil, and a field up to 1.8 T can be excited across the 20 cm uniform gaps. At a field strength of 0.9 T, which is used for this experiment, the field is nearly completely dipole with a slight toroidal component superimposed. Charged particles from the target located in the center of the magnet are bent by $\sim 90^\circ$ and tracked by several chambers at the entrance and exit of the gap. One sector of the magnet is illustrated in Fig(1.15). In manufacturing of the magnet, special care was taken to assure the dimensional accuracy necessary for high precision experiments. Each iron core was machined with a precision of 50 μm . The positioning of the superconducting coil relative to the core to form a sector was achieved within an accuracy of 2 mm. Assembly of the entire structure was performed using a special positioning device ensuring a rotational symmetry of 30° . The 12 median planes of the gaps converge to a virtual central axis with an accuracy of 0.3 mm. The difference of the diameters in the horizontal and vertical directions is less than 2 mm over a diameter of about 4.0 m. As a superconducting magnet this device is unique in its structure. The coil windings are NbTi monolith stabilized by Cu operated at about half of the critical current density at 4.5 K and maximum excitation. The windings are cooled indirectly by two-phase He flow through one turn of cooling channels around the windings. The 12 coils are connected in series and equal field distributions are generated in the 12 gaps. A power supply with a stability of 5×10^{-5} is used. Because high-quality magnet steel was used for the cores, there is no significant hysteresis in the magnetization. The validity of the map has been checked using the measured monochromatic momentum spectra of muons from $K_{\mu 2}$ and pions from $K_{\pi 2}$ in the E246 experiment.

1.5.7 Tracking Chamber

E246 tracking system

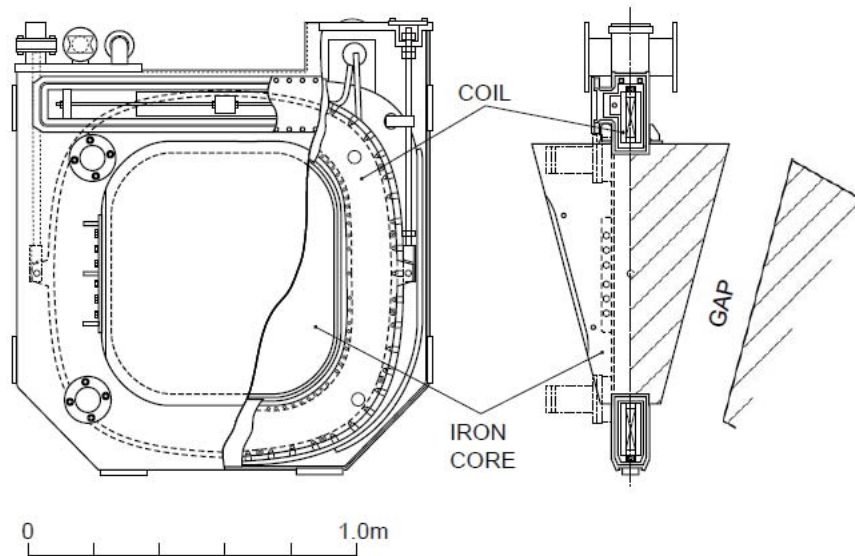


Figure 1.15: One sector of the superconducting toroidal magnet.

In E246, five different tracking elements have been employed, three planar multiwire proportional chambers (MWPC) C2, C3, and C4, a cylindrical drift chamber C1, a scintillating fiber target and ring counters surrounding the target as shown in Fig(1.16). For each of the 12 sectors, positively-charged tracks leaving the target in the transverse direction pass through the gap of the CsI calorimeter and are bent in the toroidal magnetic field by about 90° . The track reconstruction has been based on the three planar chambers C2, C3 and C4 and the ring counters. The C2 element is located at the entrance gap of the magnet, while the C3 and C4 chambers reside near the focal plane at the exit gap of magnet in front of the muon polarimeter. Near the target, another element, C1 drift chamber with cylindrical geometry was installed. However, due to its imperfect high rate performance, the C1 chamber has not been included in the final analysis. Thus, only the ring counter was used for tracking in the source vicinity, but it had a much worse resolution (6 mm) as compared to the other chambers. The momentum of the charged particle was deduced from the reconstructed momentum corrected for the energy loss in the target. The background was rejected in the momentum spectrum as well as in the χ^2 cuts of the track fitting.

TREK tracking system

At J-PARC, two sources of systematic errors will dominate. While one source is given by the background contamination from $K_{\pi 2}$ -dif events¹, the other source of systematics is due to misalignments of the setup, in particular of the muon polarimeter. In the TREK tracking system, the errors from both backgrounds and the alignment will be improved to

¹ $K_{\pi 2}$ -dif is one of the decay mode corresponding to $K^+ \rightarrow \pi^0 \pi^+ \rightarrow \pi^0 \mu^+ \nu_\mu$

Table 1.3: Main parameters of the charged particle tracking

Item	TREK	E246(reference)
High resolution elements	C0, C1, C2, C3 and C4	C2, C3 and C4
Scintillator elements	Target	Target + Rings
C0 chamber	cylindrical GEM chamber	C1 cylindrical chamber
C1 chamber	planar GEM chamber	-
C2 chamber	MWPC (the same)	MWPC
C3 chamber	MWPC (the same)	MWPC
C4 chamber	MWPC (the same)	MWPC
C3-C4 distance	30 cm	15 cm
Magnet gap	He gas bag	air
Total material thickness	$\sim 7 \times 10^{-3} X_0$	$6.6 \times 10^{-3} X_0$

meet the requirement of 10^{-4} for the systematic error in P_T . These performance goals will be achieved both by reducing the material budget along the track and by rearranging the current tracking elements and adding new GEM chambers in replacement of the previous C1 chamber. The momentum uncertainty of 3.6 MeV/c in E246 can be reduced at least by one order,

- 1) by employing a 6 cm instead of 7.5 cm diameter target with a segmentation of 3.0×3.0 mm² fibers instead of 5×5 mm²,
- 2) by replacing the air volume in the magnet between C2 and C3 and before the C2 chambers with helium bags and by increasing the distance between the C3 and C4 elements to 30 cm.

For sufficient identification and suppression of $K_{\pi 2}$ -dif events we need to build a GEM cylindrical tracking chamber (C0) with a radius of 10 cm and a spatial resolution < 0.1 mm. The new C0 chamber will replace the previous cylindrical C1 chamber of the E246 setup. In order to increase the tracking redundancy we will also add a new planar tracking element (again named C1) with < 0.1 mm resolution to cover each of the 12 gaps at the outer surface of the CsI calorimeter. By adding these additional elements to the track fitting procedure, the resulting $\chi^2 / \text{degree of freedom}$ will be much more effective to distinguish tracks from $K_{\pi 2}$ -dif from regular tracks which do not have a kink along their path. In combination with the higher segmentation of the fiber target, this will be sufficient to suppress the $K_{\pi 2}$ -dif / $K_{\mu 3}$ ratio below 10^{-3} , rendering a spurious $P_T < 5 \times 10^{-5}$. Fig(1.16) shows a comparison of the tracking system in the E246 and the TREK experiments. In addition, the tracking elements parameters compared with the E246 are shown in Table(1.3).

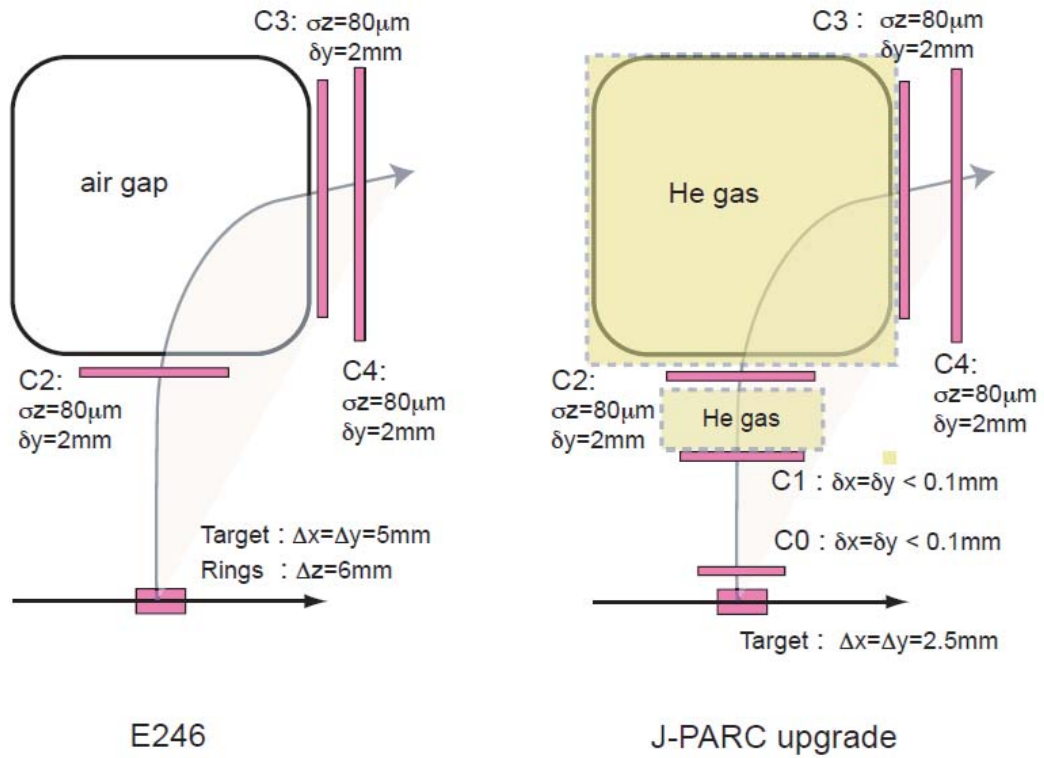


Figure 1.16: Schematics of the tracking system in the E246 setup (left) and the TREK setup (right)

1.5.8 Muon polarimeter

The muon polarimeter for the TREK experiment will be described in detail in the next chapter.

1.5.9 Muon polarimeter magnet

A uniform muon polarimeter magnet with a large strength is essential for the TREK experiment, whereas a passive field was used by guiding and trimming the main field of the superconducting magnet in the E246 experiment. The unavoidable consequence was that there was a non-uniform strength distribution and a curved flux distribution at the stopper. A uniform field parallel to the P_T component provides the maximum analyzing power. Some requirements of the muon polarimeter magnet, size, field strength and uniformity, are as follows.

To accommodate the polarimeter with range stacks on both sides the parallel gap of the dipole magnet must be about 30 cm. The area is determined to produce a uniform field distribution in the polarimeter region. From the point of view of

- 1) spin relaxation suppression,

Parameter	Value
Gap size	70cm(x) × 45cm(z) × 31.4cm(y)
Central field	0.03 T at I = 12 A
Magnetic motive force	3744 A Turn / coil for 0.03 T
Power consumption	530W /coil at 0.03 T
Assembly precision	better than 50 μ A

2) stray field decoupling,

a strong field is preferable. However, the field is limited by the interference with the toroidal magnet, in particular with its SC coils. Point 2) is regarded as the determining factor; assuming 0.3 Gauss of an unwanted component in the shielded magnet gap, a field strength of at least 300 Gauss is necessary to obtain a field alignment of 10^{-3} .

The field symmetry across the median plane is important but a non-uniformity of 10^{-2} in strength as well as in vector distribution is tolerable in the positron energy analysis.

A one sector prototype of the muon polarimeter magnet has been tested in the North Hall of KEK. After the symmetry measurement using the opposite coil-current method of the pole faces and coils without a return yoke, the magnet is now equipped with the low-weight yokes and a return yoke as shown in Fig(1.17), and normal field distribution with normal coil currents were measured. By installing the shim system, a field distribution with a uniformity good enough for the polarimeter was achieved in the fiducial volume. This magnet can be applied to the TREK experiment. It would be, however, necessary to compare the distribution with a 3D TOSCA calculation with the final realistic geometry. An improved shim system which realizes a larger field-flat volume might be possible. We don't know if the perpendicular B_x in the fiducial volume is small enough to suppress the systematic error due to δ_z rotation, although its detailed estimate depends on the actual muon stopping distribution in the polarimeter and this is not yet known.

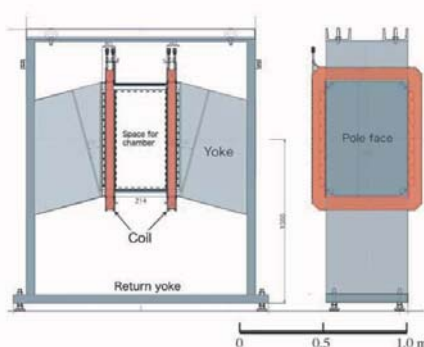


Figure 1.17: Muon field magnet one sector test setup.

1.5.10 Electronics and data acquisition

In order to overcome the higher counting rate at J-PARC, a much faster ADC system has to be used. The data-taking speed will be 100 times faster than E246. Currently we are considering a KEK-VME system, which is being developed at KEK. The KEK-VME is based on the standard VME crate but it is equipped with a power supply for analog modules and digital signal nets for timing and trigger purposes. The readout modules are made of 9U type VME modules and are called COPPER. An ADC module, for example, can acquire data using several kinds of ADC cards (FINESSE) on board with dead times of only several μs . A FADC COPPER with 65 MHz sampling and a 12-bit range has already been developed by the KEK electronics shop and they have already been used for the CsI(Tl) readout test at Tohoku University. This FADC will be used for the CsI(Tl) and muon polarimeter readout in the TREK experiment. A TDC COPPER/AMT-FINESSE with a resolution of 0.78 ns/bin with a delaying dynamic range of 17 bits has also been developed. We are considering the possibility of this module for chambers and counters. In addition, to acquire the data of TOF, which is required for higher time resolution, we have to consider a high resolution TDC. One possibility is a chip with 50 ps resolution and 1.8 ms range, which is now under development. A multi-stop charge-sensitive ADC /ASIC is also being developed.

Chapter 2

Muon Polarimeter for TREK Experiment

2.1 Muon polarimeter

The transverse muon polarization (P_T) in $K_{\mu 3}$ decay is finally measured by the polarimeter. In principle, a decay positron with more than 30 MeV energy from the Michel decay can preserve the muon spin direction due to the helicity conservation. This is a basic mechanism of the polarimeter. Hence, the polarimeter has to measure an emitted direction of the decay positron precisely along with the transverse axis, hence the P_T is measured as a transverse asymmetry of the decay positron (A_T).

It is no exaggeration to say that the most important feature of the TREK experiment is the adoption of an active polarimeter with the ability of measuring a trajectory of particles in contrast to the E246 experiment which used a passive polarimeter. The passive polarimeter consists of a separated system of a muon stopper and positron counters. The advantage of this passive system was the simplicity of the analysis with the consequence of very small systematic errors associated with the analysis. The systematic cancellation scheme, namely the asymmetry is summed over the 12 sectors, is also based on the use of both clockwise and counterclockwise counters at the same time. However, the passive system did not overcome the cost of e^+ detection acceptance and polarization analyzing power. We now aim for higher detector acceptance and higher sensitivity by introducing an active polarimeter. The suppression of the systematic errors ensured in the E246 passive polarimeter will be guaranteed by a different method.

2.2 Passive polarimeter for the E246

A passive polarimeter as shown in Fig(2.1) was used for measuring P_T in the E246 experiment. The E246 analysis method will be able to give us some hints about how to improve and build the new polarimeter.

Structure of the E246 polarimeter

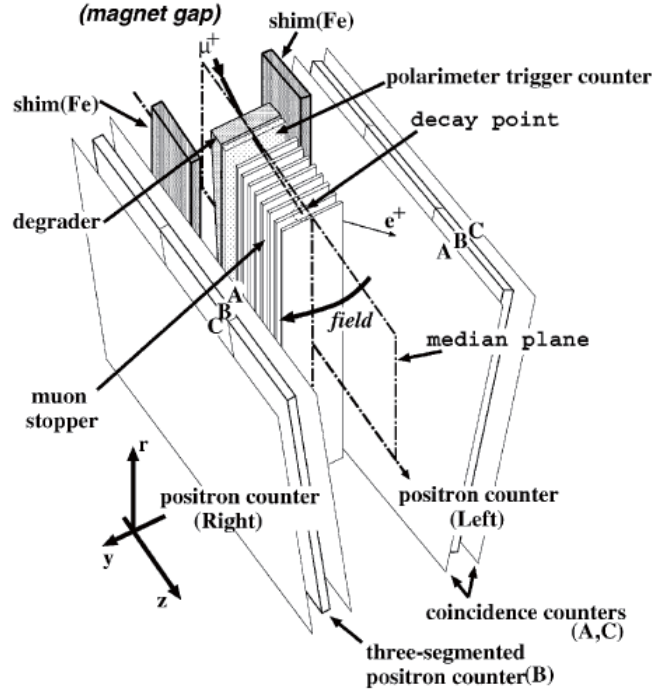


Figure 2.1: Schematic structure of the muon polarimeter.

One sector of this polarimeter consisted of the following components,

- 1) a wedge shaped Cu degrader for decreasing the speed of muons,
- 2) Fe shims for adjusting the magnetic field from the toroidal spectrometer,
- 3) one polarimeter trigger counter,
- 4) 8 pure Al plates of 6 mm thickness with size of 16 cm width and 55 cm height with 8 mm spacing in between for stopping muons,
- 5) two sets of counters for detecting positrons,
- 6) veto-counter.

The width of the pure Al plates are smaller than the toroidal spectrometer gap of 20 cm and polarimeter trigger counter width of 18 cm so that all the stopped muons would generate a trigger. The height was chosen to cover the necessary momentum range and the total Al thickness of 48 mm was enough to stop muons in a wide momentum range with an efficiency of more than 85 %. The spacing lowered the effective average density of

Al to suppress the e^+ interaction creating nearly optimum conditions for the asymmetry measurement. Veto-counters behind the stopper detected nonstopped muons to suppress background decays from the surroundings.

The holding field strength applied by two iron shim plates aside the stopper varied from 300 to 150 G with a vector direction as shown in Fig(2.2).

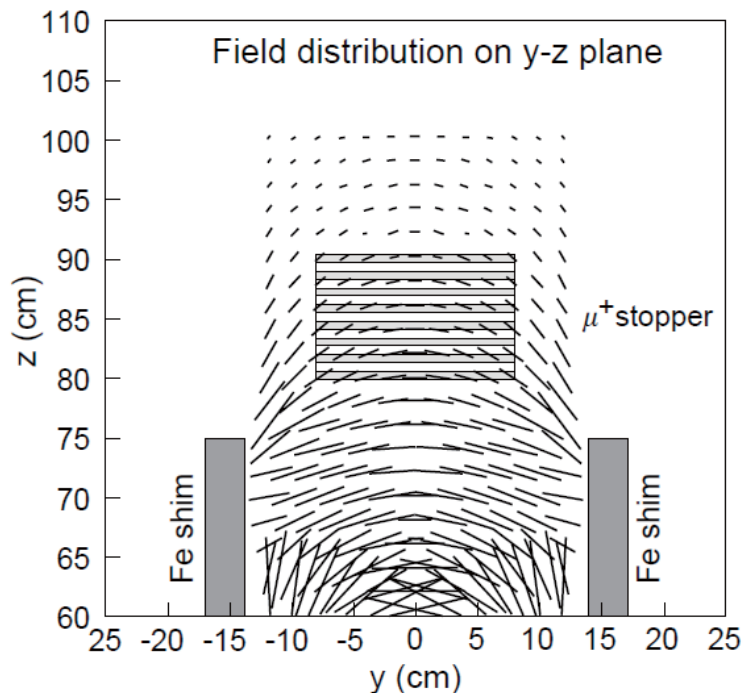


Figure 2.2: Magnetic field distribution on the muon stopper

The shim plates were aligned with a precision better than $200 \mu\text{m}$ relative to the magnet gap in order to produce a symmetric field distribution across the median plane. A field mapping was performed to check the field symmetry and to measure the strength distribution for all 12 gaps. The field vector could be analyzed with a precision of 1 mr.

Positrons were counted by a plastic counter (e^+ counter) of 6 mm thickness segmented in three parts in coincidence with two sandwich coincidence counters of 3 mm thickness. The counter system was aligned with a precision of a few mm relative to cw as well as ccw stoppers. One positron counter system served as both the cw and ccw counter with the same detection efficiency. The solid angle of detection (about 10 % on each side) was determined by the three e^+ counters and the detection threshold was set at 5 MeV. The positron time spectra were measured with a multistop time-to-digital converter (TDC) with a time range of $20 \mu\text{s}$ relative to the time origin.

The analysis method of the E246 polarimeter

The transverse polarization was measured as an asymmetry defined as

$$A = \frac{N_{cw} - N_{ccw}}{N_{cw} + N_{ccw}} \quad (2.1)$$

with the clockwise (*cw*) and counterclockwise (*ccw*) counts N_{cw} and N_{ccw} , respectively. A measurement to determine the null asymmetry A_0 , was also needed to ensure an accurate P_T . For measuring the null asymmetry, the data, which did not require the π^0 direction (*fwd* direction or *bwd* direction), could be used. In this case, most of the data could include $K_{\pi 2}$ events. After confirming the data quality from the null asymmetry measurement, the transverse polarization (P_T) measurement could be performed. In order to take better quality P_T data from $K_{\mu 3}$ decay, a double ratio method was performed for two opposite kinematic situations which correspond to the π^0 direction, respectively (*fwd/bwd*). Paying attention to just one e^+ counter, it could count both N_{cw} and N_{ccw} . This means that the efficiency of this counter is canceled out when we sum up the 12 sectors data with 12-fold azimuthal symmetry. This method played an important role in reducing the systematic errors. However, several difficulties still remained. When the transverse asymmetry was

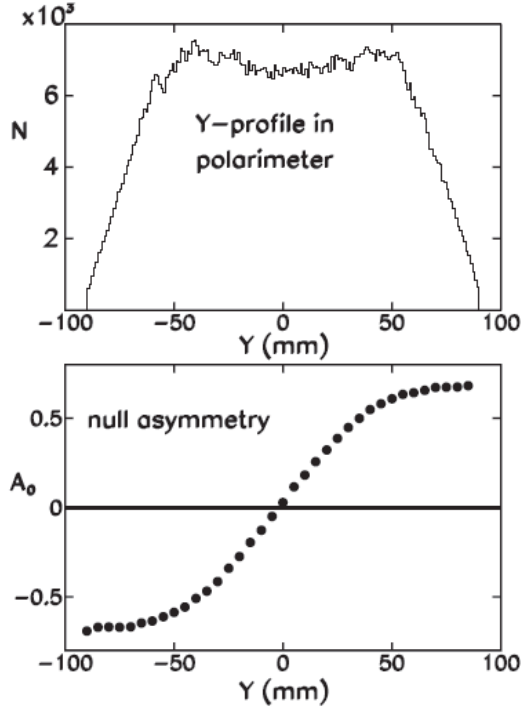


Figure 2.3: Incident muon y distribution in the stopper measured by the C4 chamber (top), and the intrinsic geometrical asymmetry for those muons (bottom). The real stopping distribution has a smearing due to beam divergence and multiple scattering. The geometrical asymmetry was measured as the null asymmetry A_0 by accepting all π^0 directions.

measured, it was essential to consider the fact that the muon stop distribution could affect

the asymmetry very strongly. In particular, a shift along the y direction was critical. The asymmetry $A_0(y)$ for the muons is shown in Fig(2.3). The effect of the shift on the asymmetry is $\delta A = k \times \delta \langle y \rangle$ with $k = 0.015/\text{mm}$ for the average shift $\delta \langle y \rangle$. Considering such a spurious effect, the asymmetry was analyzed differentially using the y -information from the C4 chamber which is in front of the polarimeter. The y dependence of the T-violating asymmetry $A_T(y)$ was calculated as

$$A_T(y) = \frac{1}{2}(A^{fwd}(y) - A^{bwd}(y)), \quad (2.2)$$

with the y -dependent fwd and bwd asymmetries

$$\begin{aligned} A^{fwd}(y) &= \frac{1}{2} \left[\frac{N_{cw}^{fwd}}{N_{ccw}^{fwd}} - 1 \right], \\ A^{bwd}(y) &= \frac{1}{2} \left[\frac{N_{cw}^{bwd}}{N_{ccw}^{bwd}} - 1 \right]. \end{aligned} \quad (2.3)$$

Here, $N_{cw}(y)$ and $N_{ccw}(y)$ are the event number distributions from C4- y . The T-violating polarization at y is then extracted using the relevant analyzing power function of $\alpha(y)$, which is determined by the polarimeter structure, especially detector acceptance, as

$$P_T(y) = \frac{A_T(y)}{\alpha(y) \langle \cos \theta_T \rangle}. \quad (2.4)$$

The attenuation factor, $\langle \cos \theta_T \rangle$ determined by the average of the angles $\cos \theta_{\pi^0}$ is independent of y . This scheme corresponds to the case in which a number of sliced muon stoppers were inserted and the polarization measurements were done for each stopper. The final P_T result for one data set was obtained as the statistical average of $P_T(y)$ as

$$\begin{aligned} P_T &\equiv \langle P_T \rangle = \int P_T(y) w(y) dy, \\ &= -0.0017 \pm 0.0023(stat) \pm 0.0011(syst), \end{aligned} \quad (2.5)$$

with the normalized weight function of $w(y) \sim 1/\sigma^2_{P_T}(y)$. Thus, P_T was unaffected by the muon stopping distribution in the stopper.

As mentioned above, it was impossible to avoid the effect of multiple scattering and there is no way to know the decayed vertex. This means that some systematical uncertainties are still remaining. Actually, the uncertainty of muon multiple scattering is larger than any other systematic error as shown in Table(2.1). Considering these points, the E246 polarimeter should be improved in order to achieve the sensitivity of $\delta P_T \sim 10^{-4}$.

Table 2.1: Summary of major systematic errors

Source	Σ_{12}	fwd/bwd	$\delta P_T \times 10^4$
e^+ counter r-rotation	yes	yes	0.5
e^+ counter z-rotation	yes	yes	0.2
e^+ counter ϕ -offset	no	yes	2.8
e^+ counter r-offset	yes	yes	< 0.1
e^+ counter z-offset	yes	yes	< 0.1
\vec{B} offset (ϵ)	no	yes	3.0
\vec{B} rotation (δ_r)	no	yes	0.37
\vec{B} rotation (δ_z)	no	yes	5.3
μ^+ counter y -offset	no	yes	< 0.1
CsI(Tl) misalignment	yes	yes	1.6
K^+ stop distribution	yes	yes	< 3.0
MWPC y -offset (C4)	no	yes	2.0
K^+ DIF background	yes	no	< 1.9
$K_{\pi 2}$ DIF background	no	yes	0.6
μ^+ multiple scattering	yes	no	7.1
e^+ time spectrum	no	yes	0.8
Decay-plane angle (θ_r)	no	yes	1.2
Decay-plane angle (θ_z)	no	no	0.66
Uncertainty of α	-	-	1.3
$\langle \cos\theta_T \rangle$ uncertainty	-	-	3.3
P_T gradient	-	-	0.3
Analysis	-	-	0.9
total			11.4

2.3 Requirements for an active polarimeter

The active polarimeter should have the following functions and advantages.

- **Determination of the muon vertices event-by-event**

An active polarimeter determines the muon stopping position for each event. Therefore the TREK experiment will be free from the systematic error associated with the ambiguities in the muon stopping distribution. Since the decay positron tracks, in addition to muon tracks, are measured, the decay vertices will be determined event-by-event. In contrast to the situation in the E246 experiment, where the positron signals were associated with non-negligible constant background events, the active polarimeter data will be relatively background free.

- **Higher solid angle acceptance as possible**

The detection of decay positrons in all directions by a polarimeter with nearly 4π solid angle will provide a much larger acceptance. In the E246 experiment, the positron counter solid angle was limited to about 10% on each side. The active detector acceptance becomes roughly 10 times larger, even though the sensitivity does not scale by this factor. The ability to measure the positron emission provides the possibility to use not only the *fwd/bwd* π^0 scheme but also the *left/right* pion scheme which was not possible in the E246 experiment.

- **Measurement of the positron emission angle**

The asymmetry changes as the function of both the positron emission angle and the energy. A weighted analysis brings about a significant increase in the analyzing power resulting in higher sensitivity. It is of interest to note that this superior performance is achieved in case of measuring the positron emission angle precisely.

2.4 Concepts of the polarimeter design

The requirements for the polarimeter design are following below.

- The polarimeter should have a large muon stopping efficiency in relatively small volume. This means that the polarimeter should be made of a material with high average density.
- On the contrary, the polarimeter enable clean detection of positrons without interactions such as bremsstrahlung or annihilation in flight. This means that the polarimeter should be made of a material with low average density.

- A drift chamber makes sense as a detector.
- The cell structure is essentially determined by the fine structure of the stopper. Thus, the stopper has to be designed taking this point into account.
- Optimization for the azimuthal field arrangement sets the highest priority to the *fwd/bwd* pion analysis. Thus, the stopper structure must be optimized for the *cw/ccw* asymmetry measurement.
- Internal cancellation mechanism against any local inefficiency is essential for the polarimeter. The *cw/ccw* inefficiency cancellation scheme of the E246 experiment is maintained by using the polarimeter.

Considering these conditions, a parallel plate configuration has been proposed as shown in Fig(2.4). The parameters of this polarimeter are also shown in Table(2.2). The tube polarimeter is actually in progress and it will be described in Chapter 5. Considering the stopping power and the spin relaxation, we also should have determined the inner material to be either Al or Mg.

Table 2.2: Parameters of plate and wire

Number of plates	24
Material	Al
Size of plate	700 mm \times 300 mm
Plate thickness	2.5 mm
Plate gap	8 mm
Average density	$0.24\rho_{Al}$
Stopping efficiency	nearly 85 %
Number of anode wires	nearly 500
Anode wire	SUS304 / $20\mu\text{m } \phi$
Anode wire gap	16 mm
Number of cathode wires	nearly 500
Cathode wire	Au-CuBe / $100\mu\text{m } \phi$
Cathode wire gap	16 mm

2.5 Requirement for stopper material

One of the most important issues in designing the active polarimeter is the selection of the stopper material. The analyzing power, defined as A_T/P_T , should be as large as possible to obtain the highest sensitivity in the experiment. This analyzing power is also required to be independent of environmental conditions such as the ambient temperature, to be

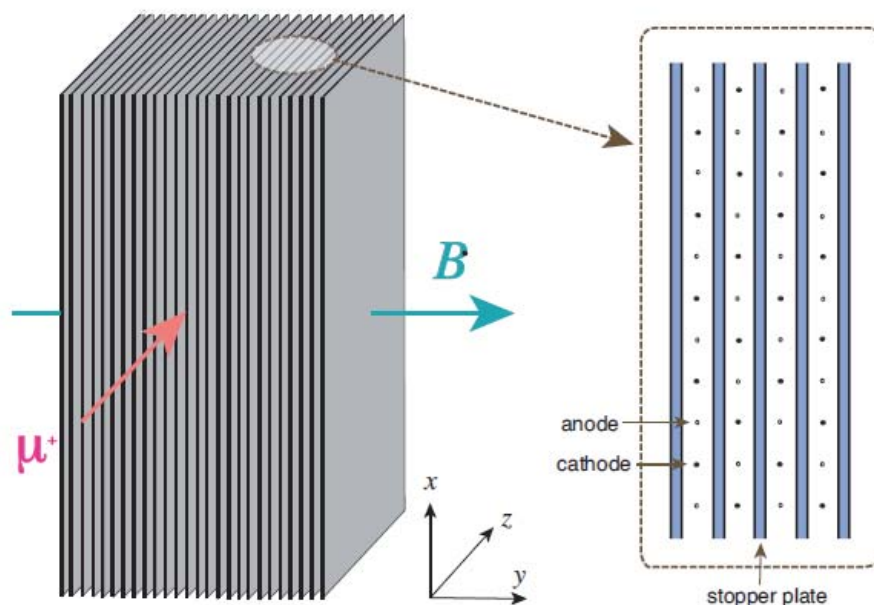


Figure 2.4: Muon stopper made of parallel plates which serve also as drift chamber cell structure.

stable during a long-term measurement, and to be uniform over the whole volume of the 12 stopper units. These requirements mean that the polarimeter should not lose the initial polarization of the incident muons due to some interactions in the stopper material during the muon stopping phase, and that the spin polarization relaxation due to solid state physics effects, if any, should be small. Hence, the stopper material should be selected

- 1) without any initial polarization loss during stopping and
- 2) without any significant spin relaxation.

Considering the decay positron interactions, the material should also be a light element. It is known that pure metals such as Al satisfy these conditions at room temperature. In fact for the E246 experiment, a pure Al plate with 99.99 % purity was adopted. In the TREK experiment, however, pure Al is not suitable, because the muon stopper material itself constitutes a component of the active polarimeter drift chamber mechanical structure. Therefore, the stopper plates have to be rigid enough as a structural element and to have a large yield strength. Pure Al, when it is annealed for the highest diffusion characteristics of muons, is too soft and easily deformed. Thus, the best material should be looked for in a wider range of metals and alloys. The most important prerequisite is the good spin polarization behavior which could be investigated with a real muon spin relaxation measurement.

Hence, an experiment was performed at TRIUMF using a surface muon beam at M20 in May 2007 under realistic magnetic field conditions. [47] In this study, only pure Al and

Mg and their alloys were studied. For the muon spin relaxation (μ SR) experiment, some samples were collected as shown in Table(2.3). The criteria for the selection was that the concentration of the admixed elements should not be large, in particular, magnetic impurities like Fe, Mn or Cr. For these impurities the depolarization can be significant due to the large paramagnetic fields from these elements if the muons are trapped in the sites. Although the transverse field as well as the longitudinal field measurement were performed with an external magnetic field of 0.03 T, which is the same field strength as designed parameter for active polarimeter, the longitudinal field relaxation rate is relevant if we do the analysis primarily in the *fwd/bwd* scheme.

In conclusion, any alloys of Al and Mg could be used except for the Al alloy A2017 and the Mg alloy AZ31-PE which showed a relatively large relaxation rate in a transverse field and a longitudinal field, respectively. Finally, A5052 was selected as the frame material of the polarimeter and pure Al (JIS1100) was also selected as the stopper. The final selection was done by comparing the characteristics of the surface condition which is important for the drift chamber electrode.

2.6 Expected performance of the polarimeter

An active polarimeter should have the abilities to measure both the muon and decay positron tracks with high position resolution, typically $100\mu\text{m}$. The coordinate along the wire is determined by charge division at both ends. The coordinates in the y - z plane are determined by drift time information. The angular determination of decay positron track is done after determination of 3-dimensional position.

Considering Michel decay and helicity conservation, selecting high energy (more than 35 MeV) positrons make sense since the low energy (less than 30 MeV) positrons have a negative asymmetry A_T . Thus, we should determine the threshold level for positrons using stoppers to achieve a higher sensitivity of P_T . Since we will know the number of plates that the positron passes through, we can select just high energy positrons.

In order to determine the cell structure including plate thickness precisely, we have calculated electric field distribution of a cell using a Garfield simulation. Although the cell structure is a rectangle, the drift velocity, which is mostly determined by the kinds of gas, is a linear function without a neighboring anode wire. The performance will be described as a drift chamber in detail in Chapter 4.

Table 2.3: List of μ SR target

Material	Base	Si	Cu	Fe	Mn	Ni	Zn	Zr	Al	Mg	Ti	t[mm]
AZ31B	Mg	0.021	0.0011	0.0015	0.4		0.85		2.91			1.0
Pure Mg	Mg	0.01	0.0016	0.0046	0.0098				0.0064			1.0
AZ31-PE	Mg	0.011	0.0007	0.006	0.0034	0.0007	0.93		2.80			1.0
AZ61A	Mg	0.015	0.0029	0.002	0.35	0.0012	0.74		6.40			1.0
AZ91D	Mg	0.031	0.002	0.002	0.23	<0.001	0.69		9.22			1.0
AM60B	Mg	0.008	0.0013	0.005	0.32	0.0008			5.88			1.0
ZK60A	Mg						5.60	0.52				1.0
Mg-6%Zn	Mg	<0.001	<0.005	<0.005			6.2		<0.001	Bi<0.005	Pb<0.005	1.0
A5052	Al	0.10	0.02	0.27			0.01			2.5	others<0.15	1.0
Pure Al	Al								>99.99			2.0
Al1050	Al	0.1	0.02	0.29	0.00		0.00		99.55	0.01	0.01	1.0
A6063	Al	0.44	0.00	0.18	0.00		0.00			0.51	0.00	2.0
A2017	Al	0.66	0.49	3.8	0.47		0.02	<0.01		0.5	0.01	1.0
p. Al annealed	Al								99.999			3.0

2.7 Development of the charge division method

2.7.1 Test experiment

The position resolution along the wire direction is required to be better than 2 mm in σ . In order to check the performance of the position determination by charge division, a 1/5 prototype chamber as shown in Fig(2.5) was constructed.



Figure 2.5: Picture of 1/5 prototype polarimeter

The test experiment was performed at the Fuji Test Beam Line (FTBL) at KEK in Nov 2008. The detail of this experiment is described in Ref [48]. The e^- beam with an average energy of 2 GeV hits the vertical center position of the prototype chamber. ADC and TDC data were recorded by moving the chamber along the wire axis. The data, which is equal to $x = \pm 15$ cm and ± 5 cm from the center of the wire, was mainly taken for the analysis.

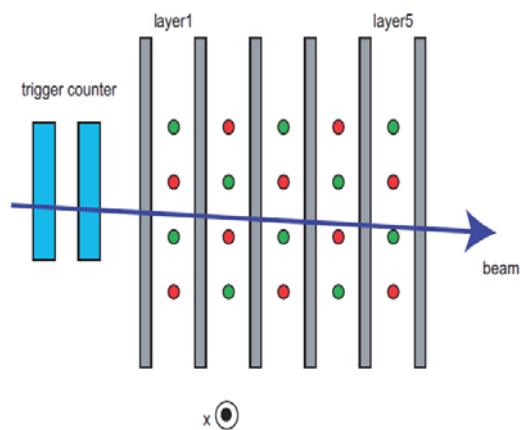


Figure 2.6: Picture of 1/5 prototype polarimeter

2.7.2 Analysis scheme

In the method of charge division which will be described in detail in Appendix A , the distance of the particle hit position from the center of the wire is finally defined as x ,

$$\frac{x}{Z} = \left(1 + \frac{r_1 + r_2}{R}\right) \frac{Q_2 - Q_1}{2Q} - \frac{r_1 - r_2}{2R}, \quad (2.6)$$

where Z is the total length of the wire and R is the total resistance of the wire. In addition, the input impedance of the amplifier and the corrected charge on a capacitor are defined as r and Q , respectively. In this analysis, the value of $r_1 - r_2$ is assumed to be much smaller than R and is negligible. As easily understood, the wire length can be regarded to be extended due to the input impedance of amplifiers. In other words, the resolution of x becomes a factor of $1 + (r_1 + r_2)/R$ worse than that of $(Q_2 - Q_1)/2Q$. It is necessary to correct the amplifier gains and the input impedance of the amplifier because only the values of Q_1 and Q_2 can be extracted from the measurement. The gain correction is performed by introducing a gain ratio parameter α as,

$$RQ = \frac{Q_2 - Q_1}{2Q} = \frac{1}{2} - \frac{Q_1}{Q_1 + Q_2} = \frac{1}{2} - \frac{1}{1 + Q_1/Q_2} = \frac{1}{2} - \frac{1}{1 + \alpha Q_1'/Q_2'}, \quad (2.7)$$

where Q_1' and Q_2' are the output charges from the amplifiers. Since α can change run-by-run due to the fluctuation of input impedance, in this analysis we obtained the α values by requiring the fact that the mean values of the RQ distributions were balanced for symmetric positional data such as 5 cm / -5 cm. Actually, the value of α is not far from 1.

Next in order to determine x from the RQ distribution, we need to correct for the effect of the input impedance as,

$$\begin{aligned} \frac{x}{Z} &= \left(1 + \frac{r_1 + r_2}{R}\right) \cdot RQ = f \cdot RQ, \\ x &= Z \cdot f \cdot RQ = 65\text{cm} \cdot f \cdot RQ. \end{aligned} \quad (2.8)$$

Since the mean value of the beam profile of each run is known, the x distributions are obtained to satisfy these mean values by adjusting the f parameter.

2.7.3 Result and an additional analysis

The RQ distribution and x distributions are shown in Fig(2.7). And the resulting residual distribution which just corresponds to the position resolution is also shown in Fig(2.7).

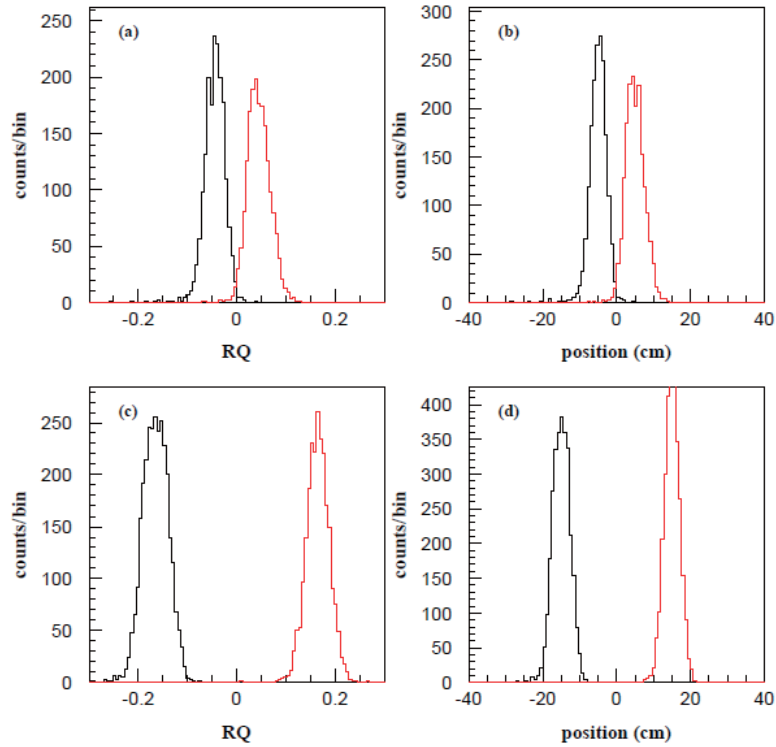


Figure 2.7: (a) and (c) are RQ distributions and (b) and (d) are x distributions, respectively. (a) and (b) are ± 5 cm samples and (c) and (d) are ± 15 cm samples. The RQ distributions are obtained by adjusting the α . The x distributions are also obtained by adjusting the f parameter.

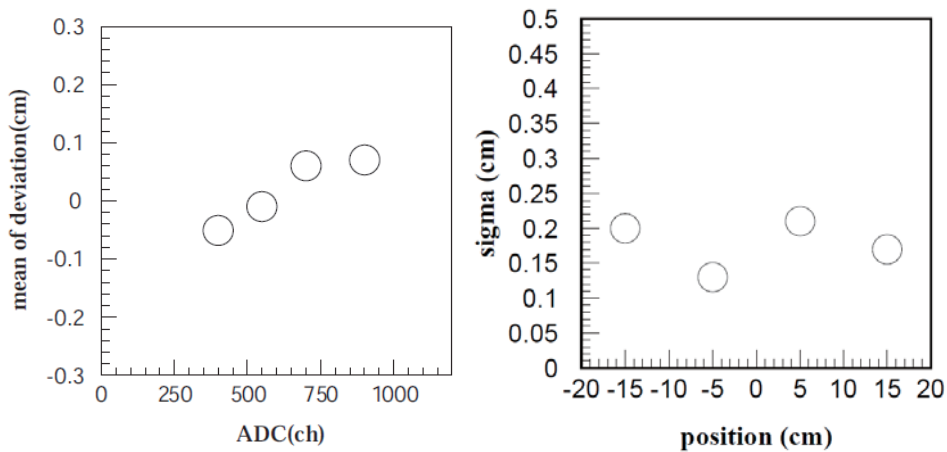


Figure 2.8: The residual distribution before correction (left) and the residual distribution after applying the additional correction (right) as discussed in the text.

Here, an additional correction to improve the position resolution is introduced. As shown in the left figure of Fig(2.8), a slight shift of the residual distribution can be recognized, and the systematic effect of the amplifier response as a function of pulse height of the input signal has to be considered. To correct this effect, it is necessary to separate the ADC regions into 4 regions as 1) $Q_h < 500$ ch, 2) $500 < Q_h < 600$ ch, 3) $600 < Q_h < 800$ ch, and 4) $Q_h > 800$ ch. The f parameters were finely tuned to remove the above correlation with fixed α . The residual distribution after this correction are also shown in the right figure of Fig(2.8).

2.7.4 Summary

In conclusion it can be interpreted that the input impedance of the amplifier changes as a function of the ADC value, and this effect can be corrected by adjusting the f parameters. As the result of the test experiment, the position resolution of 1/5 prototype chamber was obtained to be 2 mm in σ which is good enough for our requirement. Indeed we have tested two kinds of sense wires both SUS304, which has 1.9 K Ω intrinsic resistance and Stablohm800, which has 2.54 K Ω intrinsic resistance. SUS304 has been finally adopted as the sense wire in the TREK experiment.

2.8 Production

After the development of the charge division method, a Full Size Model polarimeter (FSM) has been made by REPIC Co. During the manufacturing, I went there and checked the progress of the work. As mentioned in section 2.4, pure Al plates were adopted as the stoppers and A5052 materials were adopted as the frames of the polarimeter. SUS304 wires with the diameter of 20 μm , which have a large resistance, were adopted as the sense wire and Au-CuBe wires were also adopted as potential wires. Both the potential wires and the stopper plates work as the cathode. Stringing the wires took more than 3 days due to the large number (nearly 1000) of wires but also due to their fine structure.

All the sense wires were strung with the same 30 g tension using a weight and the potential wires were strung with a tension of 80 g. Since the accuracy of the wire position was determined by the accuracy of the attached feedthrough, these feedthroughs were also attached very carefully. After the process of stringing the wires, the wire tensions were tested by using a magnet. First of all, some AC electric currents are input into a drive wire and its frequency is increased. As the drive wire produces a resonance on its specific frequency, an oscillatory wave is transmitted to the other wires. As each wire reaches its specific frequency, external force (here, the magnetic field's) also produces resonance. Finally the current is converted into tension. We are able to measure the tension this way if the wires have the same specific frequency. After the tension measurement, the process of assembling was started. The final overview of the FSM is as shown in Fig(2.10).

After assembling, a high voltage test was done with maximum voltage. (nearly 2000 V)

Although some capacitors had some electric leakage on the printed circuit board (PCB) at first, we finally succeeded in the normal operation as a drift chamber. It took more than 2 weeks to achieve the normal chamber operation.

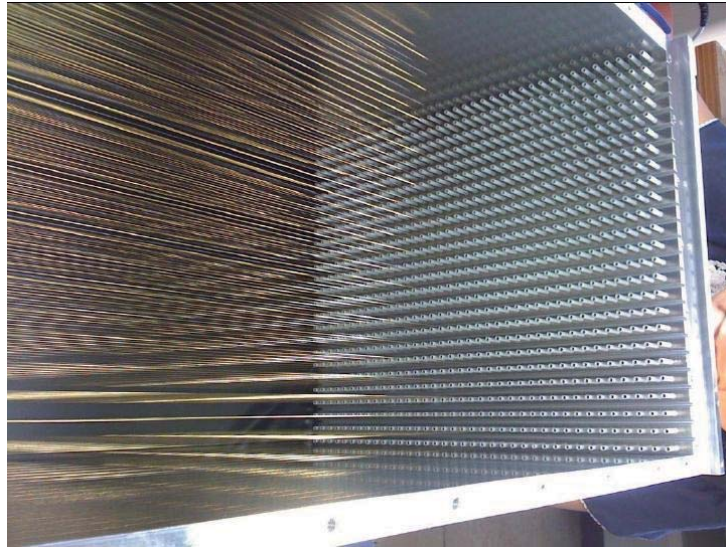


Figure 2.9: Process of the wire stringing.



Figure 2.10: Picture of the FSM polarimeter.

2.9 Read-out system for the polarimeter

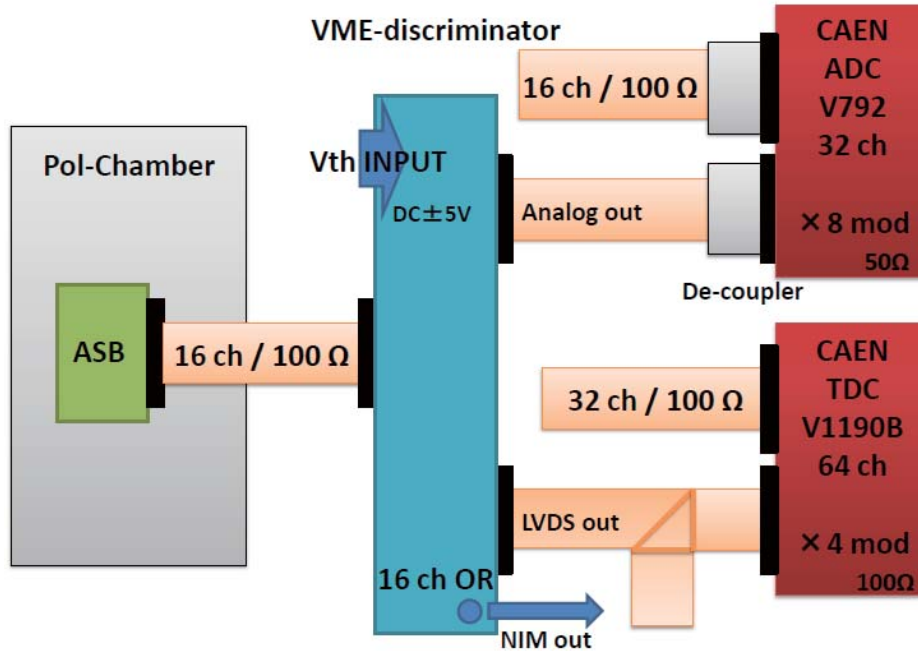


Figure 2.11: Main flow of the data acquisition system.

A polarimeter read-out test was performed at the same time as the polarimeter performance test at TRIUMF in Nov 2009. A schematic view of the read-out is shown in Fig(2.11).

The main data acquisition stream follows below. First of all, the chamber raw signals input into an ASB card. The ASB card serves as amplifier(A), shaper(S), buffer(B). The ASB output signal passes through a flat cable and input VME-discriminator board which requires about ± 5 V for its operation. The VME-discriminator board just works as an ordinary discriminator. But it has also three kinds of output which are an analog, a LVDS and a NIM signal, respectively. The analog signal and the LVDS signal are required for the CAEN ADC and TDC modules. On the other hand, the NIM signal is used in order to tag the chamber signals. In fact, the trigger logic includes the NIM output signals. After the VME-discriminator board, the LVDS signals finally input into the CAEN TDC modules. The TDC modules are used to take both chamber data and all counters' data. In terms of impedance matching for the ADC modules, the De-coupler cards are also required for our measurement. The De-coupler cards are connected directly to the CAEN ADC modules for the adoption of charge division method. The several important parts of the data acquisition system are summarized below.

2.9.1 16 ch Amp. Shaper Buffer card (ASB card)

This ASB card as shown in Fig(2.12) will be used as one of the read-out parts for the polarimeter data acquisition. ASB IC (JRK-ASB(N)-1) chips were developed by KEK

electronics shop and REPIC Co. Since we require to measure an analog output signal due to the adoption of the charge division method, we cannot use the standard Amp. Shaper Discriminator (ASD) card. Basically, an analog input signal from an anode wire is integrated for all 16 channels on one board with 25 ns time constant. In addition, the output signals pulse height can be changed due to gain controller as shown in Table(2.5). The ASB has a small input impedance, thus, it is possible to adopt the charge division method. The main functions are summarized in Table(2.4).

Table 2.4: The main functions of ASB

ASB IC	JRK-ASB(N)-001 \times 4 pcs
Analog input	negative charge input / 16 ch input
Maximum quantity of charge	1.5 pC with minimum gain
Shaping time constant	about 25 ns
Test input	negative NIM 50 Ω impedance
PP control	nor suppress input impedance
Analog output	- 3.75 V \sim - 1.25 V
Vth control	\leq + 2.5 V
Digital output	ECL output
Consumption of electricity	+ 5 V 500 mA / - 5 V 300 mA

Table 2.5: Gain control set

GC1 = L	GC1 = Open	GC1 = L	GC1 = Open
GC2 = L	GC2 = L	GC2 = Open	GC2 = Open
- 360 mV/pC	- 490 mV/pC	- 750 mV/pC	- 1400 mV/pC

2.9.2 VME discriminator board MODEL RPV-240

The VME discriminator boards have two kinds of output - analog and LVDS signals. The analog signals are used for the ADC data and the LVDS signals are used for the TDC data. Although the discriminator modules have a function for adjusting the threshold level, it is necessary for this module to provide 5 V from another DC power supply. In addition, this module has a test output. The test output signal, which is a NIM signal, is generated as an OR output even if only one channel of the 16 channels has a hit. The main specs are summarized in Table(2.6).



Figure 2.12: Top view of ASB cards.

Table 2.6: The specs of VME discriminator board

INPUT	16 CH Analog INPUT
Vth INPUT	Maximum INPUT 5 V
Analog OUTPUT	16 CH Analog OUTPUT
Digital OUTPUT	16 CH Digital OUTPUT (LVDS 110 Ω)
OR OUTPUT	16 CH OR OUTPUT (Negative NIM 50 Ω impedance)
POWER SUPPLY	+ 5 V / 1.1 A

2.9.3 De-coupler card

First, the De-coupler card works as an attenuator. Although VME discriminator board output signals are more than 1 V, the De-coupler cards output signals have 3 times lower pulse height than the input signals so as to take ADC data. Actually, the quantity of the integrated charge is limited to the CAEN ADC's dynamic range. In order to achieve a higher position resolution along the wire direction, it is necessary to gain a lot of charges before the pulse shaping by the ASB card. At the same time, the quantity of charge has to be reduced to be able to take ADC data. In addition, the De-coupler card also works as a 200 ns delay module. As the trigger timing is always delayed by more than 100 ns as compared to the time reference, delaying the analog signals is also necessary for ADC data taking. As mentioned above, the De-coupler card plays an important role for the analog signals.

2.9.4 CAEN ADC V792 / CAEN TDC V1190

The CAEN ADC V792 and CAEN TDC V1190 modules were utilized for the data acquisition. One ADC module has 32 channels and provides data for the charge division method. In addition one TDC module has 64 channels and provides data for making both the muon and the positron tracks. Since it is possible for a wire to be hit two times on one event, a multi-hit TDC module is required so that one channel can take more than 2 data hits for each event. This means that both the muon and the positron can pass near the same wire. This requirement is met by using the CAEN TDC V1190. Although the TDC is multi-hit, the ADC is not. Thus, we could take just the positron ADC data which was essential to measure the position along the wire using the charge division method. Instead a FADC will be used for the polarimeter data acquisition in the TREK experiment, so it will be possible to collect both ADC and TDC data for both the muon and the positron.

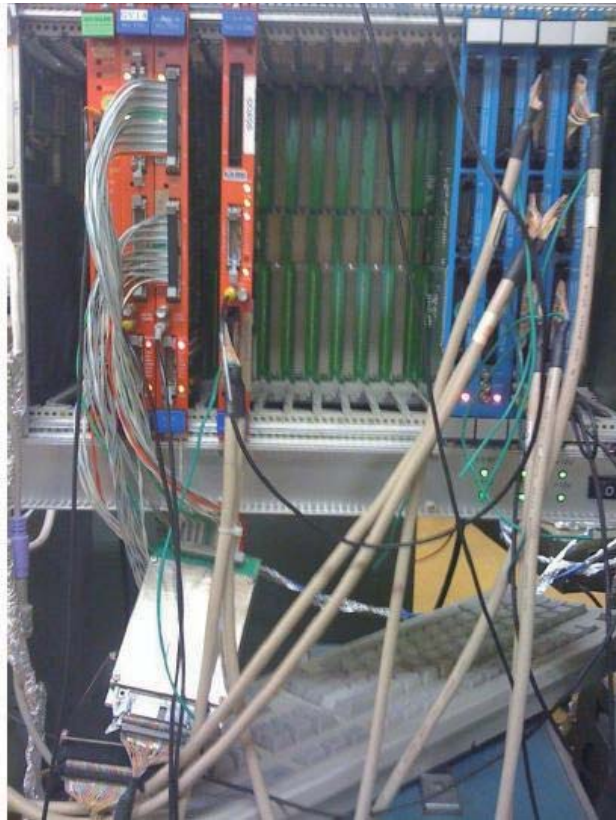


Figure 2.13: Overview of the modules for DAQ. The silver card on the bottom is one of the De-coupler cards. The four red modules are the interrupt register (left), the two ADC modules (center) and the TDC module (right), respectively. All the blue modules are VME-discriminator modules.

Chapter 3

Beam test at TRIUMF



Figure 3.1: Overview of Meson Hall in TRIUMF.

We have performed the beam test at TRIUMF in Vancouver in Nov-Dec 2009. The most important purpose of the beam test was to evaluate the performance of the polarimeter as a drift chamber - i.e. whether the drift chamber could measure both the muon and the positron tracks clearly. In addition, we wanted to evaluate whether the polarimeter had some spurious asymmetry due to its structure. At the same time the performance of the ASB card and the other modules were checked.

3.1 M11 beamline

Fig(3.3) shows the layout of the M11 beam channel.

The primary proton beam strikes the meson production target T1, which is typically 1 cm thick graphite. The momentum of the channel is determined largely by the magnetic field of the two bending magnets $B1$ and $B2$. Focusing is achieved by using the 6 quadrupole

magnets $Q1$ to $Q6$. There are also sextupole magnets available for a better focus, but we turned them off. The two quadrupoles $Q1$ and $Q2$ provide a double-focus at the midplane (focused in both horizontal and vertical planes), such that particles of the same momentum emanating from the object point at various angles, will all intersect at the same point at this focus.

The midplane of the channel is a plane of momentum focus, such that particles of different momenta will come to a focus at different horizontal locations along this focal plane. The momentum dispersion is $18 \text{ mm}/\% \delta p/p$. With the horizontal slits open to 90 mm full aperture, the beam channel admits a momentum bite of $5 \% \delta p/p$. The horizontal slits at the midplane can be closed to select a narrower momentum bite if desired. Also located at the midplane are a set of vertical slits which are considered to be fully open at 30 mm aperture when the septum was in operation, but which may need a larger opening to increase the flux.

The total length of the M11 channel is 15.3 meters, from production target to nominal final focus. Although the momentum range is from 60 MeV/c to 450 MeV/c, particles with a momentum of 170-180 MeV/c were used for our measurement. The current typical M11 rate is shown in Fig(3.2).

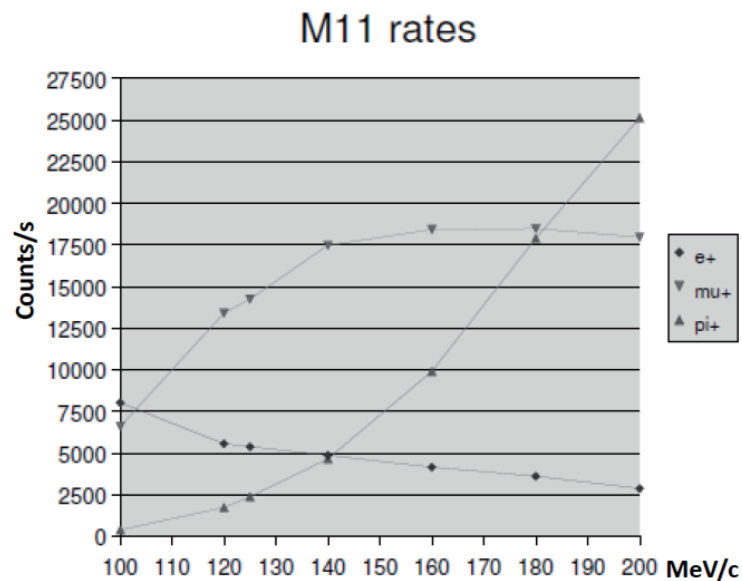


Figure 3.2: M11 beam rate

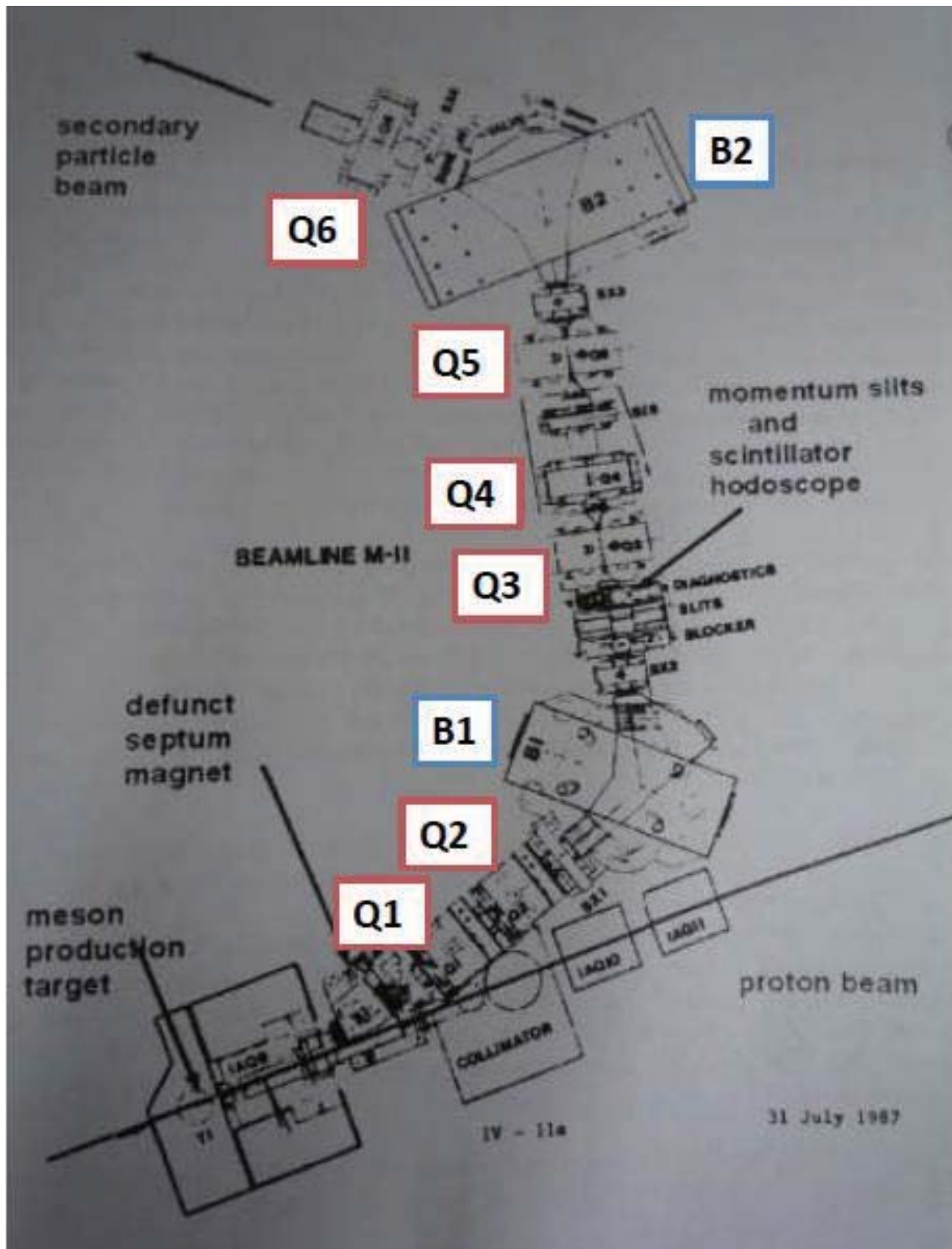


Figure 3.3: Layout of M11 beam channel

3.2 Preparation

3.2.1 Beam tuning

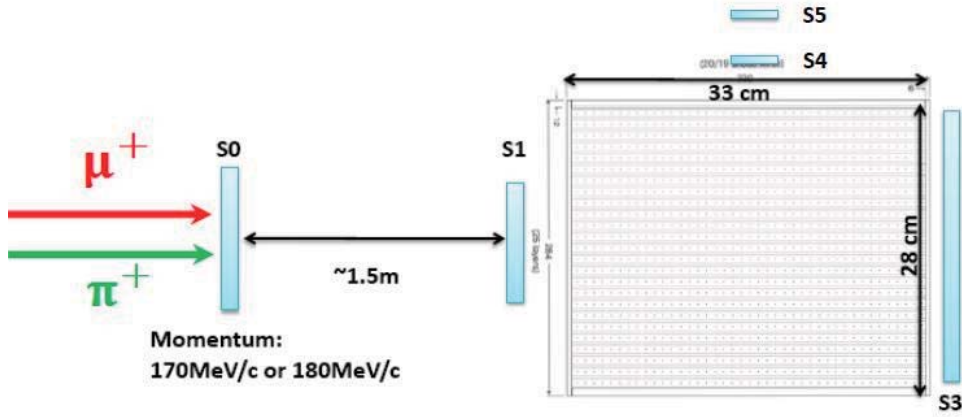


Figure 3.4: Experimental setup for beam tuning.

In order to extract and separate both muons and pions with a fixed magnet current, we tuned the beamline using S0, S1 and RF timing. These signals allowed a Time-of-Flight (TOF) measurement. The stop timing of TOF was determined by an RF signal. The experimental setup for this tuning was shown in Fig(3.4). In the beam tuning, the trigger signal was selected by triple coincidences, which consisted of S0, S1 and RF timing signals ($S0 \otimes S1 \otimes RF$). As shown in the top figure of Fig(3.5), the trigger timing was determined by the S1 counter. In addition as shown in the bottom figure of Fig(3.5), a triple coincidence signal ($S0 \otimes S1 \otimes RF$) corresponded to the time of flight between the RF timing and the S1 counter. Here, the three components correspond to the positron (fastest timing), the muon and the pion timing, respectively. In the case of a pion beam, for example, we should have added 9 ns delay to the muon signal timing. In fact, the oscilloscope's signal ($S0 \otimes S1 \otimes RF$) was consistent with the calculations based on the particle velocities (β factor) and the total beamline length (15.3 + 2 m). We finally checked the so-called TOF histogram by using a multichannel analyzer module (MCA) and an oscilloscope. Although the MCA has three functions such as integrated charge measurement, peak voltage measurement, and time difference measurement between start signal and stop signal event-by-event, the MCA was used to measure the time difference. The total TOF spectrum is shown in the top figure of Fig(3.6). Total pion counts, muon counts, and positron counts corresponded to left peak, central peak, and right peak, respectively. For measuring the spectrum, we adopted the common stop method. It was also possible to select just the pions by adding about 10 ns delay as shown in the bottom figure of Fig(3.6). Although the spectra were measured for both 170 MeV/c and 180 MeV/c beam momenta, it was a little difficult to adopt 180 MeV/c beam due to its larger muon contamination. Therefore we finally adopted 170 MeV/c as the beam momentum. In this momentum, the muon contamination at pion peak was $\sim 10^5$ times lower than pion flux.

At the same time, three counters corresponding to the S3, S4, and S5 counters were

also prepared. The S3 counter was prepared as a veto counter. In our measurement, our experimental goal was to extract the decay positron which was emitted from a stopped muon in the polarimeter. Therefore the S3 counter was suitable for selecting these events. In addition to the S3 counter, the S4 and the S5 counters were adopted as a telescope. The telescope was used in the range curve measurement. The detail of the range curve measurement will be explained in a later section.



Figure 3.5: Pictures of oscilloscope. The top one shows the S0 and the S1 counter signal which correspond to the yellow line and the blue line, respectively. The S1 counter signals appear 10 ns later than the S0 signals. On the other hand, the bottom one shows the $S0 \otimes S1$ and $S0 \otimes S1 \otimes RF$ corresponding to the yellow line and the blue line, respectively. $S1 \otimes RF$ coincidence signal has 3 components due to the three kinds of positive charged particles.

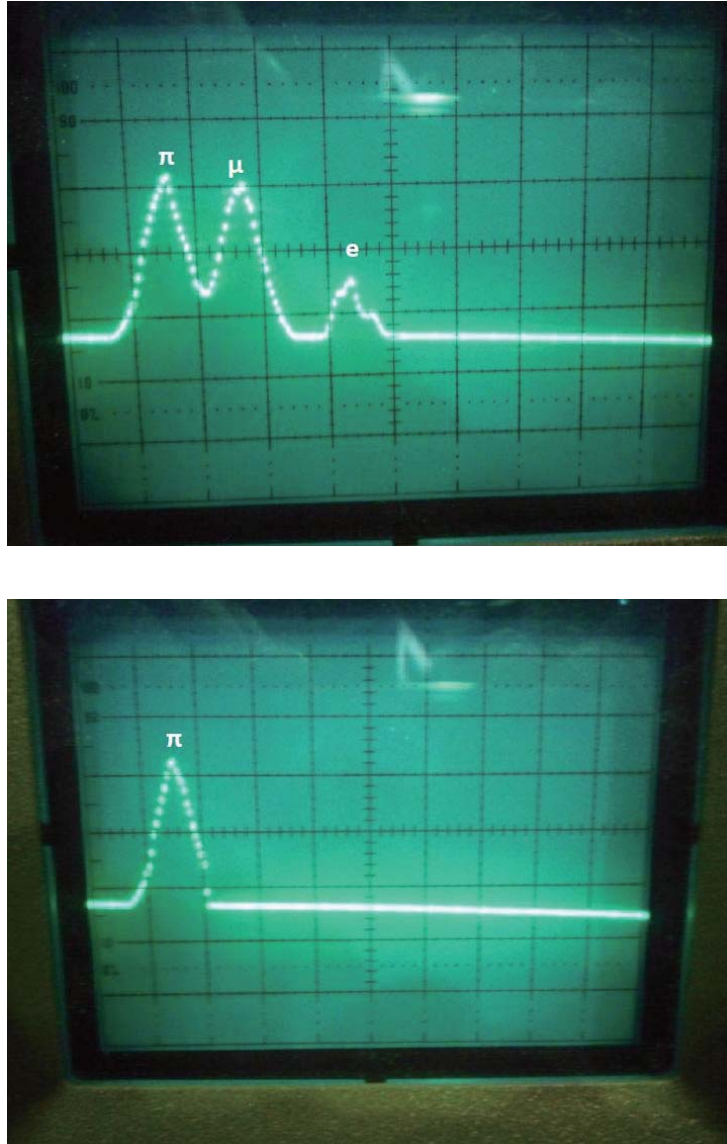


Figure 3.6: Pictures of TOF spectrum at 170 MeV/c by using the MCA. The top one shows the raw TOF spectrum showing three peaks for π , μ , and e . The bottom one shows the TOF spectrum after the RF cut. In the bottom one, pion peak including a little contamination of muons has been selected.

3.2.2 Experimental setup

Data acquisition system

The data acquisition system consisted of 16 ASB cards, 16 VME-discriminator boards, 8 CAEN ADC modules and 4 CAEN TDC modules. These amplifiers and modules have already been explained in 2.9.

The trigger logic circuit is as shown in Fig(3.10). The trigger system consisted of several trigger counters as already mentioned above. Here, I will add some explanations. The delay module which was located before the $S0 \otimes S1 \otimes \bar{S3} \otimes RF$ coincidence unit could select the kind of particle according to the length of the delay cable. Therefore, either a muon or a pion trigger could be determined by the $S0 \otimes S1 \otimes \bar{S3} \otimes RF$ coincidence unit. The main trigger coincidence unit at the lower left in Fig(3.8) had 4 channels. Each channel could be chosen according to our purpose. A-channel, for example, was used as test trigger which was available to tune the PC for data taking in addition to all VME modules. In fact, the TDC calibration was done by using the test trigger. The B-channel and the C-channel coincidence was used as the main trigger. This coincidence selected the condition of a stopped muon and a decay positron in the polarimeter. In addition the D-channel was used to measure the range curve. The downstream system of the main trigger coincidence unit consisted of several gate generators and other modules. This system provided the Gate for the ADC modules, the TDC modules, and the veto systems. For data acquisition a clock generator was needed for the TDC operation.

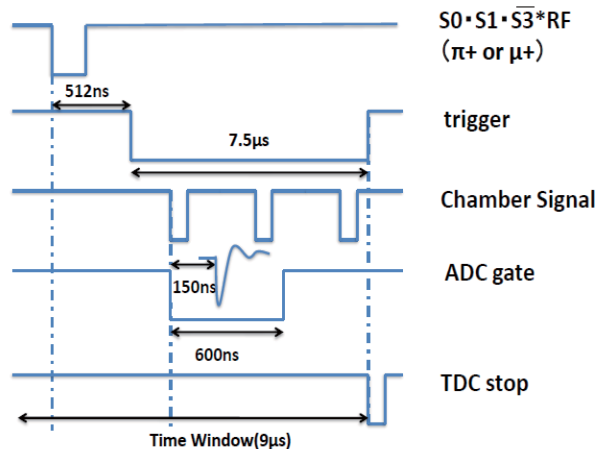


Figure 3.7: Timing chart. The ADC gate was made from the coincidence of both the delayed trigger and the chamber signals. In addition, the TDC stop has the same timing as the end of the trigger gate.

The timing chart which was associated with the main trigger is shown in Fig(3.7). The top one in Fig(3.7) shows both the pion and muon trigger signals that we named π -gate and μ -gate, respectively. Here, I will add some explanations about the trigger in Fig(3.7). This signal started about 500 ns later than both the μ -gate and the π -gate. As the ADC modules could not record multi-hit events, we had to choose the particle (incident or decay

positron) in terms of which particle data were more useful as ADC data. In terms of the charge division method, determining the decay positron track precisely was more important than the incident particle track. So the positron ADC was registered. (Of course as the CAEN TDC could registered multi-hit events, we could reconstruct both the incident π/μ and the positron tracks using the TDC data.) Considering the muon mean life time ($2.2\mu\text{s}$), it was essential to add about 500 ns delay for ensuring the decay positron event. At the same time, although less than 500 ns decay time events were discarded, the decay positron events were taken no less than 70 % as ADC data. The ADC gate was made from the coincidence of both the chamber signals and the trigger gate. One feature of the CAEN TDC, which I should especially mention, was its excellent performance of buffering. The TDC common stop was the same timing as the end of the trigger gate as shown Fig(3.7). Furthermore, it could record all the sense wire hits during the $9\mu\text{s}$ before the TDC stop. The TDC data were not associated with the ADC data.

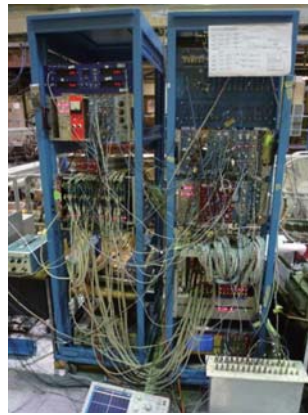


Figure 3.8: Configuration of the DAQ system.

I also show the typical chamber raw signal in Fig(3.9). As one can see in the picture, the chamber raw signal had a overshoot and some ringings due to the ASB shaping. However, this had no serious effects on the charge division method.



Figure 3.9: Typical chamber raw signal. It had an overshoot and some ringing.

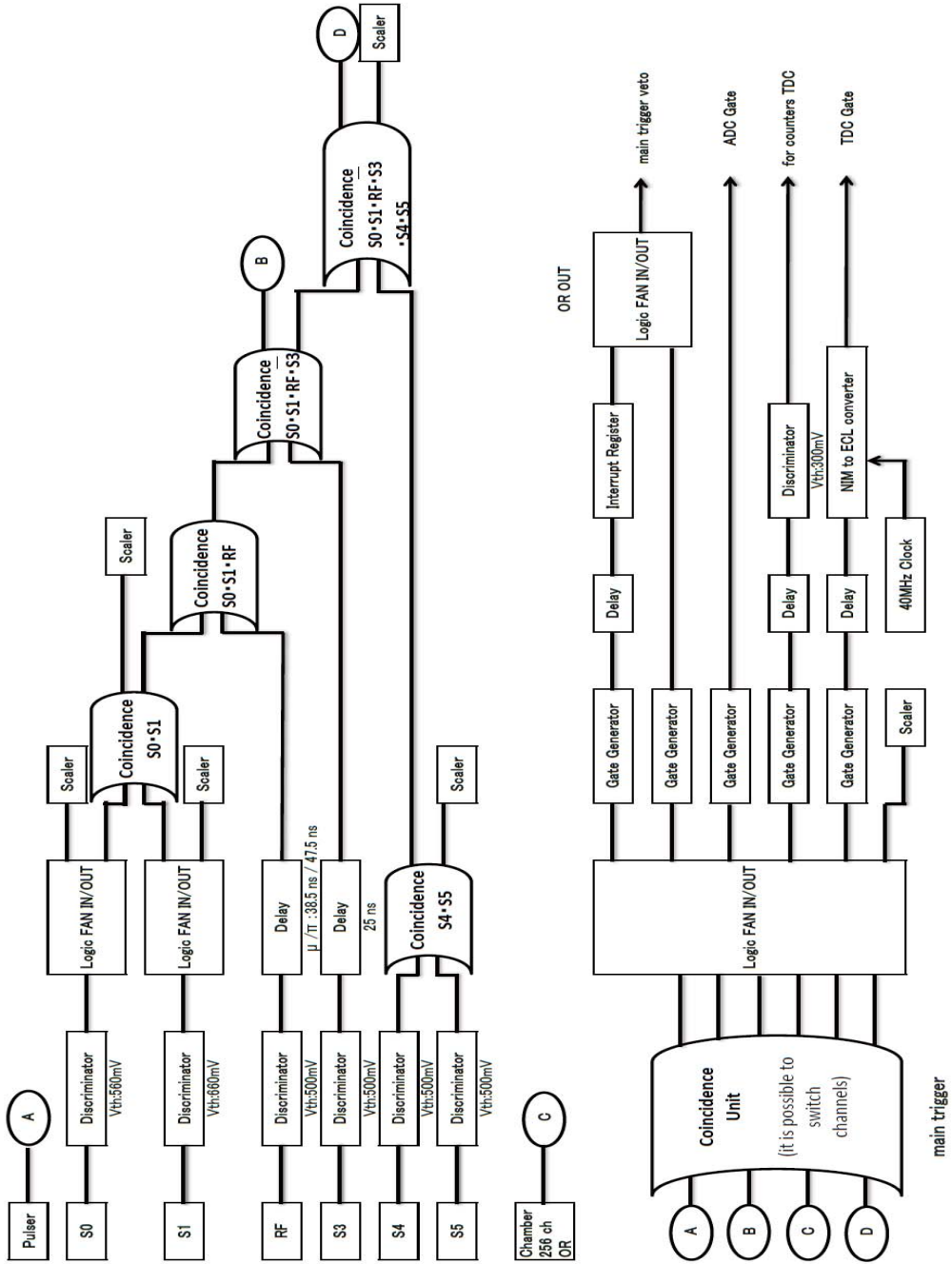


Figure 3.10: Main flow diagram of the logic circuit.

Gas system

In order to operate the polarimeter, an Ar and ethane gas mixture was adopted. The ratio was $\text{Ar} : \text{C}_2\text{H}_6 = 50 : 50$. Since the gas ratio is, in general, mainly associated with the drift velocity of the avalanche ions, keeping a constant gas ratio was very important for its operation. Because the polarimeter was carried by an airplane, there was the possibility that the polarimeter might have contained some air at first. Therefore, several complete replacements of the Ar:Et chamber gases were required before its operation.

- **Ar gas replacement**

Although we filled in the polarimeter with Ar gas, it could be possible to contain some air which entered during its flight. In order to pull out air completely, we carried out the Ar gas replacement 7 times. Since the wires were so fragile, we could not reduce the pressure below 0.3 atm.

- **Ar gas and Ethane gas replacement**

After the Ar gas replacement, we have done Ar and Ethane gas replacement bit-by-bit alternately up to 1.0 atm. We pulled out all gases bit-by-bit down to 0.3 atm again after filling up to 1.0 atm. This kind of replacement was done 3 times in total.

- **Ar and Ethane mixture gas flow**

The Ar and Ethane gases were allowed to flow with the mixture ratio from the gas house which was located outside of the meson hall with long tube transportation. We checked the mixture ratio by using a flow meter every 8 hours during the beam test.

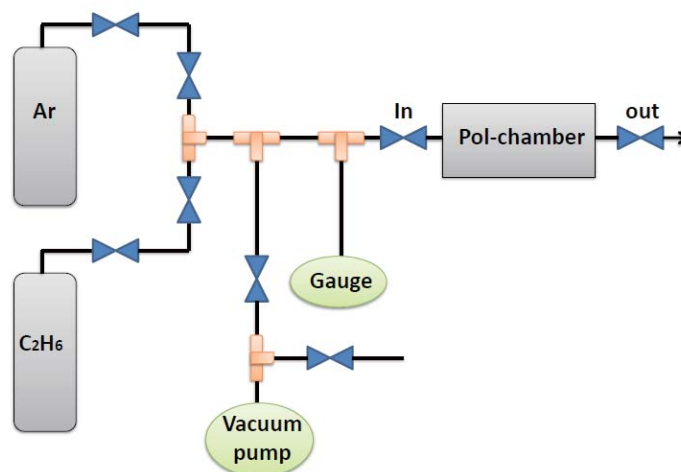


Figure 3.11: Configuration of the gas system.

3.2.3 Degradation tuning

In the beam test, the entire volume of the polarimeter should be tested to determine whether or not the polarimeter detection efficiency depended on position. Hence, we varied the stopping position of the incident particles. In order to control the stopping position, some 0.5 and 1.0 inch size Al plates were used as degrader. The Al degrader was located next to the S1 counter as shown in Fig(3.12).

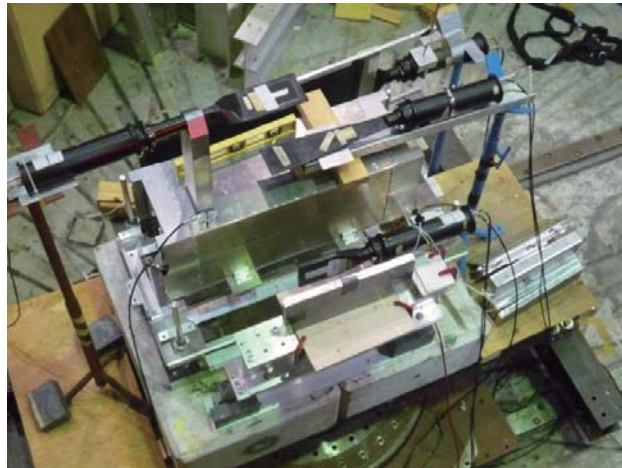


Figure 3.12: Configuration for degrader tunings.

The stopping range was divided into three regions which we called Upstream, Middle and Downstream, respectively. At the same time, the thickness of Al degrader had to be estimated for both muons and pions with 170 MeV/c momentum. Hence, the range curve measurement was classified into 6 groups.

In this measurement, the S4 and the S5 counters as shown in Fig(3.4) and Fig(3.12) were used. These counters worked as the so-called telescope. Although the telescope was just counting decay positrons, the number of counts correlated with the stopping position. The counters were placed in the transverse direction as shown in Fig(3.4) and Fig(3.12). The number of telescope counts ($S4 \otimes S5 \otimes RF$) was normalized using the number of S0 counts. The results of degrader tuning are shown in Fig(3.13). As shown in Fig(3.13), pions tended to stop in the polarimeter compared with muons because of their smaller β factor. From the downstream result, we would prefer to use a higher momentum beam so that we might not need any degrader. Considering the TOF spectrum, however, the problem of the muon contamination was more serious as compared with this problem. Therefore 0 inch was adopted as the degrader for measuring the downstream position. At the same time we could assume average stopping power of the polarimeter. Comparing Upstream data with Middle data, the pion (or muon) peak was shifted from 1.5 (or 3.0) inch to 0.5 (or 2.0) inch. In fact, although the Al plate stoppers inside the polarimeter were parallel to the beam axis, the Al stoppers stopped the incident particles due to the spread in the beam emittance. For measuring the analyzing power, the range curve were measured again using muons with the same momentum. In this measurement, a vertical stopper alignment

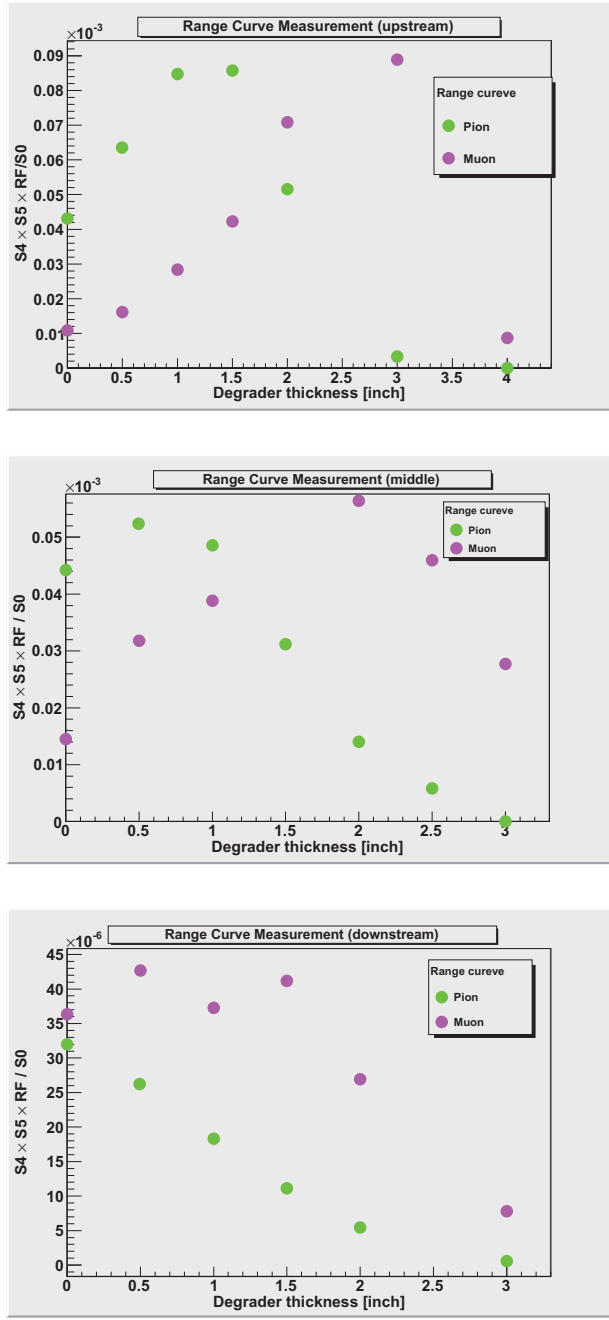


Figure 3.13: Results of the degrader tuning. Upstream (top), Middle (middle), and Downstream (bottom).

to incident beam axis was adopted. Thus, the polarimeter was rotated by 90° to the wire axis. The results of the degrader tuning are summarized in Table(3.1).

Table 3.1: Summary of degrader thickness

	Upstream	Middle	Downstream
muon	3.0 inch	2.0 inch	0.0 inch
pion	1.5 inch	0.5 inch	0.0 inch
vertical muon	-	2.0 inch	-

3.3 Measurement

3.3.1 Null Asymmetry test

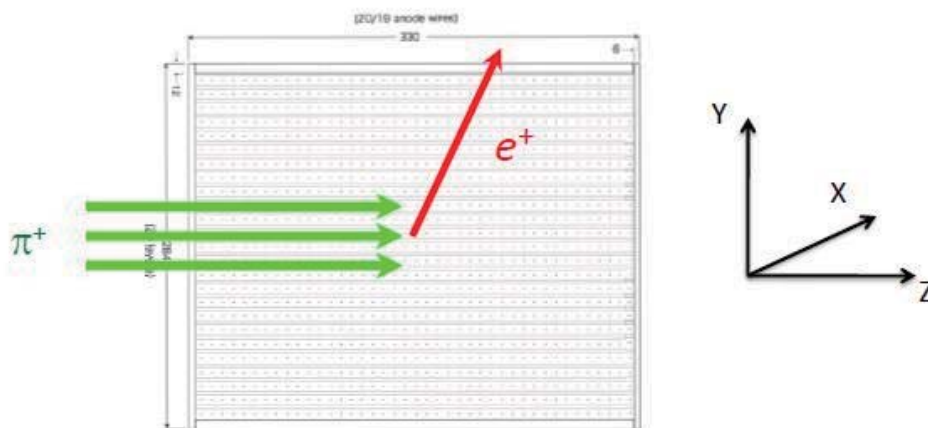


Figure 3.14: Conceptual diagram for the null asymmetry test. In this measurement, the π^+ beam was used.

The polarization measurement is based on the principle that the muon spin direction is conserved in the muon decay process due to the helicity conservation law. For a precision measurement of a small asymmetry which is associated with transverse polarization (P_T) based on *fwd/bwd* scheme, it is essential to evaluate any spurious effects generated from its mechanical structure before the start to the TREK experiment. The principle of this measurement is based on the fact that the pion is a pseudo-scalar boson with zero spin. Hence the decay muon with low momentum (~ 30 MeV/c) is emitted isotropically. Considering this feature, the resulting decay positron has to be also emitted isotropically. In terms of the principle above, the stopped pion was adopted as a good probe to search for any spurious effects.

A conceptual diagram of this measurement is shown in Fig(3.14). The configuration of the inner Al plates was parallel to the beam direction as already mentioned. The

experimental setup for the measurement was the same as the experimental setup for the degrader tunings without both the S4 and the S5 counter. In Fig(3.14), a pion with 170 MeV/c momentum enters into the polarimeter and a decay positron is finally emitted. Here, I should add some explanation about the decay muon. Most of the low momentum (~ 30 MeV/c) muons could not penetrate an Al plate. As a muon could typically travel only $200 \mu\text{m}$ in an Al plate, the muon decayed into a positron in the same Al plate in which the pion has stopped. In other words, the decay positron vertex corresponded to the decay muon position in a cell unit. Although the decay chain was $\pi^+ \rightarrow \mu^+ \rightarrow e^+$, the polarimeter could just measure both pion and positron tracks as shown in Fig(3.14).

The transverse asymmetry is defined as,

$$A_T = \frac{N_{cw} - N_{ccw}}{N_{cw} + N_{ccw}}, \quad (3.1)$$

where N_{cw} and N_{ccw} correspond to the y direction and the $-y$ direction, respectively. This definition is the same as the transverse asymmetry in $K_{\mu 3}$ decay. Although the measurement was performed for the full volume, changing the position of ASB cards was needed since we could not prepare enough number of ASB cards. The analysis results are shown in the next chapter.

3.3.2 Analyzing power measurement

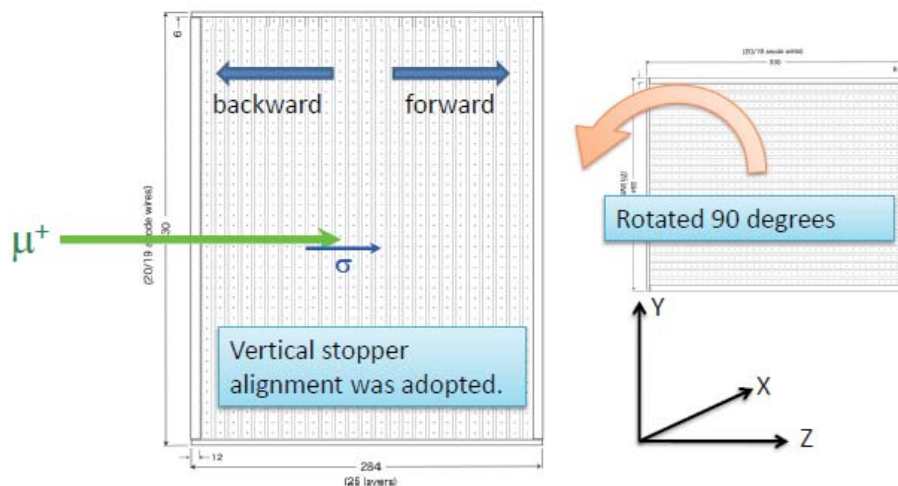


Figure 3.15: Conceptual diagram for analyzing power measurement. In this measurement, μ^+ beam was adopted.

If I can show that our polarimeter does not have any spurious effects when measuring the muon transverse polarization, then we can say that the performance of the polarimeter is good enough to measure transverse polarization in $K_{\mu 3}$ decay.

The first purpose of this measurement was, in fact, to evaluate the analyzing power. It is possible to compare with a Monte Carlo simulation to determine the analyzing power.

The purpose of this measurement was, however, not to evaluate the analyzing power but to evaluate the intrinsic beam polarization because there was no way to know the initial beam polarization. Generally speaking, surface muons with very low momentum (~ 30 MeV/c) are nearly 100% polarized. In this measurement, however, the muon momentum was much higher than the surface muons. The beam could also include cloud muons'. In general, although cloud muons also have high polarization, their polarization is lower than the surface muon's. This time the beam polarization was measured as a *fwd/bwd* asymmetry which was observable. The conceptual diagram of this measurement is shown in Fig(3.15). Before the measurement, the polarimeter was rotated by 90° around the x axis as shown in Fig(3.15). Then the configuration of the inner plates was replaced with a vertical structure. Muons with 170 MeV/c momentum enter into the polarimeter perpendicular to the inner plates and the decay positrons were emitted in upstream or downstream direction.

The longitudinal asymmetry is defined as,

$$A_L = \frac{N_{fwd} - N_{bwd}}{N_{fwd} + N_{bwd}}, \quad (3.2)$$

where N_{fwd} and N_{bwd} correspond to the z direction and the $-z$ direction, respectively. The results of the measurement are shown in Appendix C.

Chapter 4

Analysis of the beam test data

In this chapter the analysis associated with the beam test data is described.

4.1 Verification of data quality

Before the measurement, the data quality should be checked carefully. Mistakes such as cabling mismatch and misalignment of detectors could be overlooked. Thus, it was necessary to do the commissioning of the detectors and the data acquisition system. In fact, some data had to be discarded due to some hardware problems associated with the trigger.

In order to evaluate the performance of the data, the time reference spectrum (the time spectrum of the S1 counter) was checked first. As shown in Fig(4.1), the time resolution of S1 counter was obtained as $\sigma = 170$ ps. This resolution was good enough to evaluate the chamber signals because the typical sense wire time resolution scale, which was determined by the drift velocity of the avalanche ions and the cell structure, was much larger than the S1 counter time resolution scale.

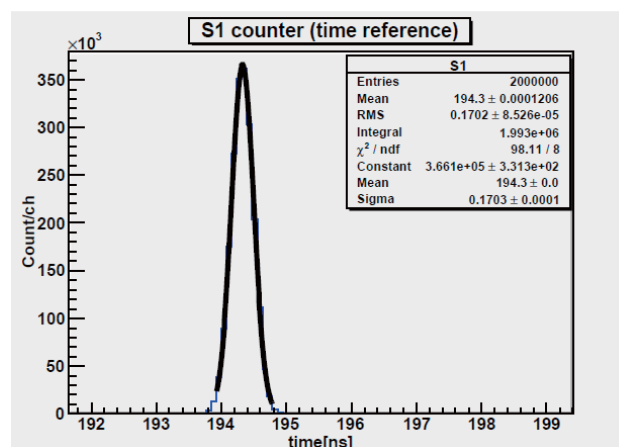


Figure 4.1: Picture of the S1 counter time spectrum. This was used to be the time reference. A 170 ps in σ time resolution was achieved. This is sufficiently high in our measurement.

Next, the muon decay curve was checked. Using the ADC trigger timing, I found that all the ADC data mainly consisted of decay positrons as expected. In fact the end of the ADC trigger gate data corresponded to a muon decay curve as shown in Fig(4.2). Actually, this data with a little contamination of pion decay could fluctuate due to drift time of the avalanche ions. In addition to the fluctuation, fitting should include the accidental region. Although the fitting was performed using an exponential function plus a constant term ($\exp[-x/\tau] + \text{const.}$), the muon mean life time was so long that we could not take enough data with time ranges over a few $10 \mu\text{s}$ scales.

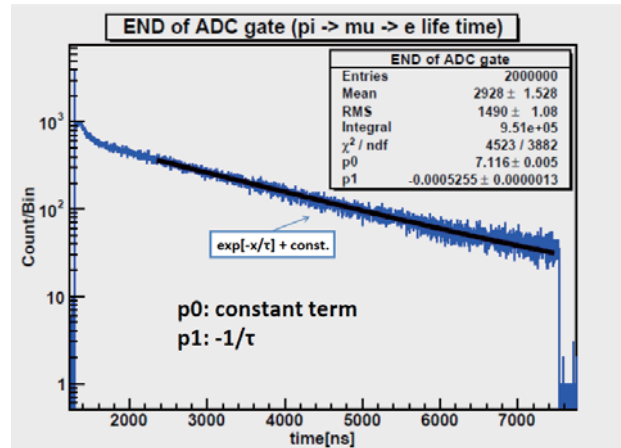


Figure 4.2: Picture of the muon decay curve. The parameter $(1/\tau)$ corresponds to $\sim 2\mu\text{s}$.

The pictures of single wire ADC and TDC data are also shown in Fig(4.3 - 4.4). Regarding the ADC data, a so-called pedestal suppression was performed. Namely, before actual data taking, the pedestal was fitted by Gauss function channel-by-channel in order to suppress all data except for the event of the decay positron. These pedestal data actually did not correlate with the TDC data of the decay positron.

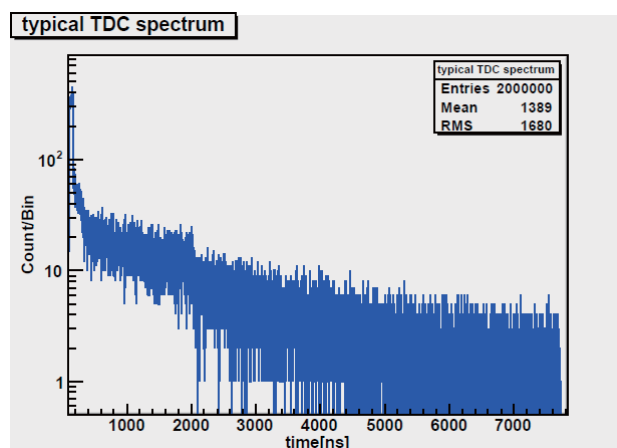


Figure 4.3: Picture of the TDC data corresponding to a single wire. The TDC spectrum composed of the decay positron hit with a small fraction of the incident particle.

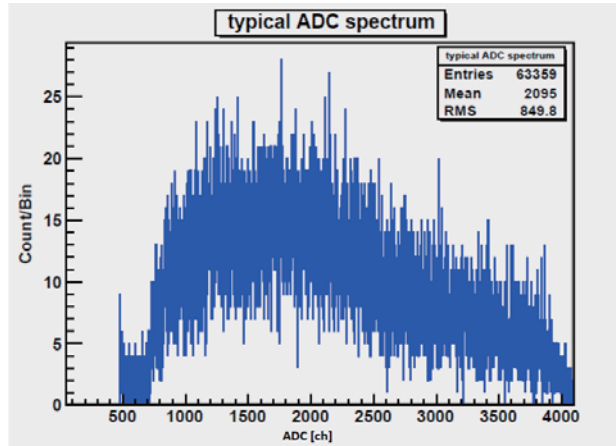


Figure 4.4: Picture of the ADC data after a pedestal suppression. The figure corresponds to a single wire hit. The ADC spectrum is completely composed of the decay positron due to the delayed trigger as mentioned in Chapter 3.

Next, a misalignment of the wires with regard to both hardware and software was checked by looking the incident particle tracks. In fact, the alignment of the wires was more complicated. In the beginning of the tracking in a cell unit, although most of the incident particle tracks were made successively, there were no continuous tracks in some events. After some changes of the analysis code, both pion and muon tracks were made much more clearly as shown in Fig(4.5). Here, the ASB cards were attached in the red region in Fig(4.5).

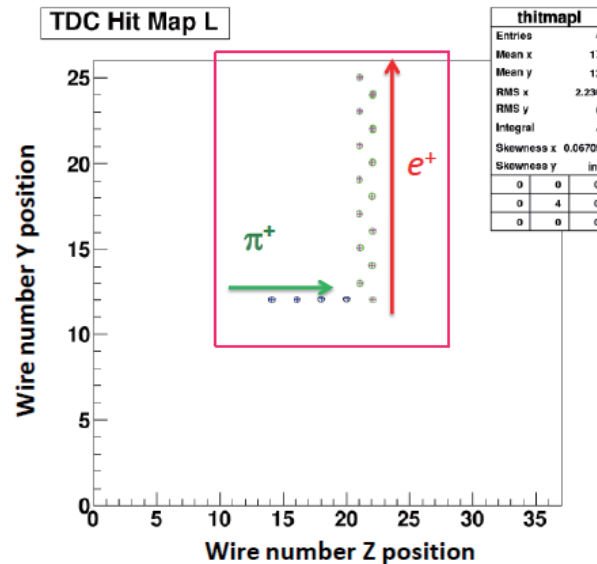


Figure 4.5: Sample track. In this picture, the pion enters into polarimeter and the decay positron is finally emitted.

After the evaluation of the tracking performance, the incident beam stopping distribution with respect to the result of the range curve measurement was checked. The stopping distribution also played an important role as a cross check probe of the misalignment of wires. For analyzing the stopping distribution, two conditions were required.

- 1) In the beginning of the analysis, only the timing which corresponds to the incident particle was selected in order to avoid the positron contamination.
- 2) In addition, the stop position was defined as the most downstream position of the incident particle in a cell unit.

The resulting distribution is shown in Fig(4.6).

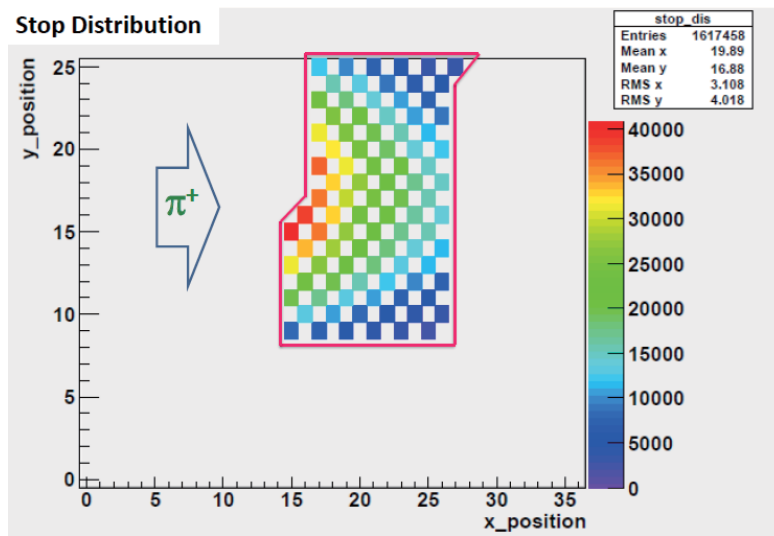


Figure 4.6: π^+ stopping distribution. It seems that incident pion stops ASB region with concentric circles. Its central position tends to concentrate upstream of the full ASB region.

From the picture, the incident particles were spread over the ASB region as concentric circles. The consistency of the shape with concentric circles means that there was no misalignment with respect to the wire configuration in my analysis code. The results also showed that the degrader tuning was roughly successful although the stop position of the incident beam tended to concentrate in the upstream ASB region. The central position of its distribution, however, did not have a bad influence on the physics data associated with any spurious asymmetry but it just decreased the number of good events.

4.2 Wire efficiency

The most important parameter of a tracker is its detection efficiency¹. In most cases, a chamber is required to have $\geq 99\%$ detection efficiency. It is difficult to reconstruct particle tracks if the detection efficiency is not high enough. Since the wire efficiency² correlates with the detection efficiency, an evaluation of the wire efficiency is needed. In our measurement, the efficiency of the chamber was evaluated using the muon beam data. The efficiency is defined as follows and as shown in Fig(4.7). In addition, the alignment of ASB cards are also shown in Fig(4.7).

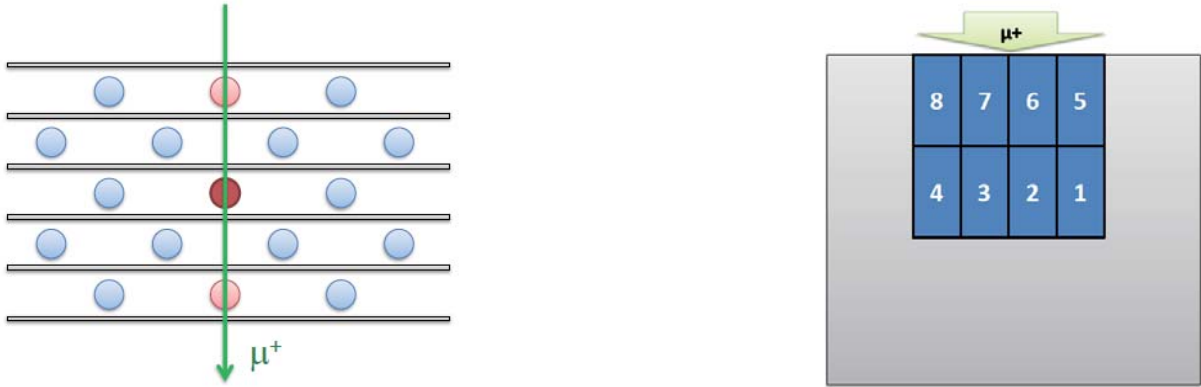


Figure 4.7: Configuration of the Al plates (left) and the ASB cards (right).

- The 3 wires parallel to the incident beam were selected for the whole volume of the chamber.
- In case that the hits of the pink wires were required, whether the red wire was tagged or not.

Considering this definition, it seems that the incident particle should always pass through the cell including the red wire. The result of this analysis, however, is not the same as this assumption as shown in Fig(4.8). From this graph, it was clear that the wire efficiency depended on its position. The tendency of this dependence shows that the efficiencies of the wires located downstream region are lower than upstream region. The wires corresponding to the ID from 0 to 64 are located in the downstream and the wires corresponding to the ID from 65 to 128 are located in the upstream, respectively. However, since some wires are outside of the fiducial volume, it is impossible to determine the efficiency for them. Moreover, since the number of events corresponding to the downstream regions are lower than in the upstream case, the downstream efficiencies often have a large error bar. The tendency of this graph could be explained as a multiple scattering effect. This polarimeter was different from other trackers in terms of its material density. In general, a tracker should be made of light material in order to prevent secondary emission or particle

¹Here, the word “detection efficiency” is defined as whether a particle trajectory can be seen or not.

²the word “wire efficiency” is defined as whether a wire responses or not in the case that a particle passes thorough the same cell as the wire.

scattering. On the contrary, this polarimeter was made of material with some density in order to stop the incident particles in the volume. A polarimeter with larger density causes some bad tracks because it was difficult to prevent these effects. Considering the multiple scattering effects, the efficiency should be evaluated not by wire but by layer. Hence, the efficiency should be redefined as follows and shown in Fig(4.9).

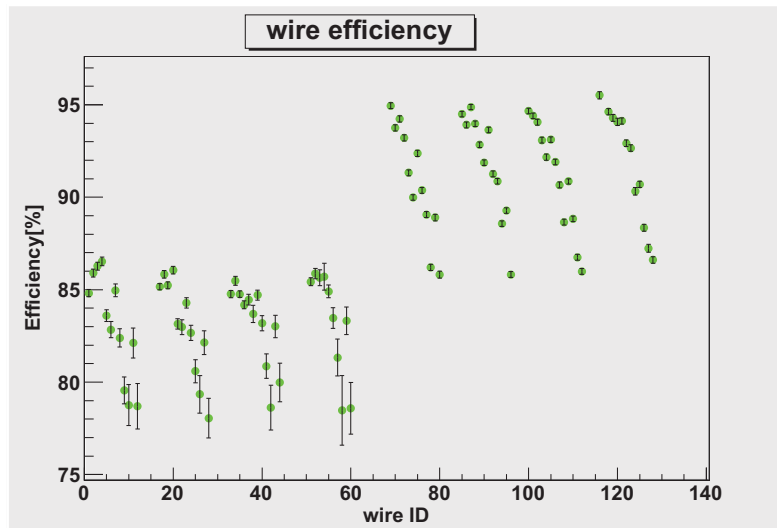


Figure 4.8: The first results of the wire efficiency measurement. These efficiencies relied on the position of a sense wire due to multiple scattering effect.

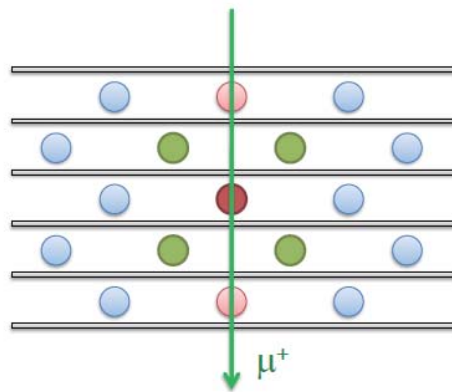


Figure 4.9: Schematic view of the Al plates and the new definition of the wire efficiency.

- The 3 wires parallel to the incident beam were selected for the whole volume of the chamber. (the same definition as above)
- In case that the hits of the pink wires were required, whether the red wire was tagged or not.
- In the case that the red one was not tagged, the green wires are checked whether two of them (left/right) were tagged or not. Namely, the other two possibilities that the incident beam passes through the left or right cell were allowed.

The result of this definition is shown in Fig(4.10). It shows that the wires had high efficiencies.

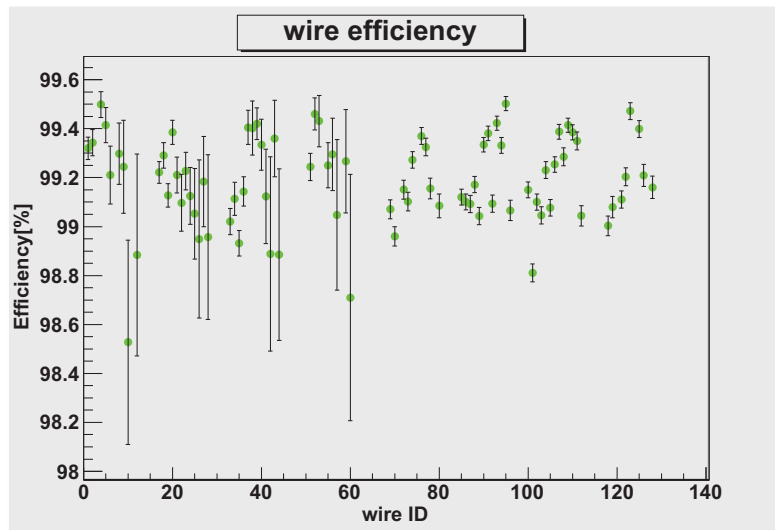


Figure 4.10: Final result of the detection efficiencies in a cell unit. This included the correction of the multiple scattering effect.

4.3 Event selection

Before the main analysis, it is essential to extract clean tracks with no-bias. It is not until some kind of selection for extracting fine tracks is performed correctly that the track reconstruction analysis and the transverse asymmetry analysis can be started. The following selections were performed in my analysis.

- **Time classification**

Based on the TDC hit timing, the TDC data were classified into 11 categories as 0-2500 channels, 2500-10000 channels, ..., 80000-90000 channels, and 90000- channels (1 channel = 80 ps). Here, I named the first category “*BEAM*”. In this case, “*BEAM*” included just the incident particles. There is no positron contamination in this group due to the 500 ns delayed trigger gate. In addition, some events have some different timings which belong to more than 3 categories, respectively. These strange events were discarded. Finally the events which belong to both “*BEAM*” and one of the other groups were selected as a true track.

- **Geometrical classification**

Next a geometrical classification was adopted in order to eliminate some noise hits and to rescue inefficient hits. At first, considering inefficient hits, the hit cells were

connected from upstream towards downstream in a cell unit. Finally, the incident track was formed as a straight line. Therefore, as some noise hits were not included in a line, the events which did not form a line were discarded. This method was also adopted for the positron track. In fact, since the decay positron has a low momentum, the positron tended to generate secondary particles. Thus, a positron could make two lines. In this case, it was difficult to extract the true positron track, so these events were also discarded.

- **Vertex selection and classification**

Finally, the vertex cell was defined as the final cell of the incident line. Here, the vertices were classified into 2 categories whether the positron hit cells overlapped the incident track or not. In case that there were more than 2 cells overlapping, these events were also discarded because they could include some hits caused by secondary particles. The events which had zero or one cell overlapping were ultimately chosen. In order to avoid some kind of bias associated with an incident angle of the beam, the condition that all incident particles have to pass through more than 3 cells parallel to the Al plate, was also required. In other words, all events are satisfied with the condition that incident particles enter into the polarimeter parallel to the Al plate.

4.4 Development of the track reconstruction

Based on these event sections above, the track reconstruction, in particular the positron reconstruction, algorithm was developed. In this algorithm, it is essential to determine the X-T relation first, which is corresponding to drift velocity of the avalanche ions. (Here, X and T are the position and drift time, respectively.) The algorithm of the X-T relation will be described in detail in the Appendix B.

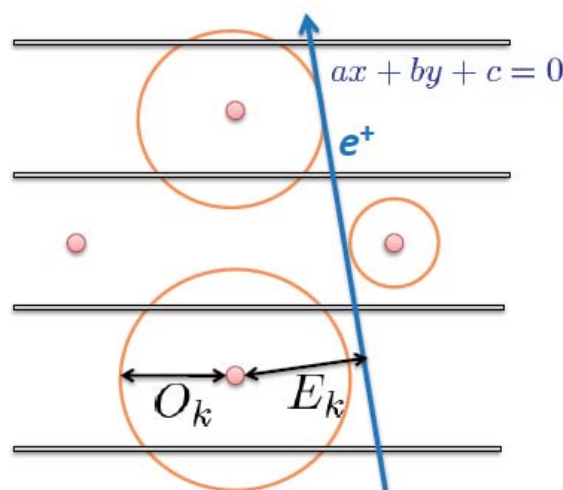


Figure 4.11: Schematic view of the track reconstruction.

In the beginning of the analysis, some parameters below as shown in Fig(4.11) are defined as,

$$\begin{aligned} E_k &= \frac{|ax_k + by_k + c|}{\sqrt{a^2 + b^2}}, \\ O_k &= X(t - t_0), \\ \sigma_k &= \sigma(t - t_0), \end{aligned} \tag{4.1}$$

where k is the identification number of the wire, E_k is a distance between the sense wire and the fitting line, O_k is a radius of equi-drift-time line, and σ_k is a fluctuation of equi-drift-time line. Here, O_k and σ_k have already been determined as the results of X-T relation. Furthermore, since σ_k included a fluctuation of the incident angle, we could regard the equi-drift-time line as a full circle. Then, χ^2 was defined using these parameters as

$$\chi^2 = \sum_k \frac{(E_k - O_k)^2}{\sigma_k^2}. \tag{4.2}$$

The fitting of the decay positron was performed based on a principle of minimum χ^2 . Here, we should pay attention to the fact that the fitting function has four free parameters corresponding to a , b , c , and t_0 . In my analysis, it was essential to determine t_0 because we could not use a counter for measuring the t_0 . Since there was no information for determining t_0 , I had to evaluate t_0 as a free parameter. In addition, considering that the fitting was performed using the four parameters, more than 5 hits in a cell unit were required for the analysis. Thus, the fiducial volume of the polarimeter including the vertex cell was chosen as a small region. The resulting pictures are shown in Fig(4.12 - 4.13).

Although the fitting was performed based on this simple method, the resulting tracks were quite clean. Due to the adoption of the X-T relation based not on the simulation but the experimental data, it was possible to do a simple analysis even if the cell structure is a little complicated. On the other hand, as shown in Fig(4.14 - 4.15), I will show some other pictures below as the bad examples.

The bad events included positron scattering due to the large material density in the polarimeter. As a matter of course, the bad track events have larger χ^2 than clean ones. As mentioned above, the algorithm should be remade with some requirements as follows.

- In order to increase the number of good events after the fitting, the algorithm has to overcome scattering events. For overcoming the scattering, the Kalman Filter method [49], which can recover the positron scattering event, should be adopted in the near future.
- Since the resolution of positrons includes the angular uncertainty, the algorithm has to be free from this kind of uncertainty. For avoiding this kind of uncertainty, a

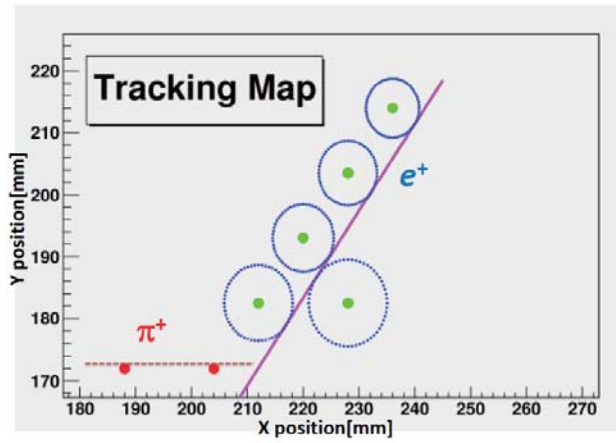


Figure 4.12: Sample picture of the decay positron fitting 1.

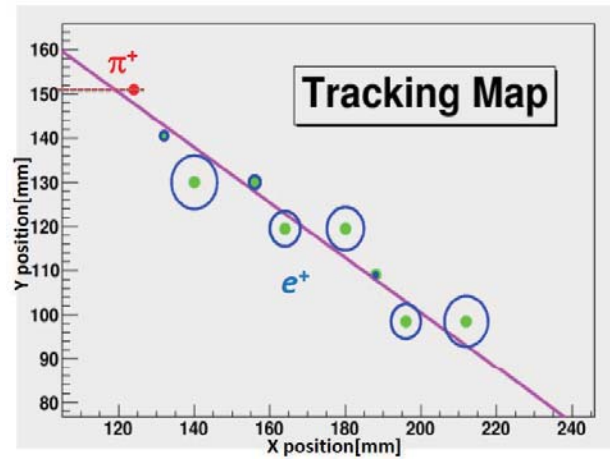


Figure 4.13: Sample picture of the decay positron fitting 2.

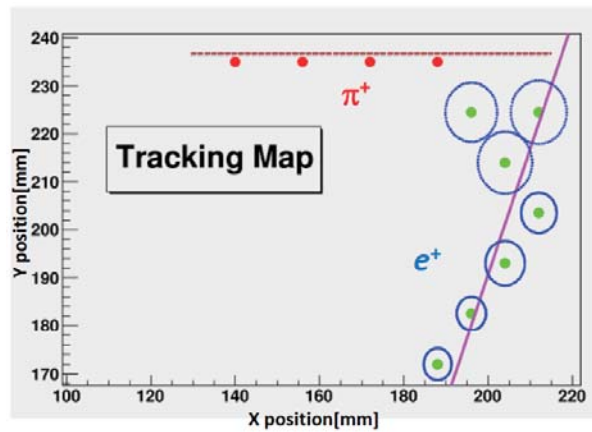


Figure 4.14: Sample picture of the decay positron fitting 3.

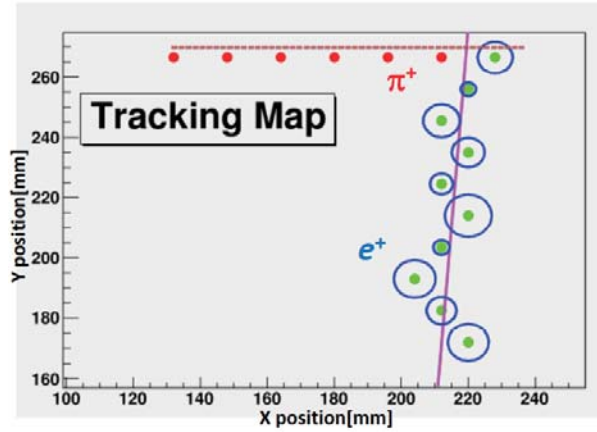


Figure 4.15: Sample picture of the decay positron fitting 4.

simpler and more symmetric cell structure should be adopted, namely we should determine the X-T relation based on the experimental data.

4.5 Spurious asymmetry

The spurious asymmetry associated with the chamber structure is discussed in this section.

4.5.1 Data analysis

Based on the event selections described in 4.3, the good events were extracted. The number of extracted good events was 5 times lower than the number of total events. Now the transverse asymmetry analysis could be started. As mentioned in Chapter 3, the transverse asymmetry was defined as,

$$A_T = \frac{N_{cw} - N_{ccw}}{N_{cw} + N_{ccw}}, \quad (4.3)$$

where N_{cw} and N_{ccw} correspond to the y direction and the $-y$ direction, respectively. The configuration of the setup is also shown in Fig(4.16).

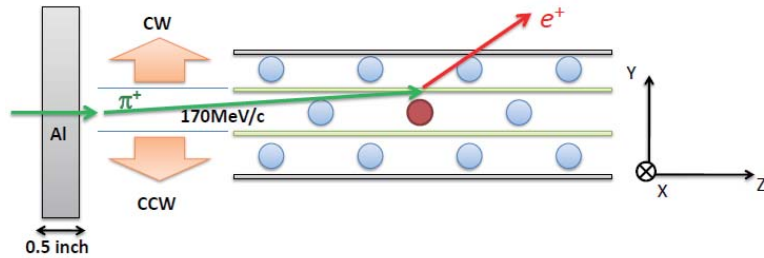


Figure 4.16: Schematic view of the null asymmetry measurement and the definition of axis.

For non-bias analysis to be performed correctly, it was essential to keep the configuration of the sense wires symmetric with respect to the beam axis. Assuming that the configuration of the sense wires is not symmetric with respect to the beam axis, it is natural to generate some spurious asymmetries associated with its configuration even if all the sense wire efficiencies are exactly the same. Hence, the analysis was performed based on keeping the configuration of “*selected sense wires*” to the vertex cell symmetric with respect to both the transverse and the beam axis. Here, “*selected sense wires*” means the 14 sense wires around a vertex. At the same time, the analysis was performed using just “*selected sense wires*” with respect to a vertex. As the result of these requirements, it was necessary to narrow the fiducial volume down to several cells. The results of this analysis are shown in Fig(4.17).

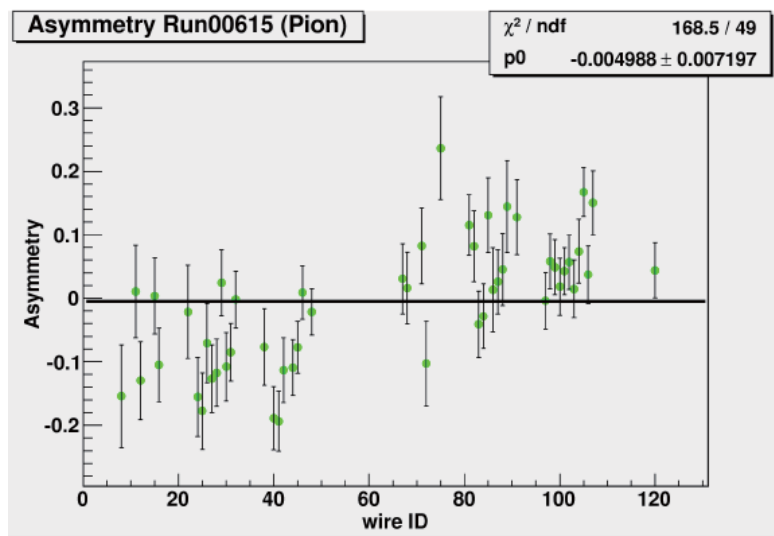


Figure 4.17: Result of null asymmetry measurement. A large spurious asymmetry appears. It depend on the wire position.

As shown in Fig(4.17), a large spurious asymmetry appears in the data. Considering that the configuration of the ASB cards was the same as for the wire efficiency measurement, the graph shows that the positron tended to be emitted in the same direction as the location of ASB card. In other words, the positron tended to be emitted upward (downward) in case that vertex cell was located upward (downward). Here, upward (or downward) is the perpendicular direction with respect to the inner Al plates. These directions correspond to the *cw* and the *ccw*, respectively. This tendency is shown in Fig(4.18). It was difficult to explain this fact as the wire efficiency fluctuation even if there were some 50 % intrinsic efficiency wires. It was clear that this picture had a structure related to the experimental conditions.

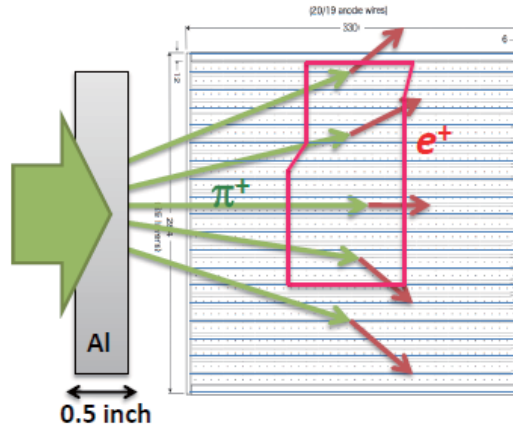


Figure 4.18: Schematic view of the decay positron emission. The tendency shows that the positron tended to be emitted upward (downward) in case of a vertex cell located upward (downward).

Therefore I considered the possibility that the incident pions also contained some muons generated from π^+ decay in flight. Can this explain the structure of Fig(4.17) even if the incident pions contained this kind of muon? To explain Fig(4.17), it is essential to meet two requirements as follows.

- **the positive helicity muon was stopped in the volume**

Suppose that the muon did not have any polarization, then the positron will be emitted isotropically. One possibility is that only high polarized muons with positive helicity were coming into the polarimeter and they were stopped in the volume. Positive helicity muons could make the spurious structure in Fig(4.17).

- **this muon was emitted with some incident angle**

Suppose that a polarized muon was coming into the polarimeter parallel to the inner plates, the muon could stop both upward and downward of the inner plate. The probability that the muon was stopped in the upper (lower) plate was 50 %. The resulting positrons will then be emitted in both upward and downward directions with the same ratio. Thus, the muon should be coming into the polarimeter with some incident angle.

Does this possibly satisfy these requirements?

Here, I will summarize the features of muons from pion decay in flight.

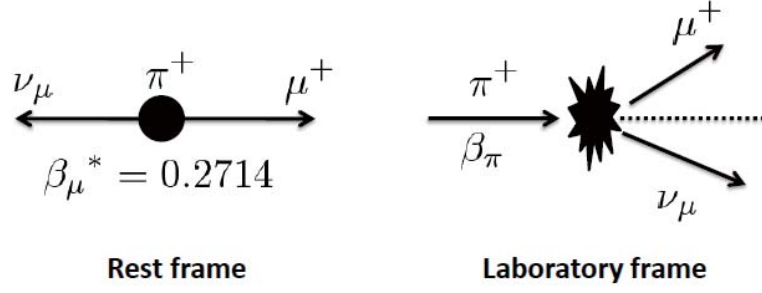


Figure 4.19: Schematic view of pion decay in rest frame (left) and laboratory frame (right).

In $\pi^+ \rightarrow \mu^+$ decay, the muon momentum in the pion rest frame is 29.8 MeV/c and its direction is isotropic. In the laboratory frame, where the pion moves with momentum p_π , the muon momentum has a flat distribution between the two limits:

$$\begin{aligned} p_\mu^{FWD} &= (\beta_\pi + \beta_\mu^*)p_\pi / [\beta_\pi(1 + \beta_\mu^*)] \\ p_\mu^{BWD} &= |\beta_\pi - \beta_\mu^*|p_\pi / [\beta_\pi(1 + \beta_\mu^*)] \end{aligned} \quad (4.4)$$

where $c\beta_\mu^*$ is the muon velocity corresponding to its 28.9 MeV/c momentum from pion decay at rest. These limits correspond to forward and backward decays in the pion rest frame. Since muons with momenta at both of these limits move along the initial pion direction, they are easy to transport. Furthermore, they have defined polarizations of +1 and -1, respectively. The muon momentum distribution for a given pion momentum and the corresponding decay angle in the laboratory frame are shown in Fig(4.20) and Fig(4.21) [50].

In our case since the pion momentum was 170 MeV/c, both FWD and BWD muon momenta were as follows.

$$\begin{aligned} p_\mu^{FWD} &= 173 \text{ MeV}/c \\ p_\mu^{BWD} &= 86 \text{ MeV}/c \end{aligned} \quad (4.5)$$

Therefore considering that the polarimeter has a finite stopping power, only BWD muons could be stopped in the fiducial volume. In addition, the BWD muons could be emitted with some incident angle due to the fact that the pions were boosted. Thus, the hypothesis could meet these requirements.

In order to estimate how many BWD muons could be contained in the pion beam under our experimental condition, it was essential to consider how to produce the muons in the beamline. In general, there are three types of muon production according to the spatial position (with respect to the target) where $\pi^+ \rightarrow \mu^+$ decays take place. These are decay μ , cloud μ and surface μ , respectively. Conceptual views of these three types of muons are shown in Fig(4.22) [50].

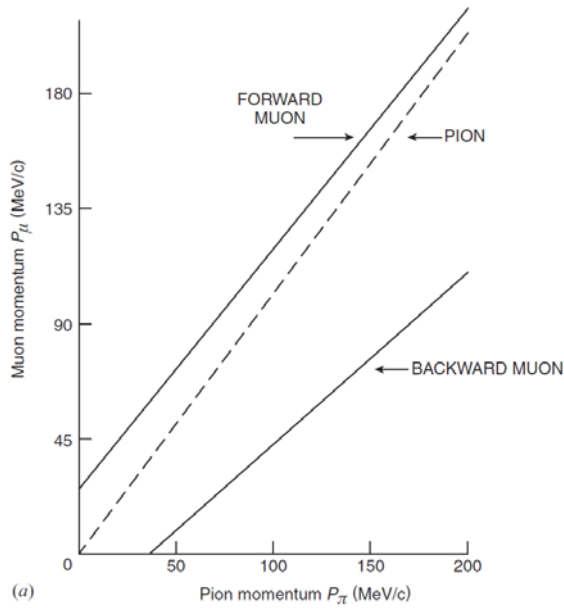


Figure 4.20: Summary of properties of decay muons. Momentum distribution.

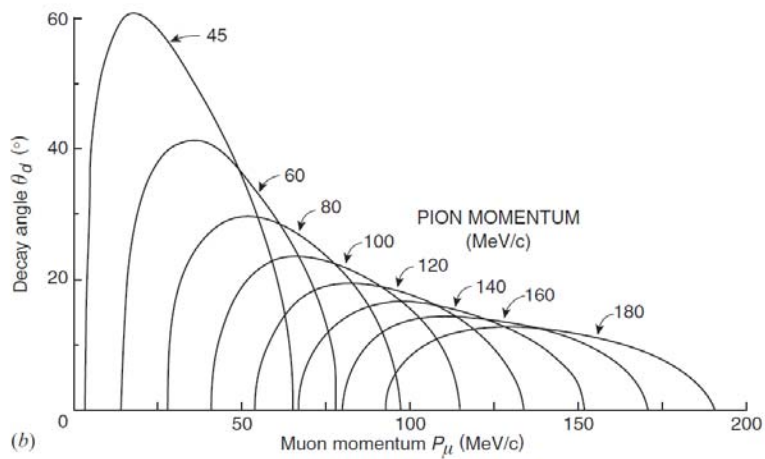


Figure 4.21: Summary of properties of decay muons. Decay-cone aperture angle for muons produced by pion decay in flight.

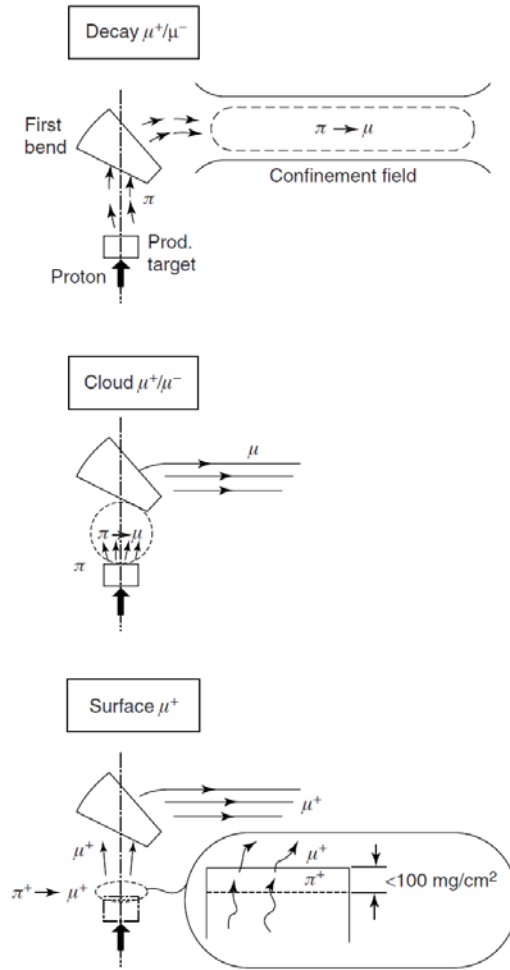


Figure 4.22: Three types of muon source (surface μ^+ , cloud μ^+ , and decay μ^+) produced by energetic protons from accelerators.

Of particular interest to us is the BWD muons because only they could be stopped in the fiducial region. In addition, their momentum (about half of p_π) is far from the initial beam momentum and so they can be cleanly separated from other particles such as π or e by bending magnets. Furthermore, muons of lower momentum have a higher stopping density.

In general, the surface muons are a monochromatic beam with low momentum of 29.8 MeV/c. So the surface muon cannot be a candidate. The cloud muons produced between the production target and the B1 bending magnet take the form of a cloud around the target and can be transported together with the pions as shown in Fig(4.22). Since the momenta of the parent pions are unknown, these muons do not satisfy any kinematic condition to assure their polarization, namely they are a mixture of FWD and BWD muons. Therefore, their polarization was expected to be small. In addition, such cloud muons with 170 MeV/c momentum can be eliminated using TOF due to the fact that their timing is faster than the pion timing. Furthermore the BWD muon produced between the B1 and the B2 do

not pass through the B2 due to its low momentum. Hence, the only candidate remaining is the BWD muon produced between the B2 and the polarimeter as shown in Fig(4.23).

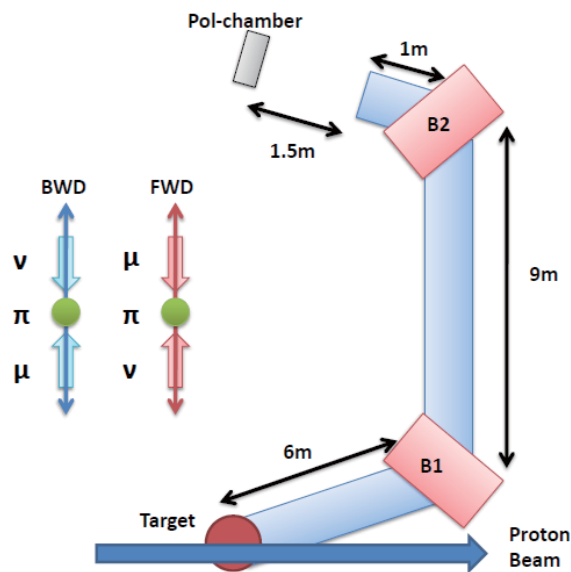


Figure 4.23: Schematic view of the M11 beamline. BWD muons could be produced after the B2 magnet.

Considering that the length between the B2 and the polarimeter was nearly 2.5 m, BWD muons delayed nearly 2.4 ns with respect to the pion timing. This means that the contamination of such BWD muon in the pion peak could not be avoided. On the other hand, since the FWD muons were at least 1.0 ns faster than the pion timing, their contamination in the pion peak was negligible.

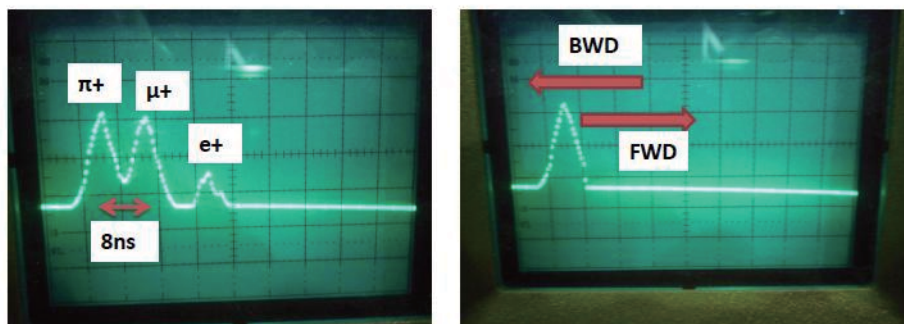


Figure 4.24: TOF spectrum. BWD (FWD) muon could be contained in the pion peak toward the left (right) direction.

However, it is difficult to discuss the quantitative evaluation. Here, in order to solve the structure in Fig(4.17) completely, it was necessary to introduce a simulation based on Monte Carlo (MC). In the next subsection, an evaluation of spurious asymmetry was done using a Geant4 simulation.

4.5.2 Simulation

Before the main discussion, the simulation data quality was confirmed. It goes without saying that the muon polarimeter must be able to measure the muon spin using the decay positron. Therefore, whether the muon spin behaves correctly or not was verified repeatedly in the simulation. In order to confirm the muon spin behavior, 100 % polarized BWD muons were generated.

First of all, the configuration of polarimeter was reproduced completely without either sense or potential wires as shown in Fig(4.25).

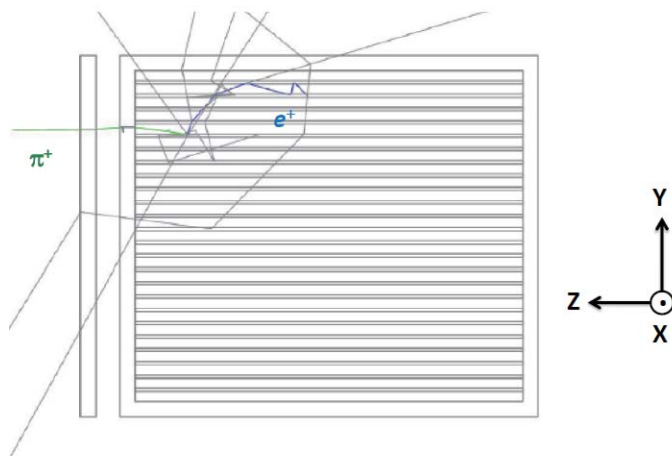


Figure 4.25: A polarimeter constructed in Geant4 simulation. In addition, main axes were also defined. Here, the incident beam was incoming toward the $-Z$ direction.

After the polarimeter and the degrader was reproduced, the muon beam was shot toward the $-Z$ direction. For keeping with the experimental conditions, the beam was shot from the B2 bending magnet. Here, we should pay attention to the configuration of the inner plates. In this muon run, the inner plate configuration was changed to be perpendicular to the beam, corresponding to the polarization measurement. Of course the degrader was also changed based on the range curve measurement. The beam profile was spread in both the x and the y direction keeping a gaussian shape as shown in Fig(4.26). The profiles, however, were not compared with an actual beam profile since we did not scan it. The beam profiles and emittance were not scanned because we did not install any beam tracker in our experimental setup.

Next the BWD muon status was evaluated. The results are also shown in Fig(4.27). Here, I should add an explanation about the muon decay rate to understand the graph of the positron emission angle with respect to beam axis. In general, the muon decay rate is a function of the energy and emission angle of the decay positron. Thus, the differential

decay rate integrated energy function is obtained as,

$$\frac{d\Gamma}{d\cos\theta_e} = \frac{1 + \alpha_e \cos\theta_e}{2}, \quad (4.6)$$

where α_e is determined by the solid angles of the positron. Assuming that the analysis is done considering a 4π solid angle, then α_e is exactly equal to $1/3$. Here, I define the probability p_+ (or p_-) that the decay positron is emitted in the same (or opposite) semi-sphere as the muon spin polarization as,

$$p_+ = \int_0^1 \frac{1 + \alpha_e x}{2} dx = \frac{7}{12},$$

$$p_- = \int_{-1}^0 \frac{1 + \alpha_e x}{2} dx = \frac{5}{12}. \quad (4.7)$$

Namely, in case that a 100 % polarized BWD muon was shot toward the polarimeter, the same semi-sphere probability has to correspond to just $7/12$. The result of the decay positron direction (FWD/BWD) was consistent with $7/12$ as shown in Fig(4.27). Furthermore, verification of the positron energy spectrum was done. It was consistent with well-known Michel spectrum.

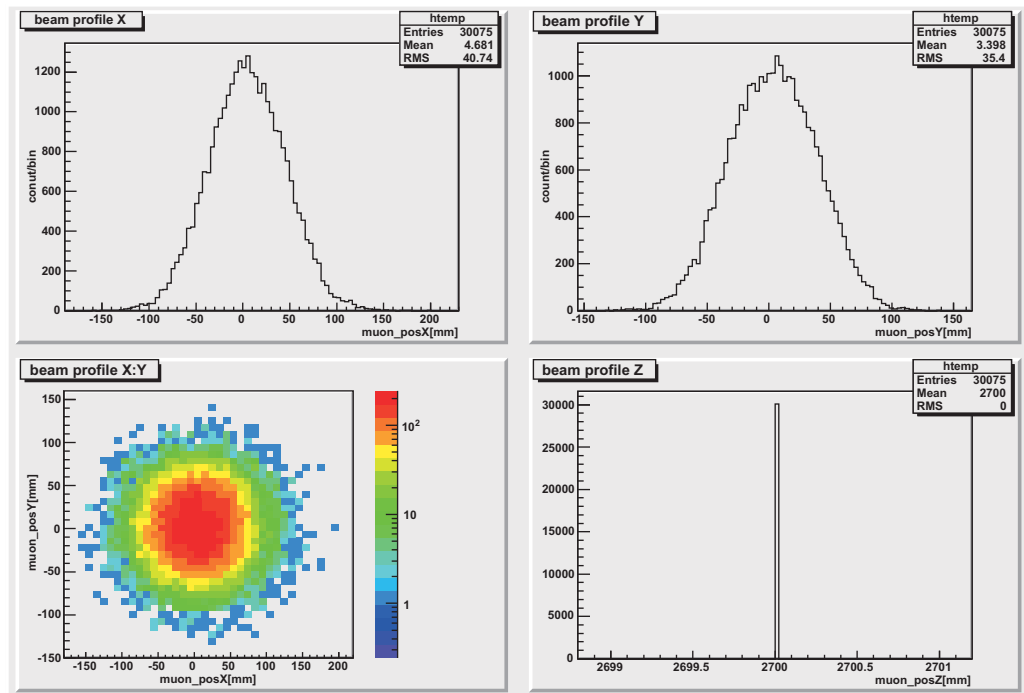


Figure 4.26: Incident π^+ beam profiles in Geant4 simulation

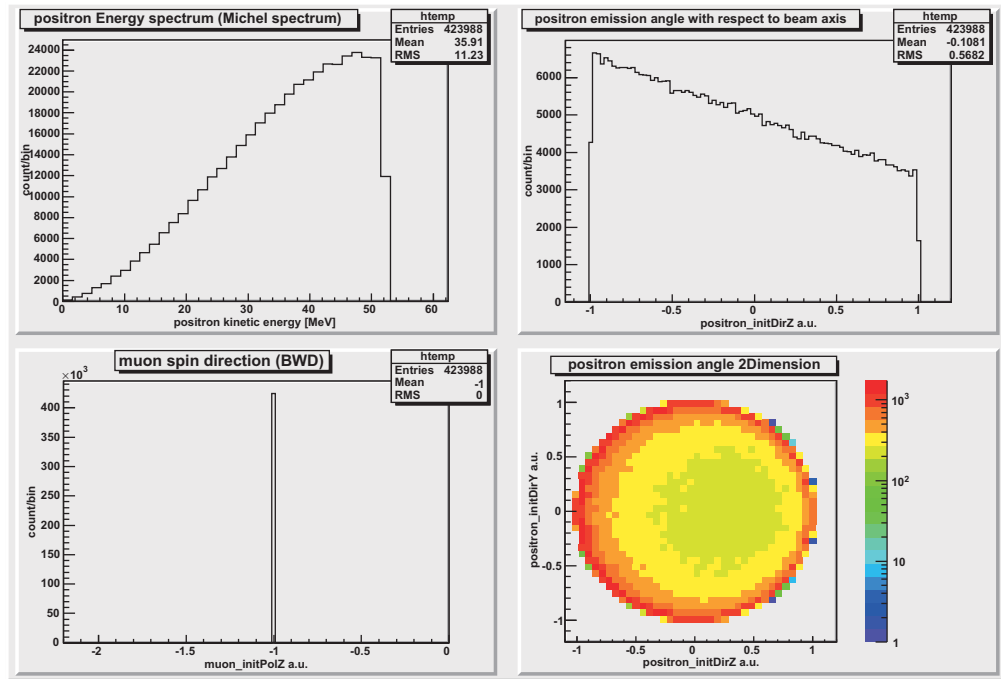


Figure 4.27: Features of the decay positron in Geant4 simulation

After some verifications were performed, the spurious asymmetry measurement was done in the same manner as our experimental conditions. The result of the simulation is shown in Fig(4.28).

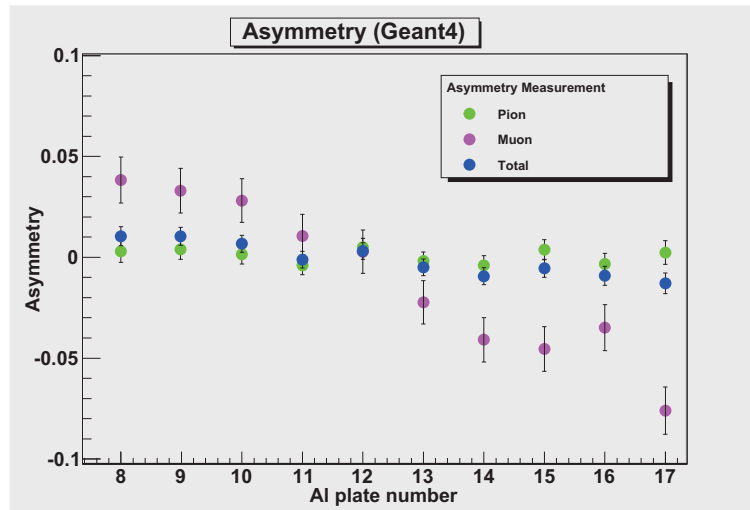


Figure 4.28: Result of the spurious asymmetry measurement in Geant4 simulation.

In this simulation, since the polarimeter did not have wires, asymmetries were defined as a layer unit, namely the "Al plate number" corresponds to the integration of the wires

in the same layer. In addition, the particles were completely identified in the simulation. It was possible to separate in-flight decay muons from pions. Here, the pink, green, and blue plots correspond to the in-flight muons, pions, and total events(muons + pions), respectively. The result of the simulation was different from the analysis of the beam test data. Although it is difficult to explain this tendency, at least the in-flight muons can cause spurious effects. Furthermore, the muons correspond to the FWD muons though beam test result tended to contain the BWD muons.

4.5.3 Summary of the asymmetry analysis

In my conclusion, this polarimeter could be very sensitive against the beam emittance. Considering the configuration of Al inner plates, stopping power of this configuration might be changed event-by-event due to the fact that the configuration was only symmetric with respect to the beam axis. In our experimental conditions, both FWD muons and BWD muons are of different momentum, 170 MeV and 85 MeV, respectively. Hence, a kind of muon (FWD/BWD) can tend to locally generate spurious asymmetry as shown in Fig(4.29).

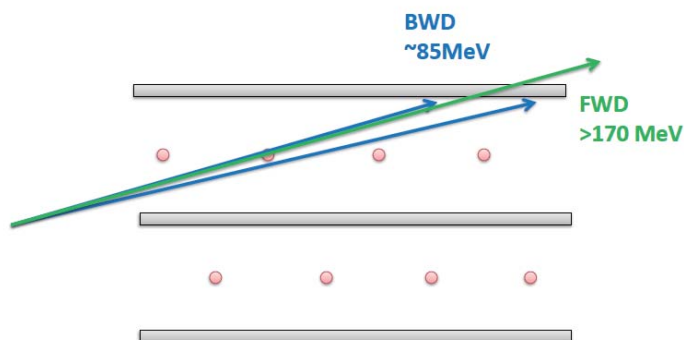


Figure 4.29: Schematic view of the cause of a spurious asymmetry.

However, we had no way to measure the beam emittance because we could not install any beam tracker. Of course there might be other reasons except for the beam emittance.

In the TREK experiment, the beam condition is different from that during the beam test. Most muons from $K_{\mu 3}$ decay spread for the full volume of the polarimeter though the muons are longitudinally polarized. Thus, it is expected that this kind of asymmetry will disappear (or get smaller).

If this kind of spurious asymmetry locally appears, this asymmetry can be canceled out based on the π^0 *fwd/bwd* scheme because the transverse axis can be determined by the π^0 direction (*fwd/bwd*) event-by-event. Hence, the polarimeter is able to measure the transverse polarization P_T precisely.

4.5.4 Future plan

We should pay attention to the followings in the next beam test for the polarimeter.

- **Beam trackers such as MWPCs**

When we try to understand the incident beam emittance, we should add more than two trackers such as MWPCs between the degrader and the S0 counter in the experimental setup shown in Fig(3.4). (Here, the degrader was placed next to the S1 counter.) Then, we will be able to roughly determine the trajectory of the incident beam particle. In other words, we can select the incident angles of the beam.

- **Configuration of the ASB cards**

We should attach a larger number of the ASB cards for the full volume as possible. If this is impossible due to our budgetary conditions, at least, we should change the configuration of the ASB cards when we take data for the spurious asymmetry test. Then, we will be able to use a larger fiducial volume for the analysis. Furthermore, we will be able to extract only the selected incident particles, namely only the beam particles parallel to the inner plates are extracted when we add more than two beam trackers. Then we can avoid the event of π decay in-flight and we can control the emittance of the incident particles. It is not until the selections above work correctly that we can start to perform the spurious asymmetry test. Last time, we did not have an enough number of the ASB cards. Although the number of the ASB cards correspond to 1/3 for the full volume, we attached the ASB cards to the both end of the polarimeter in order to take data for the charge division analysis. Suppose that the ASB cards are taken off from the one side and all the ASB cards are attached to the same end, one might worry about how to analyze the charge division analysis. The selection of the incident particles, however, is more essential than the charge division analysis when we measure the spurious asymmetry.

- **Beam profile scanning**

Last time, we could not scan the beam profile at in front of the polarimeter. Thus, we had no way to determine the center position of the beam along with the wire axis. As the result, we could not analyze charge division. Therefore, one should perform a run for the charge division. The charge division run should be performed apart from a run for the spurious asymmetry test in the next beam test for the polarimeter. Then we should scan the beam profile using a thin counter (or a MWPC) along with the wire axis in order to determine the center position of the beam. As a matter of course, the ASB cards have to be attached to the both end of the polarimeter when we can scan the profiles.

Chapter 5

Design of the Muon Tube Polarimeter

In the previous chapters, the studies of the plate type polarimeter were discussed. We also prepare a tube type polarimeter as an another possible alternative. Roughly speaking, the inner structure of the polarimeter will change from multi-plates into multi-tubes.

In the positron track reconstruction analysis, there was a difficulty caused by a rectangle cell structure. In a case of the rectangle, the shape of the equi-drift time line is very complicated. Hence, it is difficult to determine the drift velocity precisely. As a result, we have to calculate the drift velocity relying on the simulation if we pursue higher position resolution. In addition, the position resolution is limited by an emission angle of the decay positron. (see Appendix B)

On the contrary, since the tube type polarimeter has a symmetric structure, the equi-drift time line corresponds to a circle. In addition, position resolution can be free from the emission angle, the accuracy of the position determination is higher than that of the plate type. Moreover, in terms of the track reconstruction analysis, the drift velocity (or the X-T relation) should be completely determined using the experimental data. This also allows to decrease some systematics associated with an uncertainty of the calculation of the electrostatic field. This is the first reason why the tube polarimeter attracted me.

Furthermore, since the tube type does not have singular axis, we can measure the longitudinal polarization in $K_{\mu 3}$ decay based on the *fwd/bwd* scheme in the case that we can employ the tube type polarimeter. The longitudinal polarization measurement will be able to suppress some systematics in the TREK experiment. In addition, since the stopping power of the tube type does not rely on the incident angle of the muon in $K_{\mu 3}$ decay, a kind of systematics caused by a misalignment of the polarimeter can also be reduced. The main parameter comparisons with the plate type are summarized in table(5.1).

Table 5.1: Parameter comparisons of the plate type.

	Al plate	Al tube
Sense wire	SUS304 20 μm	SUS304 20 μm
Number of sense wires	~ 500 channel	371 channel
Number of potential wires	~ 500	none
The distance between sense wires	16 mm	14.2 mm
Equi-drift-time line	complicated	circle
Read-out AMP	ASB card	ASB card
Solid angle coverage for positron detection	~ 100 %	~ 100 %
Material density / full volume	24 %	24 %
Inner gas	Ar : Et = 50 : 50	Ar : Et = 50 : 50

5.1 Estimates of Muon Tube parameters

As I optimized the parameters for the muon tube, there were a few constraints and requirements as follows.

- **Size of the muon polarimeter magnet**

Considering the fact that the muon polarimeter magnet has already been manufactured and the magnetic field test has been performed, we should employ the same muon magnet which has been developed for the plate type polarimeter. This means that the full size of the new polarimeter has to be equal to the plate type. Thus, the number of tubes and the size of a tube are subject to certain restrictions.

- **Higher track efficiency**

Since the new polarimeter should also have a high track efficiency, the ratio of inner/outer diameter is limited. It is quite important to meet the condition that the ratio of the inner/outer diameter is over 87 %. Presuming that the specific condition above is satisfied, then both the incident muon and the decay positron can pass through all the gas volumes as shown in the left picture of Fig(5.1). In addition, the tubes should be aligned as dense as possible to increase the track efficiency. The track efficiency is worse in case that the tubes are not densely aligned as shown in the right picture of Fig(5.1). Furthermore, considering the positron multiple scattering, the inner density should be as low as possible. In the case that a large number of clean tracks are measured in the polarimeter, the analysis efficiency increases even if we do not employ the correction of positron scatterings. For satisfying the conditions above, the thickness of the tube should be thin and the tubes should be aligned densely.

- **High stopping power**

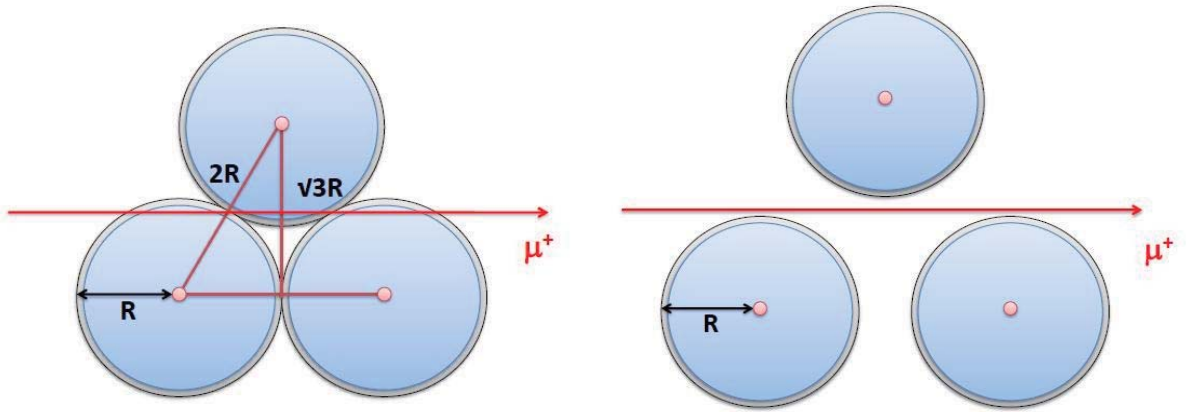


Figure 5.1: Schematic view of the constraint against the Muon Tube. The tubes are aligned densely in the left one, while the tubes in the right one are aligned with a lower packing density.

On the contrary, the incident muons should be stopped as far as possible inside the fiducial volume. Thus, the thickness of the tube walls should be as thick as possible. This requirement is in contradiction with the 2nd item.

For the requirements and constraints above, I had to optimize the best parameters of the muon tubes. For optimizing the parameters, I have done a MC simulation using Geant4. In the simulation, the muon beam generated from the full simulation for the E246 experiment was adopted, namely the muons from $K_{\mu 3}$ decay. In the beginning of the simulation, the outer diameter (named OD) was fixed from the constraint of the muon polarimeter magnet and it was equal to 14 mm. On the contrary, the inner diameter (named ID) was treated as a variable between 9.8 mm and 12.6 mm. Although more than 12.2 mm was required as the size of the ID from the requirement of high track efficiency, the size of the ID was changed to extended regions. The resulting pictures are shown in Fig(5.2 - 5.5), where ΔR corresponds to the thickness of the tube. In Fig(5.2), Many muons are stopped in the end plate of the polarimeter. On the other hand, in Fig(5.4), the muons are stopped in a narrow region though track efficiency can be quite low. In Fig(5.3) and Fig(5.5), since most of the muons are stopped in the comparatively narrow region, ΔR was finally determined to be equal to 1.2 mm.

5.2 Current status of MTP

For manufacturing the MTP, we had several meetings with the staffs of REPIC Co. Although the MTP has not yet been completed, all the parts of the MTP has been delivered to REPIC Co. and the assembling has already started.

For checking the process of Al tube manufacturing, I went to Yamakawa Manufacturing industry Co. For the MTP manufacturing, the Al material-A5052 was adopted. As men-

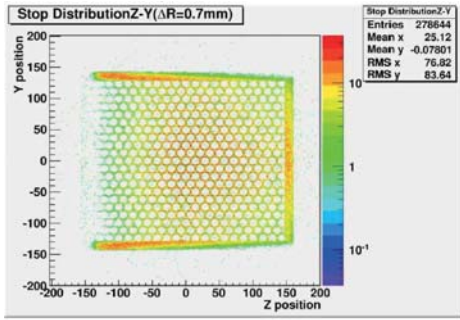


Figure 5.2: $OD : ID = 10 : 9$.

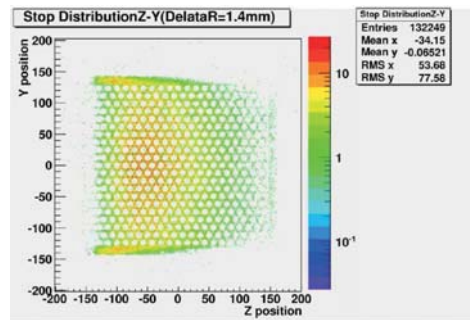


Figure 5.3: $OD : ID = 10 : 8$.

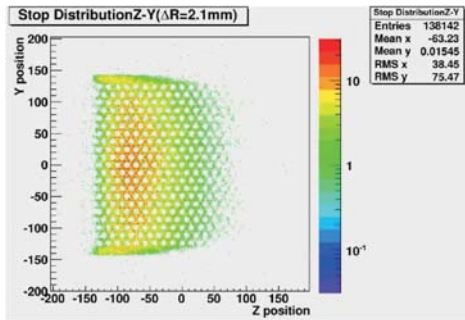


Figure 5.4: $OD : ID = 10 : 7$.

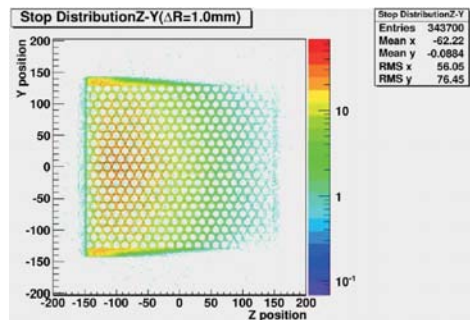


Figure 5.5: $OD : ID = 10 : 8.5$.

tioned in Chapter 2.4, A5052 is also good enough as the inner material in terms of the effect of the spin depolarization. It is essential to know the accuracy of the Al tube for optimizing the alignment of Al tubes. As the result of the tube manufacturing, the accuracy of both the outer and inner radius corresponds to $\leq 10 \mu\text{m}$ and we are successfully able to align the tubes at the intervals of 14.2 mm. The resulting tubes are shown in Fig(5.6 - 5.7)



Figure 5.6: Side view of Muon tube.



Figure 5.7: End view of Muon tube.

At the same time, the other parts are assembled as shown in Fig(5.8 - 5.13). The manufacturing process is summarized as follows.

- **Process of the Al tubes washing**

When the tubes were delivered to REPIC, the insides of Al tube were very dirty due to the lubricating oil. Hence all tubes had to be washed using the method of steam-washing after manufacturing.

- **Connection of the field guide to the Al tube**

The field guide connector, which is made of some kind of insulator, was used to eliminate any electrical contact with the Al tube.

- **Process of the Al tubes assembling**

The accuracy of the alignment of the Al tubes was determined by one of the template touching the buffer space for the chamber gases. In this process, the Al tubes were fixed using the connectors and the templates as shown in Fig(5.14).

- **Connection of feedthroughs to the end plate**

After the Al tubes assembling, the feedthroughs were attached to the end plate of the polarimeter as shown in Fig(5.16).

- **Process of stringing the wires**

Finally, the process of stringing the wires were performed. All the sense wires were strung with the same 30 g tension using a weight as shown in Fig(5.17).



Figure 5.8: Full volume.

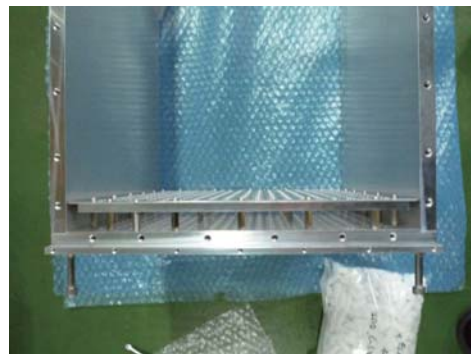


Figure 5.9: Buffer space.



Figure 5.10: Inner template.



Figure 5.11: Tube to template connector.

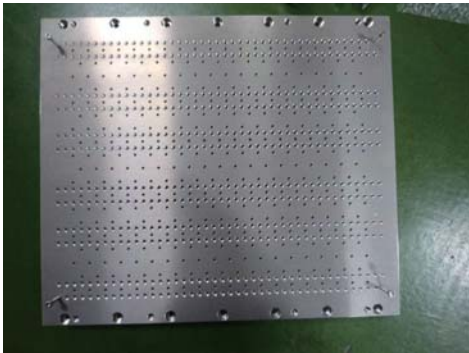


Figure 5.12: End plate.



Figure 5.13: Feedthrough.



Figure 5.14: The Al tubes assembling.



Figure 5.15: End plate connection.



Figure 5.16: Feedthroughs connection.

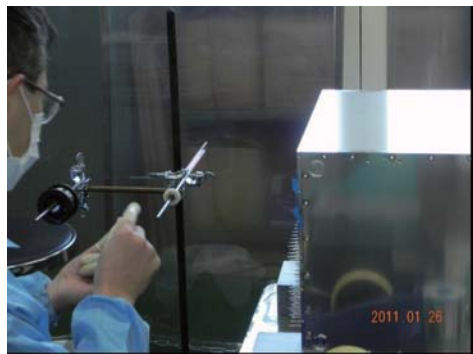


Figure 5.17: Process of the wire stringing.

Chapter 6

K1.1BR beamline for the TREK experiment

The TREK experiment will be performed at the Hadron Experimental Hall at J-PARC. At present there are 4 beam channels, K1.8, K1.8BR, KL, and K1.1BR beamline. The layout of the Hadron Experimental Hall is shown in Fig(6.1). In the TREK experiment, we will use a separated K^+ beam with 0.8 GeV/c momentum from K1.1BR. The K1.1BR beamline with a total length of 21.5 m was made as a branch beamline of K1.1, namely the K1.1BR uses the upstream magnets (from $D1$ to MS) of K1.1.

The beam optics of K1.1BR [51, 52] was designed by J.Doornbos of the TREK collaboration. In the design of the beamline, it is essential to increase the K/π ratio higher than 2 and the kaon yield as much as possible in order to satisfy the TREK requirement. Next I will describe the detector elements for the beam commissioning of K1.1BR. Finally, I will describe the current status of the beamline and the result of the beam commissioning of K1.1BR.

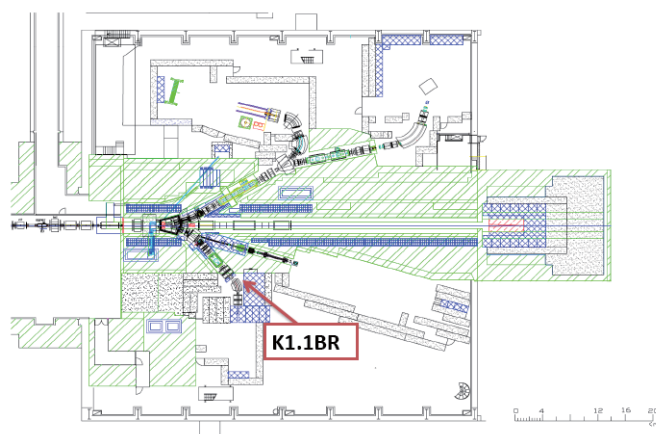


Figure 6.1: Overview of the Hadron Hall at J-PARC

6.1 Expected performance of K1.1BR

6.1.1 Design of beamline and optics

The layout of the K1.1BR beamline is given in Fig(6.2). The detector elements and the beam optics for the K1.1BR beamline are summarized in the following items.

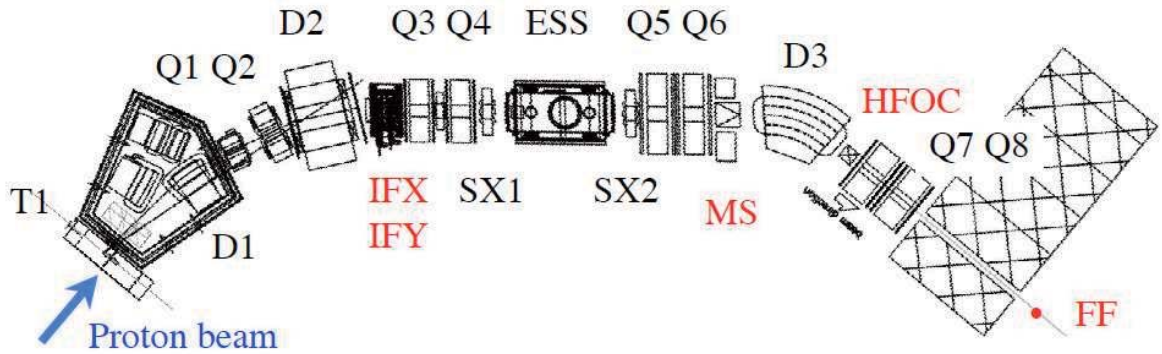


Figure 6.2: The layout of K1.1BR

- **proton target ($T1$) and first bending magnet ($D1$)**

The beam is extracted at an angle of 6 degrees to the proton beam from a 5.4 cm long Nickel production target. A 2.5 mm thick Beryllium window is placed 40 cm from the production target. The first bending magnet $D1$ which can bend up to 18 degrees is placed 2.0 m from the production target in order to avoid interference with the first bending magnets for the K1.8 and the K1.8BR beamlines.

- **quadrupole doublet $Q1-Q2$ and intermediate vertical focus (IFY)**

After $D1$, the beam passes through a set of quadrupole doublets $Q1-Q2$ that focuses the beam at the intermediate vertical focus (IFY) which is located 1.0 m downstream of the 26 degree bending magnet $D2$. A 50 μm stainless steel window is placed 15 cm downstream of IFY for vacuum control. In addition, an intermediate horizontal slit (IFX) is placed as an acceptance slit. In the K1.1BR beamline, the existence of the IFY is essential: it has a crucial role for the removal of pions. The existence of the IFY will made it possible to perform the TREK experiment in spite of having only

a single electrostatic separator (*ESS*). I will summarize the pion contamination as a background in the next subsection.

- **quadrupole doublet *Q3-Q4* and the electrostatic separator (*ESS*)**

A second doublet *Q3-Q4* makes the beam vertically parallel in the *ESS* and contains the beam horizontally. The *ESS* is one of the key elements of the beamline; it generates a transverse electric field along the beam axis and works with a correction magnet (*CM*) to separate particles by their mass difference. However, an old *ESS* from the KEK-PS is being reused due to budgetary constraints. Eventually it will be necessary to increase the length of the *ESS* to 2.5 m from the current length of the 2.0 m. Then the performance of the K/π ratio will be good enough for the TREK experiment.

- **quadrupole doublet *Q5-Q6* and mass slit (*MS*)**

A third quadrupole doublet *Q5* and *Q6* makes a vertical focus at the position of the *MS*. At the *MS*, a vertical slit can remove most of the background pions which are spread out vertically and horizontally.

- **The final bending magnet (*D3*)**

The final bending magnet *D3* with a bend angle of 40 degrees, is placed after the *MS* and the beam is bent toward a final doublet *Q7-Q8*. In the optics design, although a bend angle of 45 degrees was proposed, the current reused *D3* can only bend to 40 degrees.

- **quadrupole doublet *Q7-Q8* and horizontal focus (*HFOC*)**

A horizontal focus *HFOC* is produced after the *D3* magnet. Before the *HFOC*, the beamline still contains pions horizontally. Thus, this slit is crucial for the removal of pions and muons. A final doublet *Q7-Q8* focuses the beam at the final focus (FF), 3.3 m downstream from the end of *Q8*.

- **sextupole magnets (*SX1* and *SX2*) and octupole magnets (*O1*)**

The beamline contains two sextupoles just before and just after the separator. In addition, an octupole is placed between *Q3* and *Q4*. Although the corrections of the vertical aberrations at the *MS* are not perfect, they are sufficient to obtain a clean kaon beam.

The beam envelop of the current K1.1BR together with the various slits are shown in Fig(6.3 - 6.6).

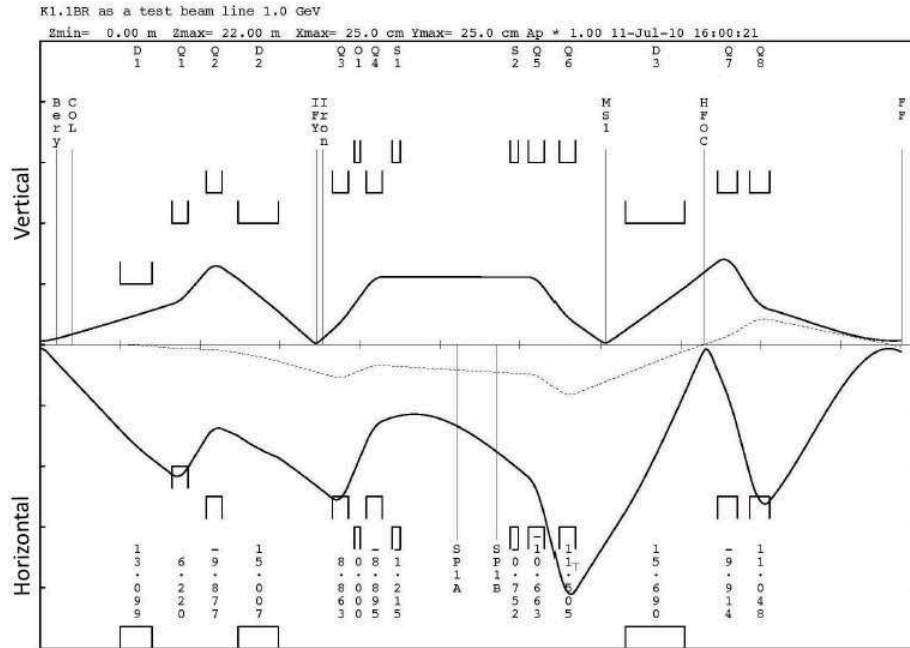


Figure 6.3: Beam envelop of the current K1.1BR beamline. The top half and the bottom half corresponds to vertical and horizontal envelop, respectively.



Figure 6.4: Picture of the intermediate focusing slits ($IFX + IFY$) and the mass slit (MS) before installation. Both slits are located at the vertical focusing point. The IFY , in particular, has a crucial role for the removal of pions in spite of the use of a single stage separator. In addition, IFX is useful to control the overall beam acceptance.



Figure 6.5: Picture of the horizontal focusing slit (*HFOC*) before installation. The *HFOC* is placed before the final doublet $Q7 - Q8$ and is also useful for the removal of the pion contamination in the beam.



Figure 6.6: Picture of the electrostatic separator (*ESS*) before installation. The *ESS* is one of the essential elements for the beamline to extract a clean K^+ beam.

6.1.2 Pion contamination

There are three sources of pion contamination. The sources and the method of their removal are summarized below.

- **Higher order aberration**

The direct pions produced in the production target can pass through the *MS* due to higher order aberrations. The direct pion contamination can be corrected by both *SX1* and *SX2* which are located just before and after the *ESS*. In addition, the singlet *O1* located between $Q3$ and $Q4$ is also useful.

- **Slit scattering**

Suppose that the aperture of the *MS* is narrow, the K/π ratio will not be good enough due to the scattering at the *MS*. Furthermore, in the case that the *IFY* is also a narrow aperture, the K/π ratio will be much worse. Then the horizontal slit *HFOC* can help to improve the K/π ratio. The removal of slit scattering pions is performed by a narrow horizontal aperture condition of the *HFOC*.

- **Cloud pions from K_s ($c\tau = 2.7$ cm)**

Cloud pions are generated from the region near the production target. The scattering in a $50\ \mu\text{m}$ stainless steel window, placed 15 cm downstream from the *IFY* for managing the vacuum conditions, can cause a large beam spot (vertically and horizontally) at the *MS*. In a single stage of the *ESS*, the removal of the pions has to be performed using a vertical focus in the beginning of the beamline before the separator, thus the *IFY* is essential for the beamline. Since a slit is placed at the *IFY*, it can be used to limit the cloud pion contamination. The *IFY* slit can bring the cloud pion fraction down to an acceptable level. However, the pions can be still contained at the *MS*, then the *HFOC* is also helpful to reduce the contamination in the beamline by selecting the narrow aperture.

6.1.3 Expected Kaon yield

The beamline and optics were designed for high K/π ratio and high kaon yield. As the result of trial and error, the best optical conditions were optimized by J.Doornbos for the TREK experiment.

The expected performance of the kaon yield is evaluated as the comparison with a similar low momentum beamline LESB3 at BNL-AGS. Its well-established kaon beam intensity at 0.8 GeV/c but with 24 GeV proton energy converts to about 80 k K^+ /spill for the current K1.1BR condition assuming a Ni target.

We can also compared the kaon yield for the current K1.1BR with the Sanford-Wang empirical formula [53]. From the result of this formula, 65 k K^+ /spill will be expected for the current K1.1BR. The accuracy of both comparisons, however, is of course limited by the ambiguity of slit openings and the kind of production target.

6.2 Detectors for the beamline commissioning

In the beam commissioning run, the detectors (Beam Hodoscope, MWPCs, Fitch-type Cherenkov counter, beam defining counter (BDC), TOF counters, and Gas Cherenkov counter) were all located downstream of the radiation shielding, which had a 2.5 m thickness, as shown in Fig(6.7).

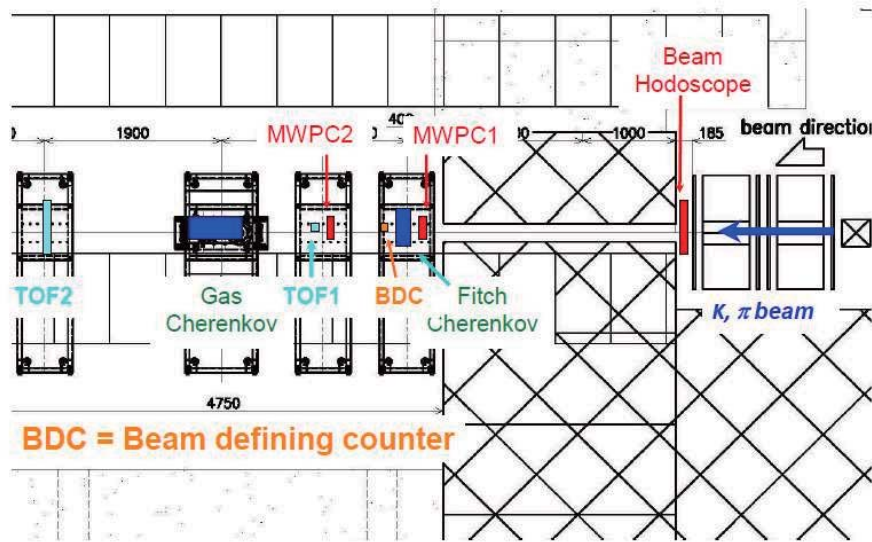


Figure 6.7: Detector components for the beam tuning.

6.2.1 beam detector elements

After the final focusing magnet $Q8$, the beam passes through the Fitch-type differential Cherenkov counter first. Both pions and kaons can be confirmed by the Cherenkov. After the Cherenkov, the beam passes through the BDC counter, which is one of the trigger counter, located at the final focusing point (FF). The FF is 3.3 m downstream from the exit of $Q8$. The beam trigger is made of the coincidence of both the BDC and TOF1. In our configuration of detectors, it is possible to measure the time-of-flight for all kinds of particles using a flight length of nearly 4 m. Indeed, the performance of the Fitch Cherenkov was confirmed by using the TOF system. The TOF spectrum and the performance of this system is shown in the next section. We also prepared the MWPCs and Beam Hodoscope counter. Therefore, the beam profiles can be measured at the FF and the end of the shielding by the MWPCs and at the end of $Q8$ by the Beam Hodoscope. The final beam profiles are also shown in the next section. In addition, a Gas Cherenkov counter was also prepared. Since this counter was filled with some air at a pressure of 1 atm, the Cherenkov light can be emitted with some incident angle in the case of the electrons entering into the detector, therefore the detector can be used as electron veto. The performance of these detectors were tested at KEK-PS North Hall at KEK and at Hadron Experimental Hall at J-PARC. As shown in Fig(6.8), all detectors were finally installed in our beam channel.

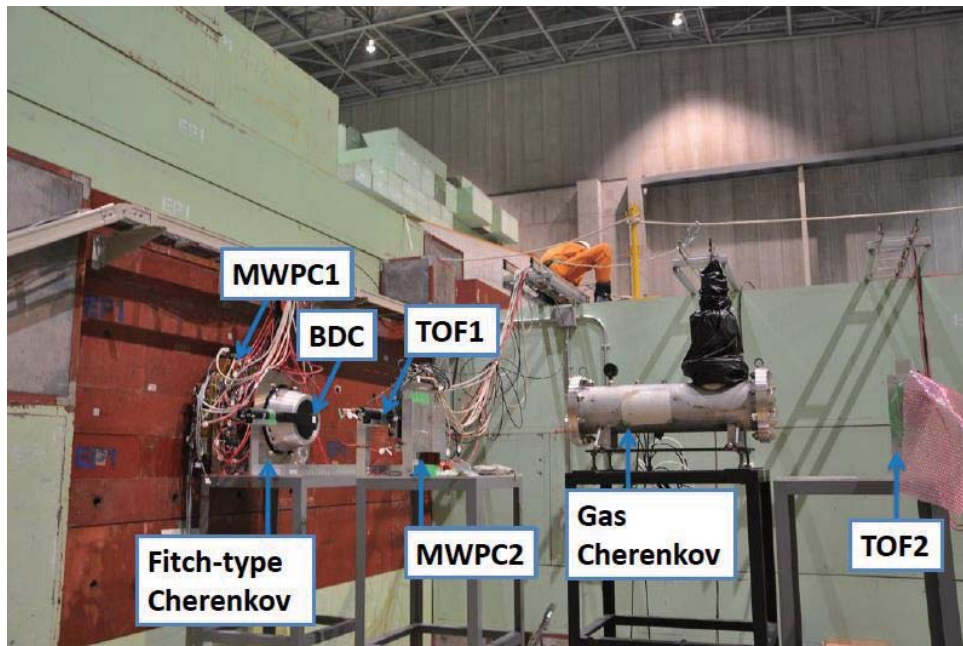


Figure 6.8: Detector elements for the beamline commissioning.

The Beam Hodoscope, however, cannot be seen in the figure above due to the fact that it was located between the shielding and the $Q8$ magnet. The structure of the Hodoscope is shown in Fig(6.9). As can be seen in the figure, the Hodoscope is simply composed of 24 scintillators with a thickness of 12 mm.



Figure 6.9: Picture of the beam Hodoscope. The Hodoscope is composed of 24 scintillators with a thickness of 12 mm in a stainless steel frame.

6.2.2 Fitch-type differential Cherenkov counter

In order to trigger on both the kaons and the pions in the beam, a Fitch-type differential Cherenkov counter was prepared. In the beginning, this counter was developed for the E246 experiment [54]. After the stop of E246, several improvements were added to the counter due to the different beam momentum of the E246 experiment [55]. The structure of this counter is as shown in Fig(6.11) and the parameters are also given in Table(6.1). The kaons and pions enter into an acrylic radiator with a 40 mm thickness and the Cherenkov light is finally emitted with a characteristic polar angle according to each velocity. The light is totally reflected at the rear surface of the radiator and detected by an inner photomultiplier(PMT) ring (π ring). The light from the kaons emerging from the radiator is reflected by a backward parabolic mirror and detected by an outer PMT ring (K ring). Each ring is composed of 14 PMTs with a Winston cone at the entrance. The designed momentum range is 740-800 MeV/c. The trigger condition is evaluated as the multiplicity of the PMT hit by Monte Carlo simulation as shown in Fig(6.12 - 6.13). From the results of the simulation, when a threshold multiplicity of $N > 6$ is required, more than 99 % trigger efficiency for kaons can be expected with negligible misidentification as pions. In addition, when a threshold multiplicity of $N > 4$ is required, ~ 100 % trigger efficiency for pions can be also expected with a negligible kaon misidentification.

Table 6.1: Main parameters of the beam Cherenkov counter. The K^+ momentum is expected to be 740-800 MeV/c. The K^+ efficiency is obtained to be higher than 99 % by setting the threshold multiplicity of $N > 6$.

Parameter	Value
Accepted K^+	740-800 MeV/c
Radiator material	acrylic ($n_D = 1.49$)
Effective aperture	12 cm diameter
Number of PMTs	14 for K^+ and 14 for π^+
K^+ efficiency	$> 99\%$
π^+ misidentification as K^+	$< 1\%$



Figure 6.10: Top view of the beam Cherenkov counter.

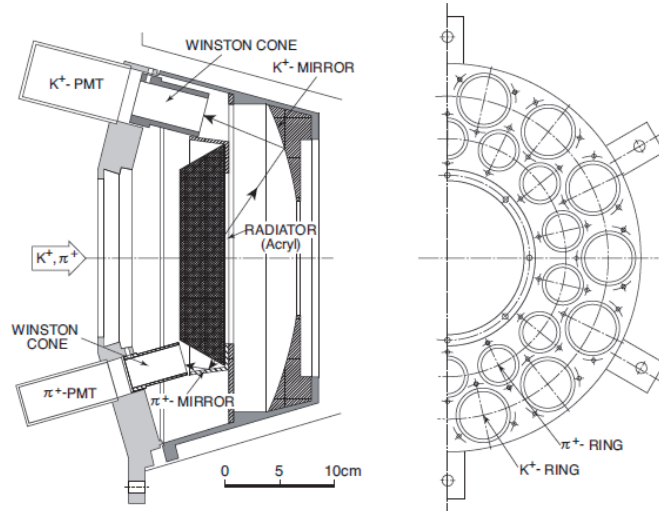


Figure 6.11: Side view and end view of the beam Cherenkov counter. The beam with 740-800 MeV/c momentum emits Cherenkov light with an angle of 38° for K^+ and 47° for π^+ . The critical angle of the radiator for total reflection is 42.2° .

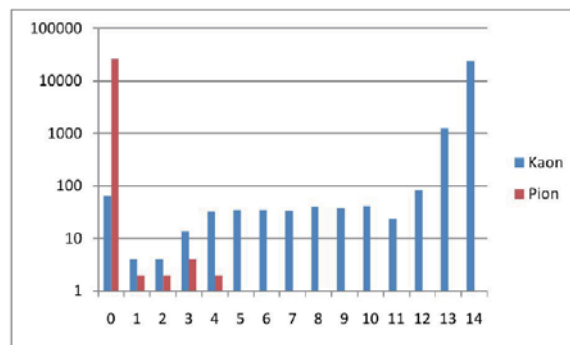


Figure 6.12: Distribution of PMT-hit K ring multiplicity @ 770 MeV/c in Monte Carlo simulation.

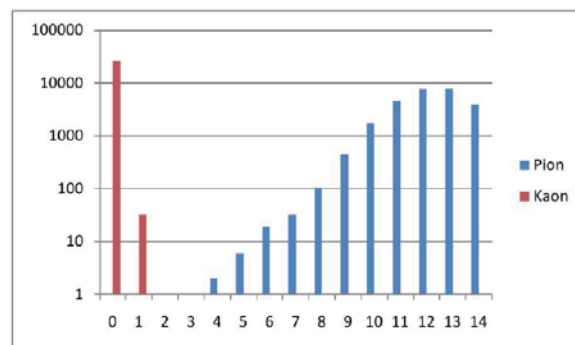


Figure 6.13: Distribution of PMT-hit π ring multiplicity @ 770 MeV/c in Monte Carlo simulation.

6.3 Commissioning of the beamline

The current K1.1BR beamline has been constructed slightly different than the original optics design. The different points are the followings:

- The length of *ESS* is not 2.5 m as in the optics design, but 2.0 m, because an old *ESS* from KEK-PS has been reused. As a matter of fact, this is disadvantageous for the K/ π separation.
- The bending angle of the last dipole magnet (*D3*) is not 45 degrees as in the optics design but only 40 degrees due to performance limit of the reused *D3*. This might increase the pion contamination compared with the larger bend angle.
- The final focus (FF) is currently 3.3 m distance from the last focusing element *Q8*, due to the 2.5 m thick Fe shielding as required by the radiation safety group during the test beam period. This will be shortened to 0.8 m for the TREK experiment.

6.3.1 Result of the beam tuning

The commissioning of the K1.1BR beamline was performed in Oct-Nov 2010. The TREK collaboration was responsible for the beam commissioning. The 0.8 GeV beam momentum at an accelerator power of 3 kW on average on a P_t production target was adopted for the beam tuning.

In the beginning of the beam tuning, we searched for kaons using a TOF system. Then, we confirmed the time-of-flight for particles corresponding to pions, kaons, and protons. The first observation of kaons from the K1.1BR beamline is shown in Fig(6.16). For confirming whether the kaon-like peak is consistent with the real kaons or not, the conditions that the π ring and K ring PMT hit multiplicity are zero hit and more than 1 hit, respectively, were required. Finally, we could verify the fact that the TOF spectrum did not depend on the requirement above. (I have also done the simple calculation using the β factor and the flight length; the calculation was also consistent with the TOF spectrum.) In this step, the pion peak, however, was higher than kaon peak due to the three reasons below.

- The Fitch Cherenkov detector has not been tuned yet.
- The beamline magnets has not been sufficiently tuned yet.
- The *ESS* operation voltage was lower than its maximum voltage ($\sim \pm 400$ kV).

For extracting the maximum performance of the beamline, we tuned the Fitch Cherenkov detector first.

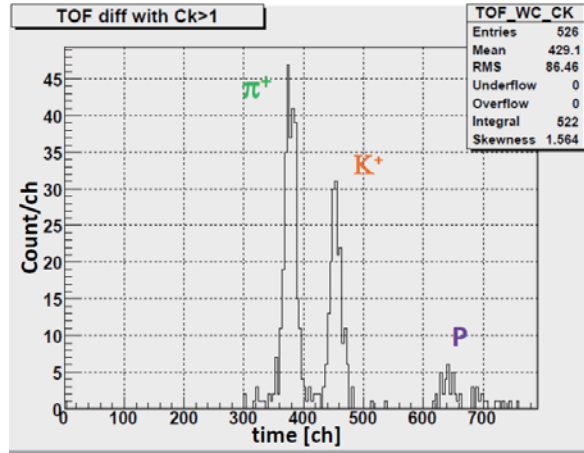


Figure 6.14: TOF spectrum. A large number of kaons were observed in the separated beam. We also see pions and protons in the spectrum. In this figure, the conditions that the π ring and K ring PMT hit multiplicity are equal to zero hit and more than 1 hit, were required, respectively.

After the confirmation of the particle timing, the performance of the Fitch Cherenkov counter was confirmed using the unseparated beam. As shown in Fig(6.15 - 6.17), it is no exaggeration to say that the performance of the detector is even better than the results of the simulation in Fig(6.12 - 6.13); the π^+ misidentification as K^+ is less than 0.3 %. Finally, the threshold multiplicity was determined to be equal to $N > 6$ for K ring and $N > 4$ for π ring.

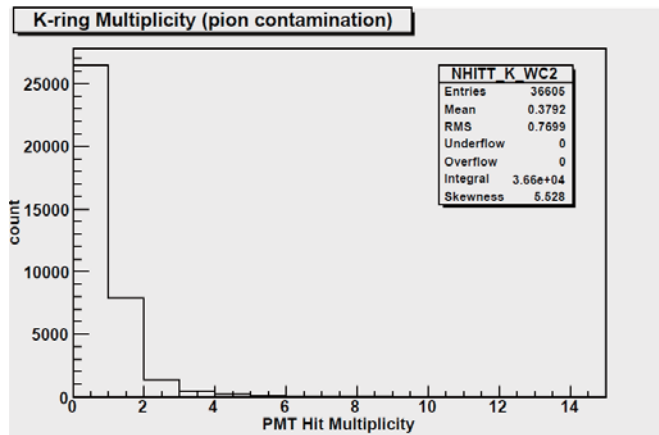


Figure 6.15: The performance of the K ring. In this spectrum, the condition of the pion timing confirmed by the TOF spectrum above is required. Thus, the figure shows the pion fraction in the K ring.

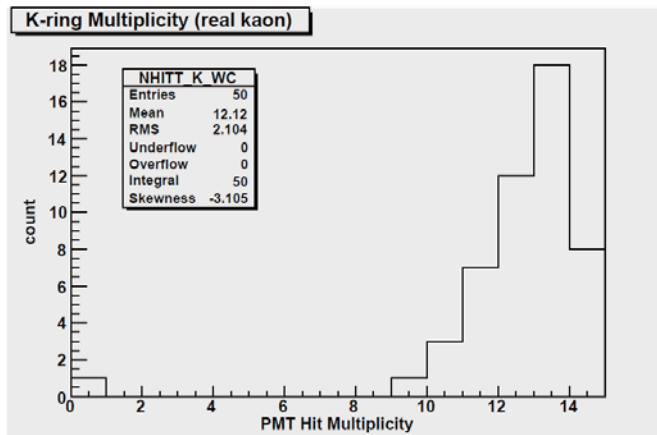


Figure 6.16: The performance of the K ring. In this spectrum, the condition of the kaon timing confirmed by the TOF spectrum above is required. Thus, the figure shows the real kaon events.

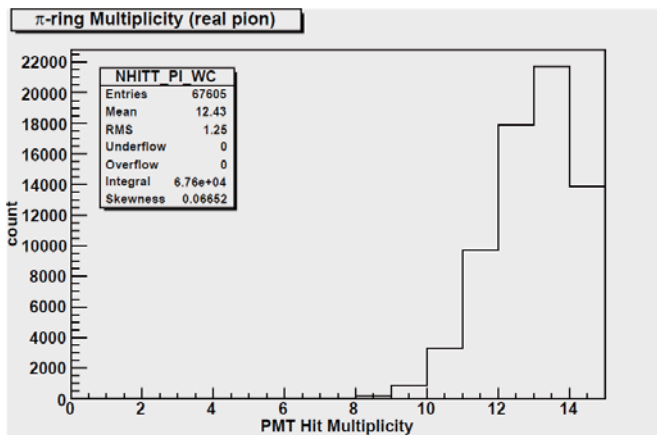


Figure 6.17: The performance of the π ring. In this spectrum, the condition of the pion timing confirmed by the TOF spectrum above is required. Thus, the figure shows the real pion events.

The beam survey and the tuning were mostly done using narrow horizontal slit (*IFX* and *HFOC*) conditions to avoid counter performance degradation where the *IFX* played the role of an acceptance slit not as a focus point. The full intensity was deduced using a scaling factor obtained from very narrow vertical slit (*MS* and *IFY*) conditions. The *ESS* was excited to ± 150 kV for rough tuning and then raised to ± 250 kV or ± 300 kV for final confirmation of the K/ π separation. The separation curve was measured by sweeping the *CM* current and finally plotting π^+ and K^+ yields triggered by the Fitch Cherenkov detector. Furthermore the proton yield was also measured as the triggered events above

the K^+ peak. The measured kaon yield and the K/π ratio are summarized for various slit conditions in Table(6.2).

Table 6.2: Results of the K^+ beam tuning at 0.8 GeV/c at K1.1BR.

Vertical slit	K^+ / spill @ 3.6 kW		π/K ratio	
	Narrow H.S.	Wide H.S.	± 250 kV	± 300 kV
Narrow ($IFY:\pm 0.5$ mm, $MS:\pm 0.75$ mm)	1253	3629	1.4	
Standard ($IFY:\pm 1.5$ mm, $MS:\pm 2.0$ mm)	2541	≥ 58443	9.8	1.1
Wide ($IFY:\pm 2.0$ mm, $MS:\pm 2.5$ mm)	3493	≥ 80338	25.2	
Widest ($IFY:\pm 2.5$ mm, $MS:\pm 2.5$ mm)	3811	≥ 87653	26.8	6

The wide horizontal slit (H.S.) settings, which are relevant to the TREK experimental condition, have some ambiguity due to the uncertainty of the scaling factors. However, the given values are lower limits, which should not be very different from the real values. In the standard vertical slit settings, we observed nearly 60 k K^+ /spill at 3.6 kW power with 6 sec repetition. As shown in the separation curve of Fig(6.18), we achieved considerably good separation with a π/K ratio of 1.1 on the kaon peak at the ESS operation of ± 300 kV.

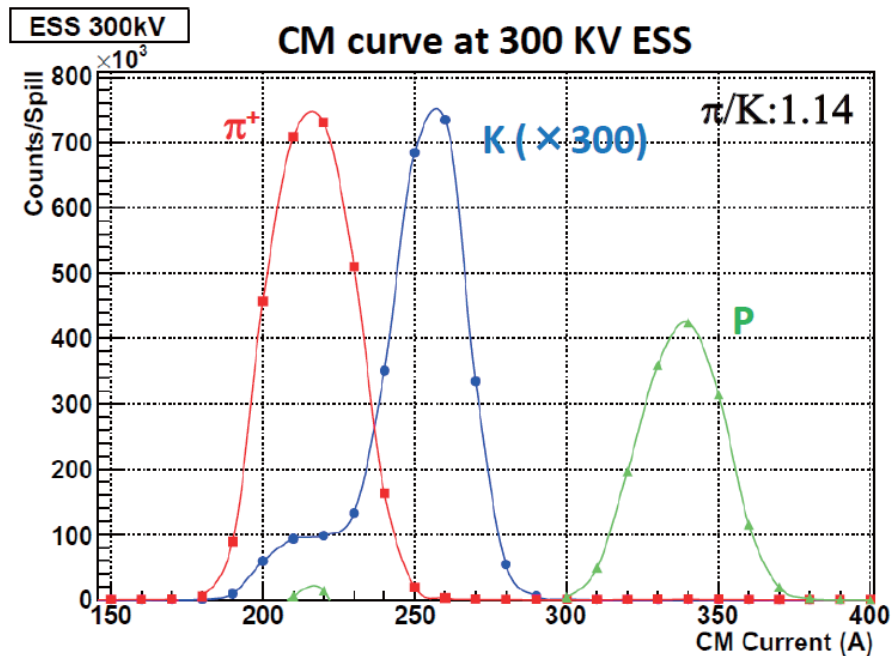


Figure 6.18: Mass separation curve obtained with a ESS voltage of ± 300 kV at the beam momentum of 0.8 GeV/c.

From the figure of Fig(6.18), one can see the kaon fraction in the pion peak. This fraction shows that the pion misidentification as kaons in the K rings and the misidentification corresponds to $< 0.03 \%$.

In the beam tuning, we also tried to find optimum focusing condition at the FF (although it will be different from the closer FF without the 2.5 m shielding), by varying the last focusing magnets $Q7$ and $Q8$. We finally succeeded to focus the kaon beam to a round spot with $\sigma_{x,y} = 11$ mm as shown in Fig(6.19).

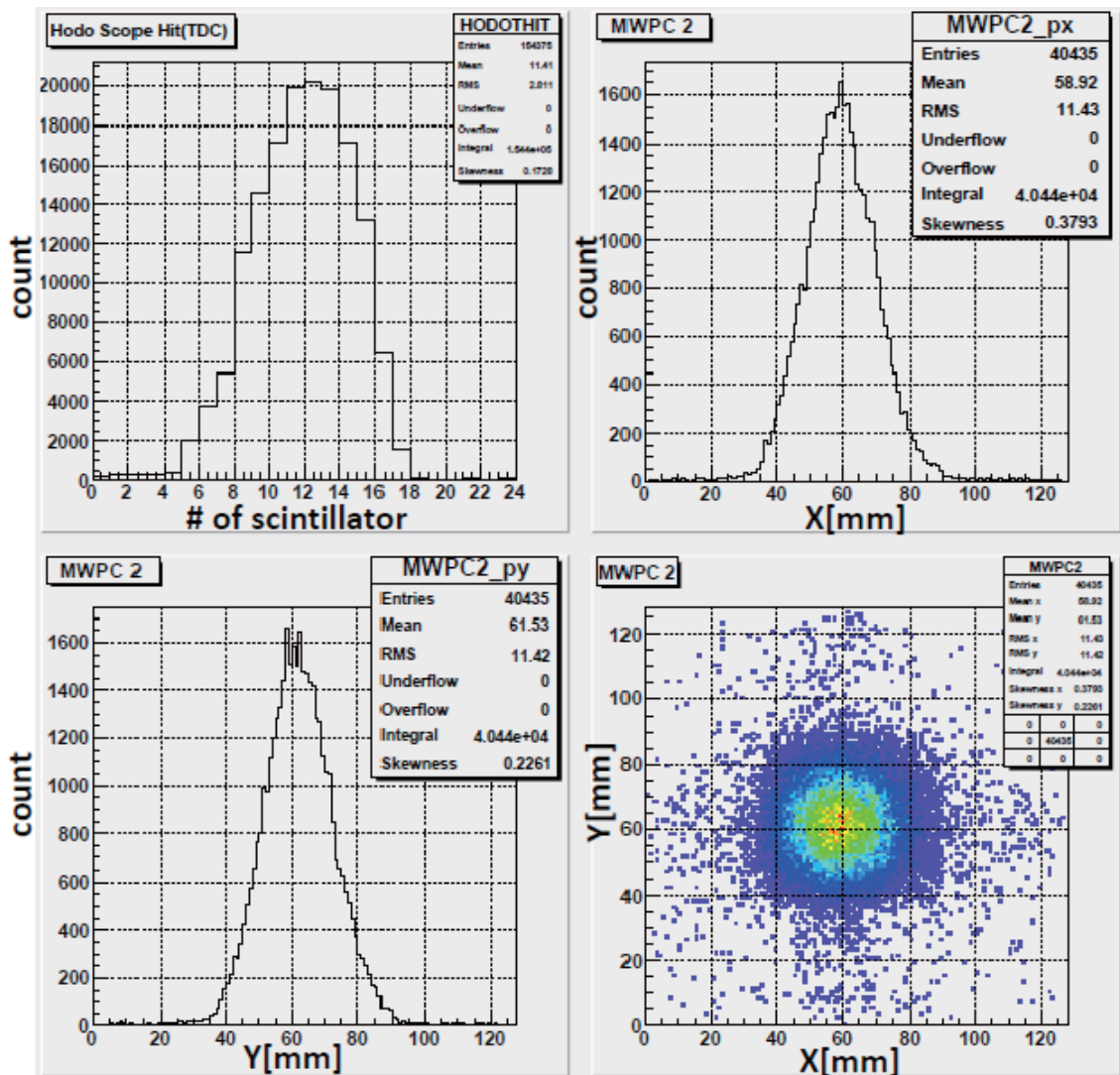


Figure 6.19: Kaon beam spot at the FF for the best tuning setting of $Q7$ and $Q8$, and at the end of $Q8$ using a beam Hodoscope.

Conclusion

In this thesis, the following items regarding the polarimeters for the TREK experiment are discussed.

1) At present we have two choices as the polarimeter. One is a plate type and the other a tube type. For the plate type, I took part in from the process of the manufacturing and the beam test at TRIUMF. The analysis based on the beam test was done on my responsibility.

2) In the track reconstruction analysis, I developed a track reconstruction algorithm based on my idea. As the result, a simple track algorithm using the X-T relation optimized by the experimental data was developed though still some kinds of problems I described in Chapter 4.

3) In the null asymmetry analysis, a spurious asymmetry, which is generated from the polarimeter mechanical structure, appeared. I think that muons from the pion decay in-flight can be possible to cause the spurious asymmetry, in other words, the emittance of the incident particle beam can locally make the asymmetry. Further studies for understanding the spurious effects are essential in order to complete an active polarimeter. I suggested the new experimental condition for avoiding the effect of decay in-flight in Chapter 4.

4) At present the manufacturing of the tube type polarimeter is in progress under my supervision. Since the cell of the tube type has a structure of circular symmetry, the equi-drift time line completely corresponds to a circle. Hence, the position resolution can be free from the emission angle of the decay positron. As the result, a higher accuracy of the position determination will be expected. Furthermore, some systematics in the TREK experiment will be able to be reduced.

In addition, I described the commissioning of K1.1BR beamline, where 60 k K^+ /spill was obtained. In order to start the TREK experiment, it is essential to make some improvements to the beamline. First, we should install a 2.5 m *ESS*, then the π/K ratio will be down to 0.5. If we change the current *D3* into a new *D3* with a bending angle of 45 degrees, we will obtain a π/K ratio smaller than 0.5. Furthermore, we should shorten the distance to the FF, then the value of the kaon yield will increase up to 90 k K^+ / spill, which also satisfies the TREK requirement.

Appendix A

Charge division

Here, the mechanism of the charge division method will be described briefly. As shown in Fig(A.1), the distances between particle hit position and the wire ends are defined as Z_1 and Z_2 , and the resistances corresponding to the distances are defined as R_1 and R_2 , respectively. In addition to these wire resistances we have to consider the input impedance of amplifiers, which are defined as r_1 and r_2 , respectively. In this case, the equivalent circuit can be expressed as shown in Fig(A.2). The collected charge on the virtual capacitance is

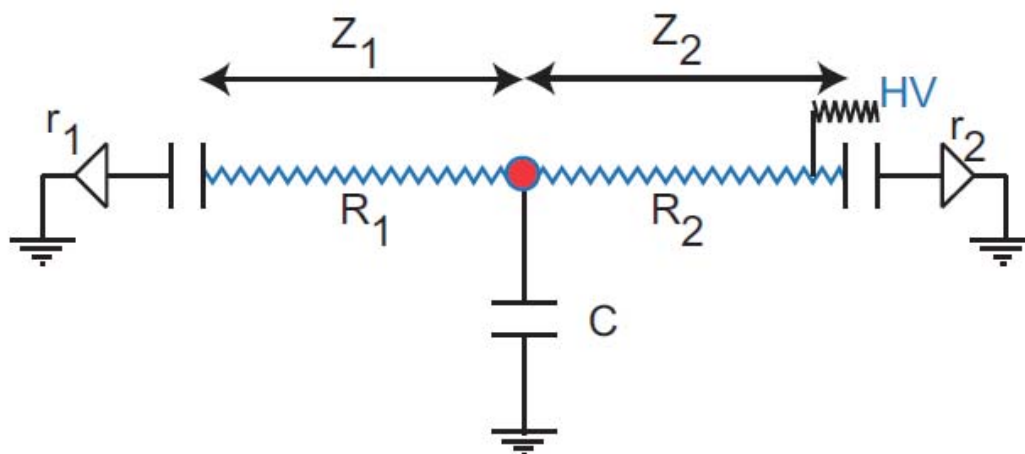


Figure A.1: The schematic view of charge division system. The distance from avalanche to wire ends are Z_1 and Z_2 , and the corresponding resistances of the wire are R_1 and R_2 , respectively. The input impedance of amplifiers are r_1 and r_2 .

discharged through the resistances. The experimentally time-integrated I_1 and I_2 currents are observed as the charges Q_1 and Q_2 , respectively. Using the capacitance (C) and voltage (V), the charge (Q) can be written as,

$$V = I_1(R_1 + r_1) = I_2(R_2 + r_2), \quad (\text{A.1})$$

$$Q = \int (-I)dt = CV, -I = -(I_1 + I_2) = C \frac{dV}{dt}, \quad (\text{A.2})$$

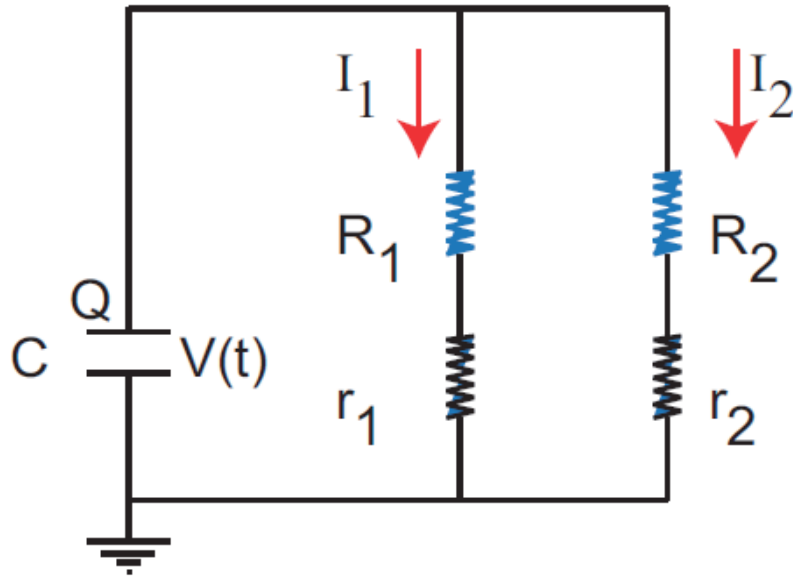


Figure A.2: Equivalent electric circuit of the charge division system. The collected charge on capacitor is discharged through resistances. The experimentally time-integrated I_1 and I_2 are observed as the charges Q_1 and Q_2 .

thus

$$C \frac{dV}{dt} = -\frac{V}{R_1 + r_1} - \frac{V}{R_2 + r_2} = -\left(\frac{1}{R_1 + r_1} + \frac{1}{R_2 + r_2}\right)V, \quad (\text{A.3})$$

$$V = -\frac{(R_1 + r_1)(R_2 + r_2)}{R_1 + R_2 + r_1 + r_2} C \frac{dV}{dt} = -\tau \frac{dV}{dt}$$

V can be obtained as $V(t) = V(0)\exp(-t/\tau)$, and

$$I_1 = \frac{1}{R_1 + r_1} \frac{Q}{C} \exp(-t/\tau) \text{ and } I_2 = \frac{1}{R_2 + r_2} \frac{Q}{C} \exp(-t/\tau). \quad (\text{A.4})$$

The charges from both wire ends are obtained by time-integration of I_1 and I_2 as

$$Q_1 = \int (-I_1) dt = \frac{1}{R_1 + r_1} \frac{Q}{C} \tau = \frac{R_2 + r_2}{R_1 + R_2 + r_1 + r_2} Q, \quad (\text{A.5})$$

$$Q_2 = \int (-I_2) dt = \frac{1}{R_2 + r_2} \frac{Q}{C} \tau = \frac{R_1 + r_1}{R_1 + R_2 + r_1 + r_2} Q.$$

From the relation of

$$\frac{Z_1}{Z_2} = \frac{R_1}{R_2}, \quad (\text{A.6})$$

Q_1/Q can be described by using $Q = Q_1 + Q_2$, $R = R_1 + R_2$, and $Z = Z_1 + Z_2$ as,

$$\frac{Q_1}{Q} = \frac{R_2 + r_2}{R_1 + R_2 + r_1 + r_2} = \frac{R_2/R + r_2/R}{1 + (r_1 + r_2)/R} = \frac{Z_2/Z + r_2/R}{1 + (r_1 + r_2)/R}. \quad (\text{A.7})$$

Therefore, from Eq(A.7) the particle hit positions can be determined by the output charges from both wire ends as,

$$\frac{Z_2}{Z} = \left(1 + \frac{r_1 + r_2}{R}\right) \frac{Q_1}{Q} - \frac{r_2}{R},$$

$$\frac{Z_1}{Z} = 1 - \frac{Z_2}{Z} = \left(1 + \frac{r_1 + r_2}{R}\right) \frac{Q_2}{Q} - \frac{r_1}{R}, \quad (\text{A.8})$$

$$\frac{Z_1 - Z_2}{Z} = \left(1 + \frac{r_1 + r_2}{R}\right) \frac{Q_2 - Q_1}{Q} - \frac{r_1 - r_2}{R}.$$

In the coordinates where x is the distance of the particle hit position from the center ($x = 0$ is center), x is written as,

$$\frac{x}{Z} = \left(1 + \frac{r_1 + r_2}{R}\right) \frac{Q_2 - Q_1}{2Q} - \frac{r_1 - r_2}{2R}, \quad (\text{A.9})$$

where $Z_1 - Z_2 = 2x$. The Eq(A.9) is the same as Eq(3.6).

Appendix B

An estimate of X-T relation

For determining the X-T relation, first of all, an estimate of the typical drift velocity is needed as an initial parameter. In order to estimate the parameter, the incident beam data were useful because we have the known start timings (t_0) determined by the S1 counter. In addition, the trigger condition in the analysis was as follows,

- 1) in order to extract only the incident particles, less than 200 ns data from the S1 signals were adopted,
- 2) the condition that all continuous 5 wires were hit and thus forming a straight line was required.

As the trigger, any selected 5 wire sets were used. The spectrum, as shown in Fig(B.1), consisted of the sum of all the central wire hit timings.

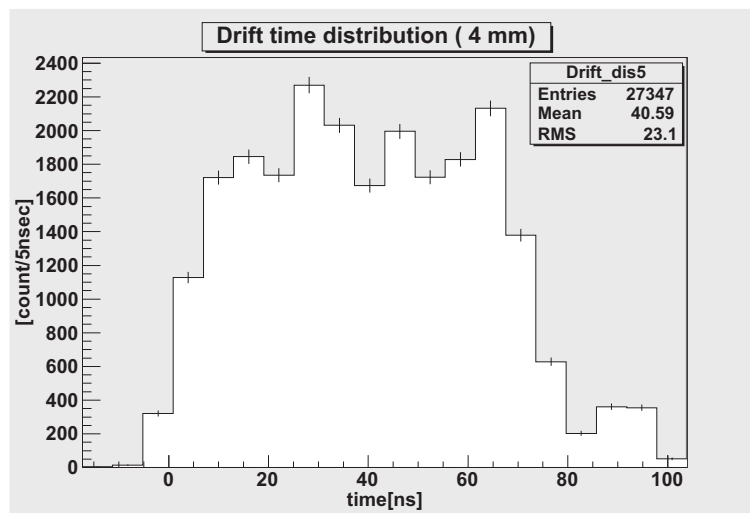


Figure B.1: Drift time distribution. The sweep of the drift time distribution corresponded to a cell size.

In general, the time width was determined by both the cell size and the drift velocity. In this case, since the cell size has already been fixed as 4 mm, the only parameter was the drift velocity. From the distribution, the 80 ns time width corresponds to roughly $50 \mu\text{m}/\text{ns}$. The drift velocity is generally determined by the kind of gas and its pressure. The

resulting velocity from the experimental data was roughly consistent with the estimation from the gas condition.

B.1 Determination of the X-T relation

Next I will explain the algorithm for determining the X-T relation. Indeed, as the only data that we could use for analysis were each wire hit timings, the other parameters must be extracted from them. The 3 wires which meet the same configuration as Fig(B.2) were chosen for the full volume.

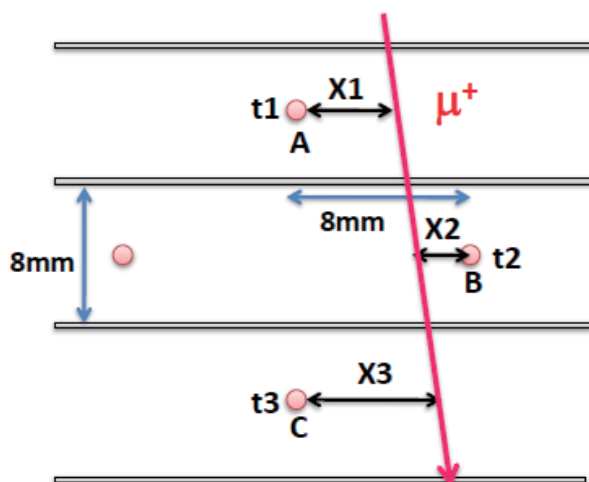


Figure B.2: Schematic view of the definition of wires for analyzing the X-T relation. The same configuration of wires was adopted in my analysis.

Here, I define the wires as A, B, and C and the wire hit timing as t_1 , t_2 , and t_3 , respectively as shown in Fig(B.2). In this analysis, the muon beam was adopted due to the two reasons given below.

- time zero
As well as the estimate of the drift velocity, we already know the start timing due to the S1 counter. In this case, the timing just corresponds to t_0 .
- stagger structure
For evaluating the X-T relation, the incident particle must have passed between A (or C) and B, then the simple relation given below could be ensured,

$$X2 = 8 - (X1(t_1) + X3(t_3))/2. \quad (\text{B.1})$$

Eq(B.1) is essential for my analysis. Here, I must give an account of the explanation above in detail. Suppose that both X1 and X3 are linear functions of t_1 and t_3 , respectively such as $X1 = v(t_1 - t_0)$, then X2 is calculated using Eq(B.1). Here, the fact is essential

that the X2 is evaluated without using t_2 . In other words, both X2 and t_2 are evaluated independently. A 2-Dimensional graph of X2 and t_2 using the assumed drift velocity as an initial parameter, namely $v = 50 \mu\text{m/ns}$, is shown in Fig(B.3).

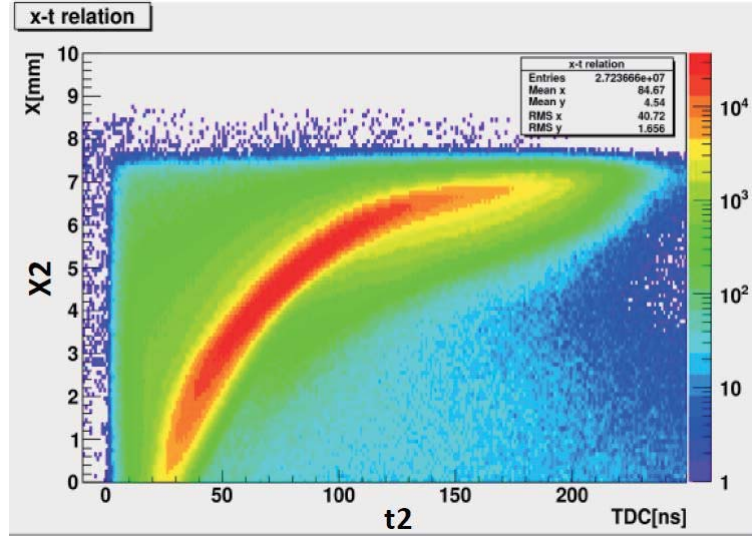


Figure B.3: 2-Dimensional plot of the X-T relation based on $50 \mu\text{m/ns}$ drift velocity. The resulting plot shows that drift velocity was not constant.

From this figure, the fact is clear that the drift velocity was not constant. This means that the drift velocity which has been assumed at first is not correct. Indeed, the actual drift velocity should have been a quadratic function,

$$X2(t_1 - t_0) = v_1(t_1 - t_0)^2 + v_2(t_1 - t_0), \quad (\text{B.2})$$

where X2 is satisfied with $X(0) = 0$. Suppose that the actual velocity has been assumed, the resulting X-T relation should be the same as the assumed one. Namely, somehow or other I have to look for the actual velocity. For the reason above, the so-called iteration method was adopted.

B.2 Iteration method

The complete method is as follows,

- **an estimate of the drift velocity**

In the beginning of the iteration, the drift velocity is assumed as an initial parameter based on the measurement such as the Fig(B.1) ($v_2 = 50 \mu\text{m/ns}$). In my case, although $v_1 = 0$ was adopted as an initial parameter, the value of χ^2 finally diverged. Thus, for avoiding this kind of situation, a non-zero value was assigned to v_1 .

- **2-Dimensional X-T relation plot**

Next, as already mentioned and shown in Fig(B.3), a 2-Dimensional X-T plot is drawn based on the trigger condition above. This 2-Dimensional plot must be consistent with the initial parameters in the case that the correct value has been assumed.

- **Projection to X axis**

The 2-Dimensional plot was projected onto the X axis by a 10 ns interval. Next, all the projected histograms are fitted by gaussian function as shown in Fig(B.4).

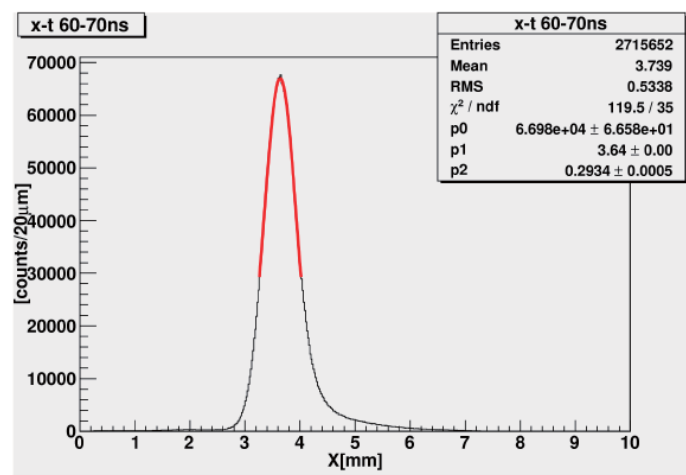


Figure B.4: Sample of projected histogram. These products were fitted by Gauss function.

Here, one of the fitting parameters, p1, which corresponds to σ , could be roughly regarded as the position resolution relying on the interval, namely the resolution corresponds to a drift velocity fluctuation. In fact, the fluctuation is including angle fluctuation. Supposing a shape of the cell structure corresponds to a circle, the shape of the equi-drift-time line also corresponds to the circle. On the other hand, since our polarimeter has the cell structure of a rectangle, the shape of the equi-drift-time line is more complicated.

- **1-Dimensional X-T relation plot and a fitting using the assumed parameters**

All the mean values of the projected products with some deviation are plotted in a 1-Dimensional graph. After all projected products are plotted as a point, the graph was fitted by a quadratic function with the assumed parameters as shown in Fig(B.5).

Although I should use an error of the mean value for the Fig(B.5), the value of sigma is actually adopted as the error because of the difficulty of the iteration method, namely the error from the mean value causes the value of χ^2 to diverge.

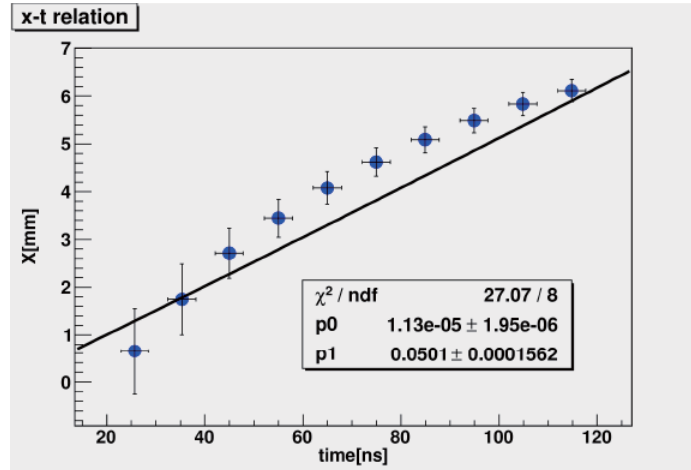


Figure B.5: Result of fitting with an assumed parameter. At the same time, the value of χ^2 was recorded every time.

- **Recording the value of χ^2**

After the fitting was performed under the initial condition, the resulting parameters, in particular χ^2 , were recorded. In case that the χ^2 diverged, the initial drift velocity was changed.

- **An estimate of the new drift velocity**

At the same time, the best fitting parameters are also extracted as the new initial parameters.

It was not until these operations were done repeatedly that the value of χ^2 finally converged. The resulting values of χ^2 are plotted every time as shown in Fig(B.6). Furthermore the results of the final parameters are also shown in Fig(B.7). These final parameters were adopted as the actual drift velocity.

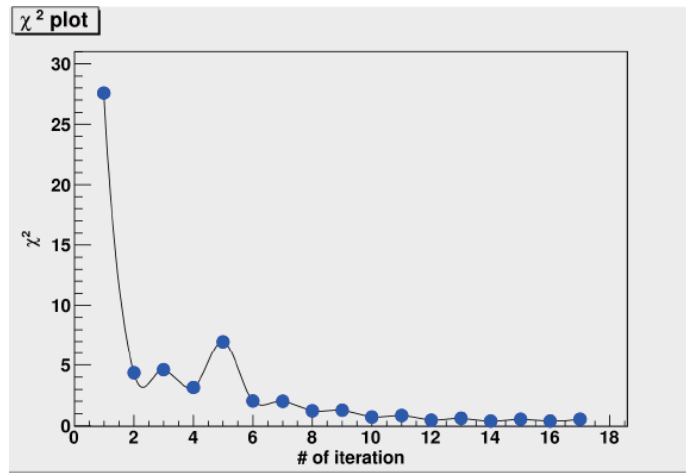


Figure B.6: The variation of χ^2 . The value of χ^2 converged after several iterations.

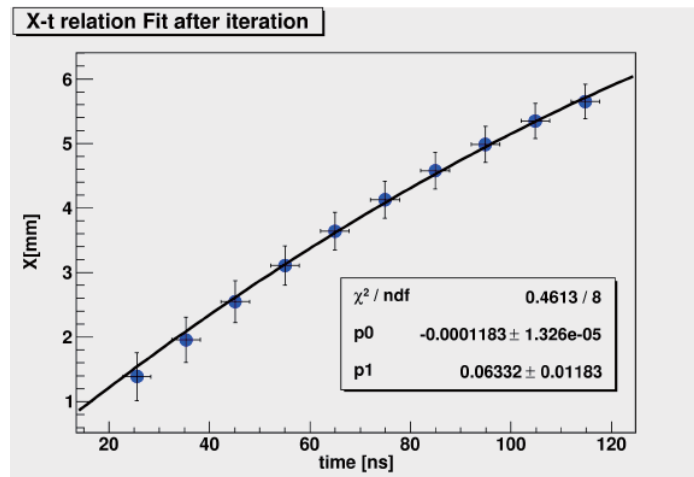


Figure B.7: Final result of parameters corresponding to actual drift velocity.

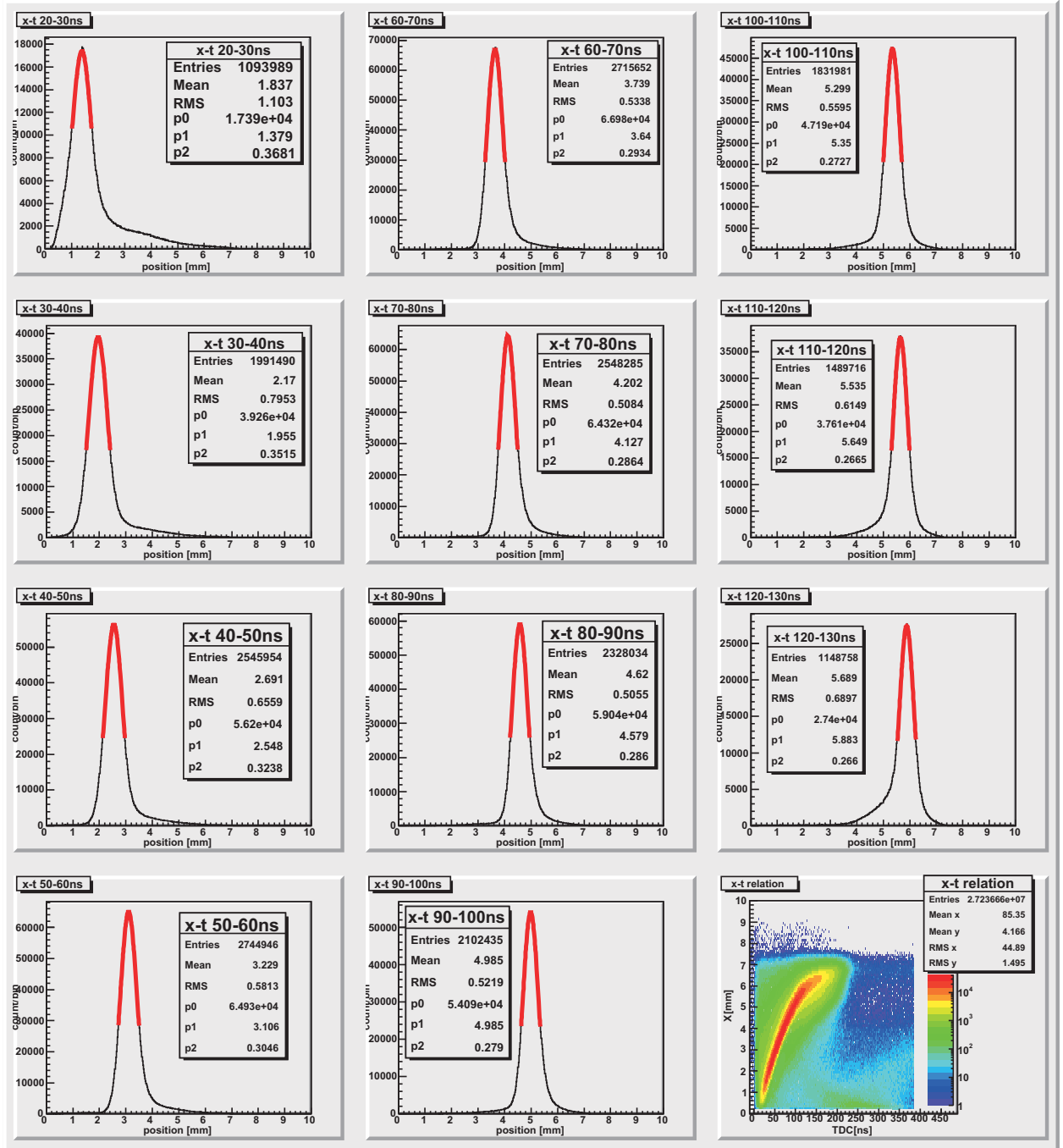


Figure B.8: A final set of the projected histograms and the 2-Dimensional X-T plot. The mean value of the histogram is shifted toward the right direction and the value of sigma is becoming smaller.

In addition, the deviations of the projected products were also plotted with respect to every time interval as shown in Fig(B.9). The graph was fitted by the function below,

$$\sigma(t) = \frac{p0}{\sqrt{t}} + p1, \quad (\text{B.3})$$

where both p_0 and p_1 are free parameters. These parameters are also essential as the tracking parameters as was explained in Chapter 4.

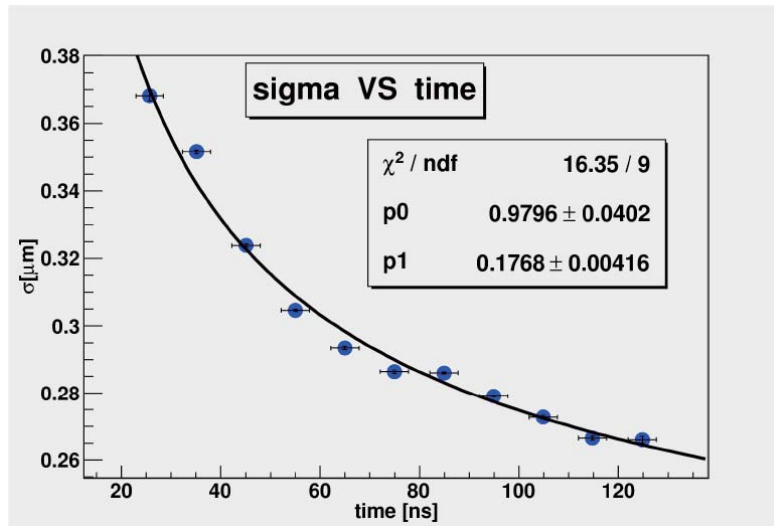


Figure B.9: The variation of σ . The resulting parameters were adopted as the fluctuation of the equi-drift-time line.

Appendix C

Beam polarization

In this section, the result of the beam polarization measurement will be described though the polarimeter has the kind of uncertainty caused by the spurious effects generated from its mechanical structure. As shown in Fig(4.26), the muon beam enters into the polarimeter perpendicular to the Al plates in this measurement.

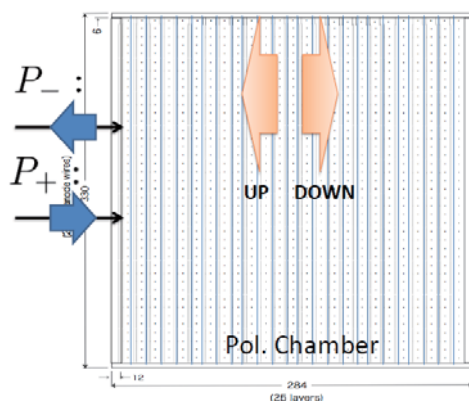


Figure C.1: Conceptual diagram of the longitudinal polarization measurement.

As already mentioned in 4.5.2, the probability p_+ (or p_-) that the decay positron is emitted in the same (or opposite) semi-sphere as the muon spin polarization is

$$\begin{aligned}
 p_+ &= \int_0^1 \frac{1 + \alpha_e x}{2} dx = \frac{7}{12}, \\
 p_- &= \int_{-1}^0 \frac{1 + \alpha_e x}{2} dx = \frac{5}{12}.
 \end{aligned}
 \tag{C.1}$$

Thus, the probability that the decay positron was emitted into the upstream (or downstream) semi-sphere is

$$\begin{aligned}
 p_{up} &= P_+ \times \frac{5}{12} + P_- \times \frac{7}{12}, \\
 p_{down} &= P_+ \times \frac{7}{12} + P_- \times \frac{5}{12},
 \end{aligned}
 \tag{C.2}$$

where P_+ and P_- are positive helicity and negative helicity, respectively. Finally, the asymmetry can be obtained as,

$$A = \frac{P_{down} - P_{up}}{P_{down} + P_{up}} = \frac{1}{6}(P_+ - P_-), \quad (C.3)$$

where A is the observable. Therefore, the beam polarization can be replaced with the *fwd/bwd* asymmetry in this way. The resulting picture is shown in Fig(4.27).

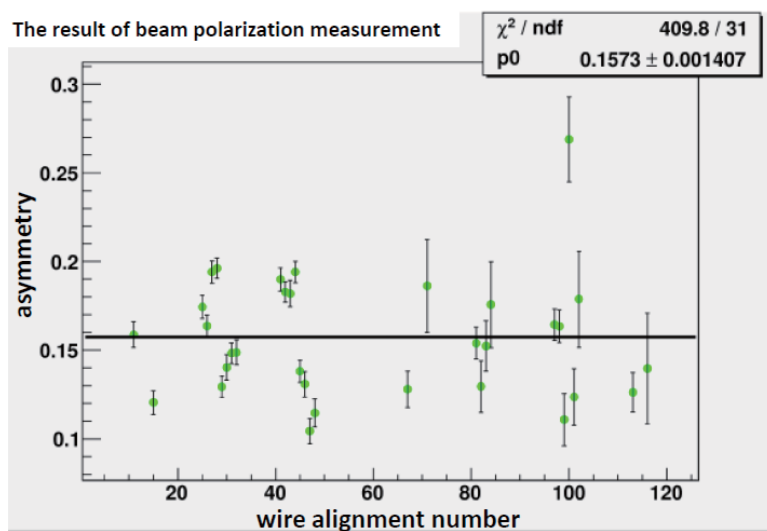


Figure C.2: Asymmetry of the longitudinal polarization measurement.

From the resulting graph, the value of $A \sim 0.16$ was observed as the beam asymmetry. This means that the muon beam has a large polarization corresponding to $\sim 95\%$ though there are some uncertainties as mentioned above.

Since the muon beam can mainly include both the cloud muon with low polarization and the decay muon, the beam polarization should be small enough. However the result is different from the assumption.

Bibliography

- [1] Particle Data Group, <http://pdg.lbl.gov/>.
- [2] Review of SM in reference[1].
- [3] Review of Neutrino mixing in reference[1]
- [4] Stephen P. Martin et al., arxiv:[hep-ph/9709356v5](2008).
- [5] A.Sakharov, in "The Early Universe" by E.W.Klb and M.S. Turner, Frontiers in Physics lecture note series, vol.69 (1989), Addison-Weilet pub.
- [6] Neven Bilic et al., Phys. Lett. B 535 17 (2002).
- [7] Review for MSSM in reference[1]
- [8] LHC homepage, <http://lhc.web.cern.ch/lhc/>.
- [9] T2K homepage, <http://www-nu.kek.jp/jhfnu/>.
- [10] Belle homepage, <http://belle.kek.jp/>.
- [11] J-PARC homepage, <http://j-parc.jp/>.
- [12] J.H. Christenson et al., Phys. Rev. Lett. 13 (1964) 138.
- [13] KOTO homepage, <http://koto.kek.jp/>.
- [14] TREK homepage, <http://trek.kek.jp/>.
- [15] G.Luders, Danske Mat. Fys. Medd. 28, 5 (1954); Annals of Physics 2, 1 (1957); W. Pauli, Nuovo Cimento 6, 204 (1957).
- [16] P.K.Kabir, Phys. Rev. D2, 540 (1970).
- [17] S.M. Barr and W.J. Marciano, "Electric Dipole Moments", p.455 in "CP violation" ed. C. Jarlskog, World Scientific.
- [18] J.J.Sakurai, Phys.Rev. 109, 980 (1957).
- [19] S.R. Blatt et al., Phys. Rev. 109, 980 (1957).
- [20] M.Abe et al.[E246 collaboration], Phys. Rev. Lett. 93, 131601 (2004).

- [21] TRIUMF homepage, <http://www.triumf.ca/>.
- [22] N. Cabibo and A. Maksymowicz, Phys. Lett. 9, 352 (1964); *ibid* 11, 360(E) (1964); *ibid* 14, 72(E) (1966).
- [23] S. Eidelman et al. [Particle Data Group], p.618 in "Review of Particle Physics", Phys. Letters B592, 1 (2004).
- [24] M.Kobayashi, T.-T. Lin, and Y. Okada, Prog. Theor. Phys. 95, 361 (1995).
- [25] G.-H. Wu, K. Kiers and J.N. Ng, Phys. Rev. D56, 5413 (1997).
- [26] M. Leurer, Phys. Rev. Lett. 62, 1967 (1989).
- [27] I.I. Bigi and A.I. Sanda, "CP Violation", Cambridge University Press (2000).
- [28] A.R. Zhitnitkii, Yad. Fiz. 31. 1014 (1980).
- [29] V.P. Efrosinin et al., Phys. Lett. B493, 293 (2000).
- [30] R. Garisto and G. Kane, Phys. Rev. D44, 2038 (1991).
- [31] G. Belanger and C.Q. Geng, Phys. Rev. D44, 2789 (1991).
- [32] A.L. Ssnada, Phys. Rev. D23, 2647 (1981).
- [33] N.G. Deshpande, Phys. Rev. D23, 2564 (1981).
- [34] H.-Y. Cheng, Phys. Rev. D26, 143 (1982).
- [35] J.-Y. Cheng, Phys. Rev. D34, 1397 (1986).
- [36] I.I. Bigi and A.I. Sanda, Phys. Rev. Lett. 58, 1604, (1987).
- [37] M. Leurer, Phys. Rev. Lett. 62, 1967 (1989).
- [38] H.-Y. Phys. Rev. D42, 2329 (1990).
- [39] S.Weinberg et al., Phy. Rev. Lett. 37, 657 (1976)
- [40] M.Abe et al., Phys. Rev. D73, 072005 (2006).
- [41] Y. Grossman, Int. J. Mod. Phys. A19, 907 (2004); T. Hurth, Rev. Mod. Phys. 75, 1159 (2003).
- [42] K. Hara et al., arxiv:[hep-ex/1006.4201v3](2010).
- [43] Y. Okada, Y.Shimizu, and M.Tanaka. arxiv:[hep-pf/9704223].
- [44] V.V. Anisimovsky[E246 collaboration] et al., Phys. Letters B562, 166 (2003).
- [45] G.-H. Wu and J.N. Ng, Phys. Lett. B392, 93 (1997).

- [46] M. Fabbrichesi and F. Vissani, Phys. Rev. D55, 5334 (1997).
- [47] TREK Technical Note No,5 Muon Spin Relaxation Study of Several Material for the Polarimeter Muon Stopper (J. Imazato 2007).
- [48] TREK Technical Note No,9 Performance of 1/5 prototype chamber studied at KEK FTBL (S. Shimizu and K. Horie 2008).
- [49] Luca STANC et al., Computer Physics Communications 57 380-384 (1984).
- [50] Introductory Muon Science (K. Nagamine).
- [51] K0.8 report to FIFC June'07 (J. Doornbos; April, 2005).
- [52] Addendum to the K0.8 report (J. Doornbos; May, 2007).
- [53] C.L.Wang et al., Phys. Rev. Lett. 25, 1068 (1970).
- [54] M.P. Grigorev et al., Instrum. Exp. Tech. 41, 803 (1998).
- [55] A. Toyoda et al., "Development of π/K Differential Fitch-type Cherenkov Counter for J-PARC K1.1BR Beamline", Proceedings of the 7 th Annual Meeting of Particle Accelerator Society of Japan, 2010, THPS078.